Optimisation of Tether Orientation in Head and Neck Restraint Systems

by
Vincent Phibbs Clarke

Thesis presented in partial fulfilment of the requirements for the degree of Master of Engineering (Mechatronic) in the Faculty of Engineering at Stellenbosch University

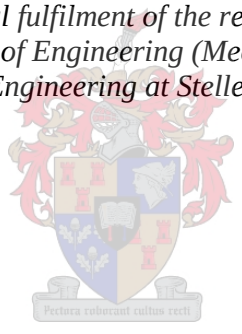

Supervisor: Mr Cornel de Jongh
Co-supervisor: Dr Johan van der Merwe

December 2021

Declaration

By submitting this thesis electronically, I declare that the entirety of the work contained therein is my own, original work, that I am the sole author thereof (save to the extent explicitly otherwise stated), that reproduction and publication thereof by Stellenbosch University will not infringe any third party rights and that I have not previously in its entirety or in part submitted it for obtaining any qualification.

Date: December 2021

Abstract

The Head and Neck Restraint (HNR) is a critical component of safety equipment for racing car drivers. In the event of a collision, this device lessens the forces acting on the driver's head and neck. The working of the HNR relies on a tether, attached between the driver's helmet and a shoulder support, which prevents excessive forward flexion during sudden deceleration. There appears to be a lack of published information describing the tether's optimal orientation for injury risk minimisation. This project aims to correct this by determining the optimal orientation of the HNR's tether. To this end, solid body models of the human and Anthropomorphic Test Device (ATD) head and neck regions were developed and the effects of various tether orientations were tested on these models.

For the ATD model, the aluminium components were represented as solid bodies, while the rubber components were modelled as non-linear springs. This model was validated against neck calibration data as specified by ATD manufacturers. In the human head and neck model, vertebrae were modelled as solid bodies, ligaments and intervertebral (IV) discs as non-linear springs and muscles as Hill-type muscle models. The human model was validated against data from a study involving human volunteers subjected to simulated frontal collisions. Both models predicted responses that were similar to the data in literature. The most significant differences were with the Occipital Condyle (OC) forces and moments where it was decided that these measurements should be closely monitored going forward.

The HNR's tethers were modelled as linear springs with certain adjustable parameters, such as the angle at which the tethers act. These parameters could then be passed to an optimisation algorithm to determine the optimal tether set-up. Three sets of objective functions were tested, where these functions computed the maxima of the N_{ij} Neck Injury Criterion (NIC), the scaled OC moment and the scaled OC axial force, respectively.

It was found that, of all the parameters included in the optimisation problem, the tether angle had the greatest impact on the effectiveness of the HNR. While the human model's optimal angle is nearly nine degrees below the horizontal, an average difference of 13 degrees is measured between the optimal angles of the two models. This could indicate that an HNR designed using a real-world ATD may yield a design that is not as effective for human users. In addition to determining the optimal angle, it was found that moving the position of the attachment point on the helmet 36 mm upwards may further reduce the risk of injury. Finally, the addition of a second tether to the HNR does not appear to improve results.

Opsomming

Die kop-en-nekvertragingstoestel is ’n sleutelkomponent van veiligheidstoerusting vir renjaers. In die geval van ’n botsing verminder hierdie toestel die uitwerking van kragte op die kop en nek van die renjaer. Die werking van die kop-en-nekvertragingstoestel maak staat op ’n weerstandband, geheg aan die valhelm en ’n skouerstut, wat oormatige vorentoe-fleksie tydens skielike vertraging verhoed. Dit blyk dat daar ’n tekort is aan gepubliseerde inligting wat die weerstandband se optimale oriëntasie vir die vermindering van beseringsrisiko beskryf. Hierdie projek beoog om dit reg te stel deur die optimale oriëntasie van die kop-en-nekvertragingstoestel se weerstandband te bepaal. Ten einde hierdie doel te bereik is soliedeliggaam modelle van die kop-en-nekareas van die mens sowel as van die antropomorfiese toetstoestel ontwikkel en is die uitwerking van verskeie weerstandband oriëntasies op beide getoets.

Vir die antropomorfiese toetstoestel se kop-en-nekmodel verteenwoordig soliede liggame die aluminium komponente en nie-lineêre vere die rubber komponente. Nek-kalibrasie data van antropomorfiese toetstoestel-vervaardigers is gebruik om die werking van hierdie model te bevestig. In die menslike kop-en-nekmodel is werwels gemodelleer as soliede liggame, ligamente en intervertebrale skywe as nie-lineêre vere en spiere as “Hill”-tipe spiermodelle. Die werking van die menslike model is bevestig deur dit te vergelyk met vrywilligers wat in ander studies onderworpe is aan gesimuleerde frontale botsings. Beide modelle het reaksies voorspel wat soortgelyk is aan data in die literatuur. Die mees noemenswaardige verskille is gevind in die oksipitale kondiel se kragte en buigmomente—hier is besluit dat die opnames daarvan voortaan noukerig gemonitor moet word.

Die kop-en-nekvertragingstoestel se weerstandbande is gemodelleer as lineêre vere met sekere verstelbare veranderlikes, o.a. die hoek waarteen die weerstandbande inwerk. Hierdie veranderlikes kan vir ’n oprimeringsalgoritme gevoer word om die optimale opset van die weerstandband te bepaal. Drie stelle doelwit funksies is getoets en deur díe te bereken het elk een van die volgende opgelewer: die maksimum N_{ij} nekbeserings-kriterium, die maksimum geskaalde oksipitale kondiel se buigmoment en die maksimum geskaalde oksipitale kondiel se aksiale krag.

Daar is bevind dat, uit al die veranderlikes betrokke in die optimasie probleem, die weerstandbandhoek die grootste impak gehad het op die doeltreffendheid van die kop-en-nekvertragingstoestel. Die menslike model se optimale hoek is byna nege grade onder die horisontaal. ’n Gemiddelde verskil van 13 grade is gemeet tussen die twee modelle se optimale hoeke. Dít kan aandui dat ’n kop-en-nekvertragingstoestel wat ontwerp is met die gebruik van ’n werk-

like antropomorfiese toetstoestel 'n ontwerp kan oplewer wat nie ewe doeltreffend is vir menslike gebruik nie. Buiten die vasstelling van die optimale hoek, is ook gevind dat indien die aanhegtingspunt van die weerstandband 36×10^{-3} m opwaarts geskuif word, die beseringsrisiko verder verminder kan word. Laastens is gevind dat die byvoeging van 'n tweede weerstandband tot die kop-en-nekvertragingstoestel klaarblyklik nie beter resultate oplewer nie.

Acknowledgements

I need to convey my appreciation towards my supervisors for their support during this project. Without their guidance, with respect to the project's content and the writing of the thesis, I would not have been able to complete it.

I would like to thank the Skye Foundation for their financial contribution towards my studies. This assisted in providing me the opportunity to pursue my goal of postgraduate studies.

Words cannot express the gratitude that I have for my parents. Not only have they always been there to encourage me, but they lay the foundations that allowed me to come this far. Thank you for teaching me the value of education and always reminding me that we never stop learning.

To my dear Anita, a list of reasons can be made to thank you. Highlights of this list include your words of encouragement when my own motivation ran low, planning fun distractions when I needed a break and help with the grammatical editing of the thesis.

Finally, none of this would have been possible without the blessings of God. He has provided me with endless opportunities and I know that I am always protected by His hands.

Contents

List of Figures

List of Tables

List of Abbreviations

ALL	Anterior Longitudinal Ligament
ARD	Automatic Relevence Determination
ATD	Anthropomorphic Test Device
CAD	Computer Aided Drawing
CE	Contractile Element
CG	Centre of Gravity
CL	Capsular Ligament
EI	Expected Improvement
FEM	Finite Element Method
FIA	Fédération Internationale de l'Automobile
GP	Gaussian Process
HANS	Head and Neck Support
HNR	Head and Neck Restraint
ISL	Interspinous Ligament
IV	Intervertebral
LF	Ligamentum Flavum
LNL	Lower-Neck Load Index
MRI	Magnetic Resonance Imaging
NDC	Neck Displacement Criterion
NIC	Neck Injury Criterion
NMT	Neuromuscular Transmission
OC	Occipital Condyle
pCSA	Physiological Cross-Sectional Area
PEE	Parallel Elastic Element
PI	Probability of Improvement
PLL	Posterior Longitudinal Ligament
RMS	Root Mean Square
SDE	Serial Damping Element
SEE	Serial Elastic Element
SHAP	SHapley Additive exPlanations
SSL	Supraspinous Ligament
THOR	Test device for Human Occupant Restraint

Chapter 1

Introduction

1.1 Background

The fastest legal racing cars travel at speeds in excess of 350 km/h. Coming to a stop in a collision forces such a car to rapidly decelerate, while Newton dictates that the driver's body wants to continue moving forward. The only factors reducing the risk of injury are safety equipment including seat belts, helmets and Head and Neck Restraint (HNR) systems, as prescribed by the Fédération Internationale de l'Automobile (FIA) [1; 2; 3; 4]. The FIA acts as the most senior governing body with respect to racing of any motorised vehicles with four or more wheels.

Multiple studies concerning accidents at racing events note the relative prevalence of accidents, as well as the nature and severity of the resulting injuries. Chapman and Oni [5] describes the likelihood of experiencing an accident during a race at Brands Hatch in the United Kingdom as greater than experiencing an accident on a public road. The resulting injuries are often attributed to the head and neck. At a similar point in time, Steele [6] recorded that the number of accidents at Indianapolis Raceway Park is near equal to the number of races. Of these accidents, only 3.5 % were head and neck injuries, but they were all serious enough to require intensive care hospitalisation. Chesser *et al.* [7] conducted a similar study to determine the medical requirements needed at a race track and found in their research that 31 % of serious car accidents result in head and neck injuries. Similarly, the study by Minoyama and Tsuchida [8] at Fuji Speedway showed that 34 % of injuries were related to the neck. This shows that head and neck injuries among racing car drivers are a significant risk regardless of where the race is held.

The aforementioned HNR works with the helmet to protect the driver's head and neck during impact. The HNR system involves a tether which is connected to the helmet at one end and to the shoulder support at the other end. During extreme deceleration its purpose is to prevent hyperflexion and excessive tension of the neck. The requirements of this tether system are outlined in Standard FIA 8858-2010 [2] and tested according to SFI Specification 38.1 [9]. The FIA approved HNR systems are listed in Technical List N29 [10] and these can be paired with any helmet from the FIA approved Technical List N69 [11]. However, none of these standards specify the optimal angle at which the tether should ideally act.

1.2 Aims and Objectives

The primary aim of this project is to determine the optimal angle at which the tethers in an HNR system must attach to the helmet. The secondary aim is to investigate the difference in response between a model of the human neck and a model of the Anthropomorphic Test Device (ATD) neck. In order to accomplish this, the following objectives have been identified.

- Build and validate a human head and neck model.
- Build and validate an ATD head and neck model.
- Execute optimisation processes to find the optimal tether angle for both models.

1.3 Motivation

The HNR system is critical in protecting drivers from base of skull fractures and cervical fractures by limiting violent forward movement of the head during a collision [12]. While the tethers effectively prevent such movement, a tether pulling at the wrong angle may result in residual stresses building in the neck. There appears to be no published research into the optimal angle at which a tether needs to act on the head. The aim of this project is to fill this void by finding the optimal angle at which a tether needs to act to minimise all forces acting on the head and neck during a high speed collision.

Due to the severe risk of injury to humans under conditions specified in the HNR's certification testing, Hybrid III ATDs are used as surrogates [9]. The accuracy with which the Hybrid III's head and neck can predict injury is limited due to the manner in which it is constructed. This project intends to compare the responses of ATD and human necks to determine whether a tether angle obtained from testing on an ATD will yield the optimal angle for a human user.

Chapter 2

Literature Review

The literature review intends to provide the reader with the concepts necessary for understanding the background information. This chapter is divided into sections that consider the anatomy of the head and neck, the models developed based on the actual head and neck, the information pertaining to ATDs, data related to the HNR system and a discussion on optimisation algorithms.

2.1 Head and Neck Anatomy

The neck acts as the connection between the head and the torso. Therefore, there are a variety of structures that need to pass through this narrow part of the body to allow for normal function. Kohan and Wirth [13] summarised that the neck consists of the cervical spine, muscles, nerves, blood vessels, lymph nodes and submandibular glands. This project will only focus on the muscles and the cervical spine, which consists of vertebral bones, intervertebral (IV) discs and ligaments, since these would be related to the dynamic forces and moments that are experienced by the head and neck during a collision.

2.1.1 Anatomical Planes and Terminology

Describing the anatomy requires an unambiguous set of terminology. Figure 2.1 shows four directions relative to the human body. Anterior is always towards the forward direction of the body, while posterior is in the opposite direction. Superior is towards the top of the head and inferior is towards the feet. The two remaining directions (left and right of the body) are both referred to as lateral. The mid-sagittal plane divides the left and right sides of the body symmetrically.

The curvature of the spine is split into four regions. The cervical and lumbar spine both curve backward as shown in Figure 2.1 and this is defined as a lordotic curvature. Kyphotic curvature is the opposite to lordotic curvature and is exhibited by the thoracic and sacral spine.

The final two terms that need to be defined are actions that relate to the tilting of the head. Tilting the head and neck in the anterior direction is known is flexion. The opposite to flexion is the bending of the head in the posterior direction and this is known as extension.

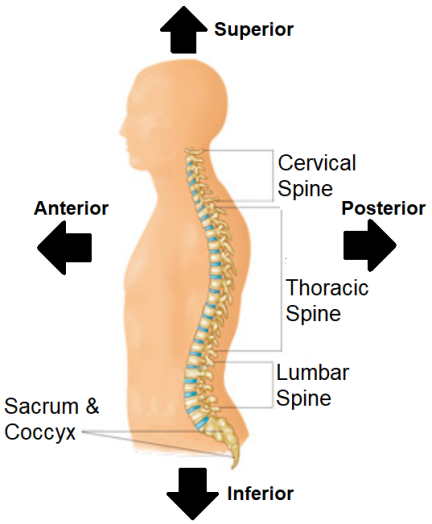

Figure 2.1: Diagram showing the curves of the spine, as well as the anatomical directions (Image from: Li [14])

2.1.2 Bony Anatomy of Cervical Vertebrae

The cervical spine consists of seven vertebrae that attach between the thoracic spine and the head such that the cervical spine forms a lordotic curve. Structurally each vertebra is made of a vertebral body, facet joints, transverse processes and a spinous process. Figure 2.2 shows the general shape of a vertebra with C3 being the bottom view and C4 the top view. The top of the vertebral body is concave and the bottom is convex to prevent excessive relative translation of the bodies in the horizontal plane [15]. Lateral to each side of the body, both superiorly and inferiorly, are facet joints that act between two successive vertebrae. These joints are at an approximate angle of 45 degrees and allow for flexion and extension of the neck up to 35 and 70 degrees respectively [16]. Finally, the spinous and transverse processes act as attachment points for muscles and ligaments.

Dodwad *et al.* [15] provided general dimensions for these cervical vertebra. The bones have an average width of 17×10^{-3} m and average depth of 15×10^{-3} m. The seventh vertebra is slightly larger to link with the even larger thoracic vertebrae and has an average width of 20×10^{-3} m with an average depth of 17×10^{-3} m. All these vertebrae are between 11×10^{-3} m and 13×10^{-3} m in thickness [15].

There are two major exceptions to the structure described previously and these are the first and second cervical vertebrae also known as the atlas and the axis or C1 and C2, respectively. The diagrams of each are in Figure 2.3. The atlas connects to the occiput at the base of the skull via the concave facets on its top side to form the atlanto-occipital joint.

The atlantoaxial joint is formed between the atlas and the axis and is responsible for 50 % of the total 90 degrees of head rotation [16]. To facilitate this motion, the atlas does not have a vertebral body and the axis has a vertical spike, known as the odontoid process. The odontoid process extends into the circular

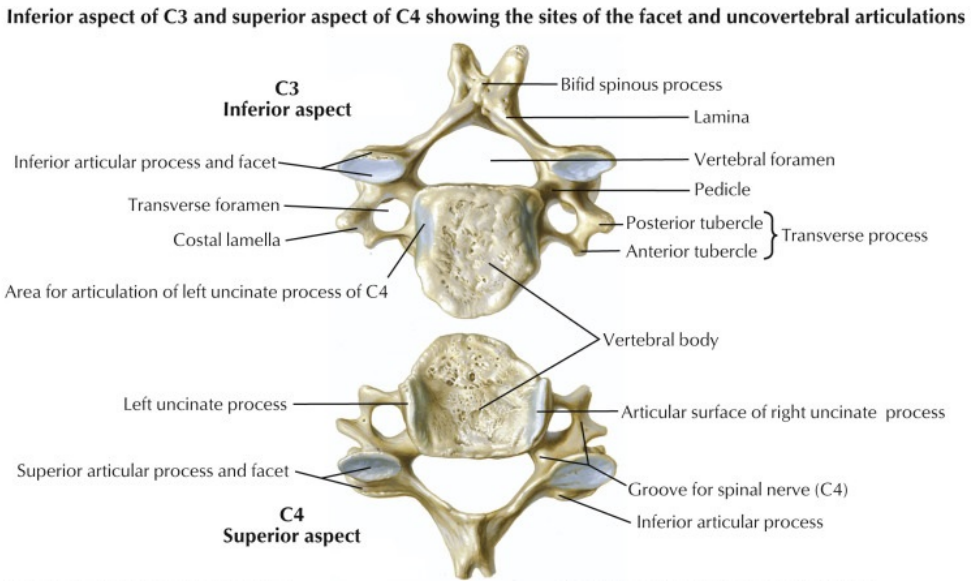

Figure 2.2: Diagram of cervical vertebra C3 and C4 (Image from: Netter [17])

hole (foramen) in the atlas and makes contact at a facet. The atlas can then rotate about the odontoid process on large flat facets on the topside of the axis [15]. The constructed view of how these two vertebra connect is shown in Figure 2.3. The inferior surface of the axis is the same as that of the other cervical vertebrae in order to attach to the rest of the spine.

2.1.3 Intervertebral Discs

Between any two successive vertebral bodies is an IV disc. Since the atlas does not have a vertebral body, there is no IV disc between the atlas and axis, nor is there one between the atlas and skull. Each IV disc is sandwiched between two cartilaginous layers and the centre of the discs act as shock absorbers within the spine [15].

The curvature of the neck is a result of the IV discs and not the vertebral bodies. The thickness of the discs is greater towards the front of the body as compared to the back and the discs make up a quarter of the total height of the cervical spine [16]. The discs also allow for a degree of anterior and posterior translation to occur between vertebrae.

2.1.4 Ligaments

Ligaments are made of fibrous connective tissue and are attached between two bodies. The ligaments are responsible for providing stability between bodies during rest and in motion.

Dodwad *et al.* [15] described the cervical spine as supported by five sets of ligaments. The first of these two are the anterior longitudinal ligament (ALL) and posterior longitudinal ligament (PLL) which run the full length of the spine on

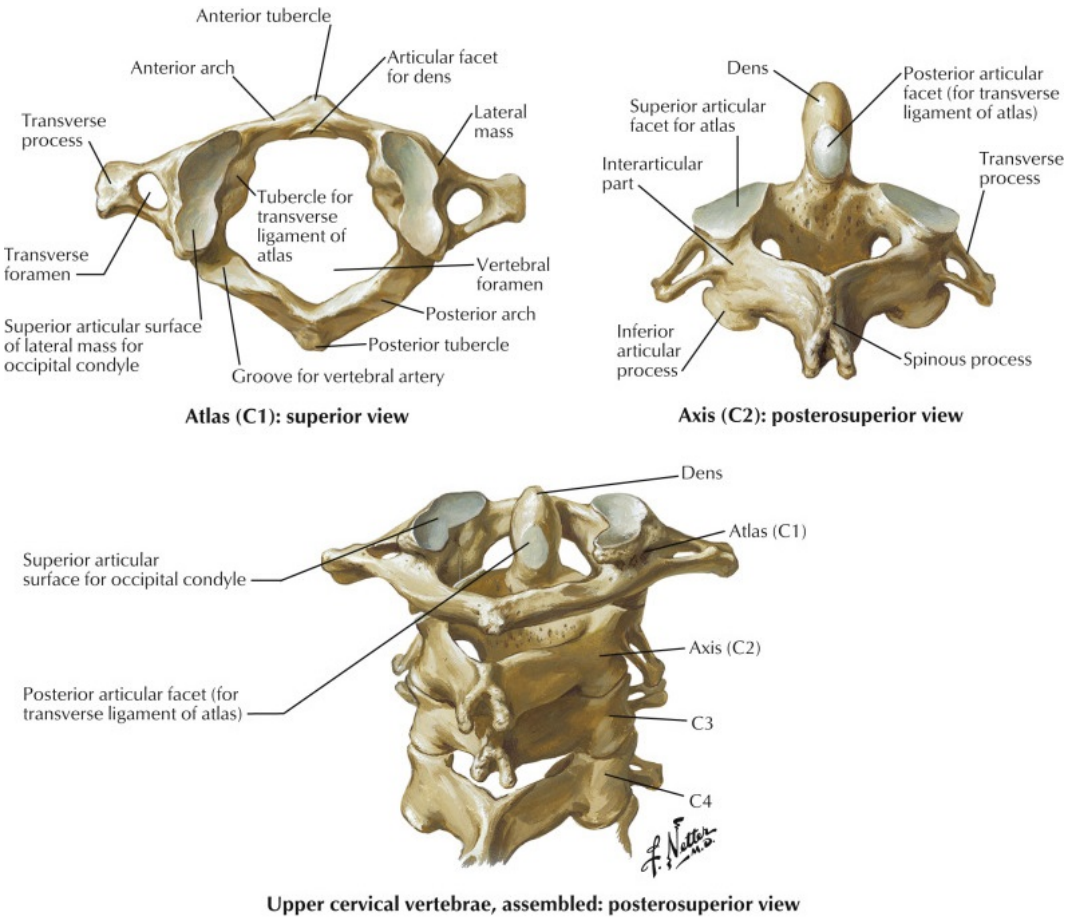

Figure 2.3: Diagram of the top view of the atlas, the posterior view of the axis and an assembled view of both (Image from: Netter [17])

the front and back of the vertebral bodies respectively. Dodwad *et al.* explained that the ligaments become broader and thinner as they pass over the IV discs as compared to the vertebral bodies. The ALL resists extension with the PLL resisting flexion.

The remaining three sets of ligaments described by Dodwad *et al.* [15] are the ligamentum flavum (LF), interspinous ligament (ISL) and supraspinous ligament (SSL). Figure 2.4 shows where these three ligaments are located on a typical cervical vertebra. All three these ligaments are resistant towards flexion of the neck.

The unique shape and function of the atlas and axis result in different ligaments being necessary to support these and their respective joints. The ALL extends to the occipital and the PLL becomes the tectorial membrane. Beneath the tectorial membrane is the cruciate ligament that pulls the odontoid process against the atlas. This ligament attaches to the atlas on either side of the odontoid process and wraps around it. The cruciate ligament then has two shoots (which are perpendicular to the rest of it) that attach to the occiput and the axis to give it its characteristic cross shape, as seen in Figure 2.5. From the sides of the odontoid process extend the alar ligaments that attach to the occipital condyle

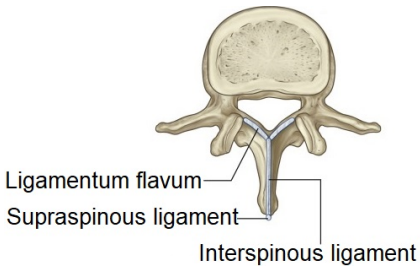

Figure 2.4: Diagram locating the LF, ISL and the SSL (Image from: Dodwad *et al.* [15])

(OC), while the apical ligament extends from the top of the odontoid process to the foramen magnum [15]. Finally, the anterior and posterior atlanto-occipital membranes attach between the atlas and the OC with the posterior membrane actually replacing the LF at this position [16].

2.1.5 Muscles

The skeletal system of the human body relies on muscles to produce movement and to maintain static position and posture. Muscles shorten and exert a force between two points on the skeleton to facilitate such movement. To allow for all possible movements, many muscles are needed and therefore contribute to approximately 40 % of the total human mass [18].

Muscles are comprised of myocytes (muscle cells) that are elongated in appearance. Between 10 and 100 myocytes are grouped into fascicles that are contained by the perimysium and 10000 to 100000 fascicles make up a muscle as shown in Figure 2.6 [18]. Each myocyte is comprised of myofibrils that are collections of sarcomeres placed in succession which is also shown in Figure 2.6. A motor unit is described as the combination of both the neurons that supply signals to the myocytes as well as a large number of these myocytes [19]. Contraction of myocytes upon receiving a neural impulse reduces the total length of the muscle by a maximum of a half [19]. This is made possible by each of the sarcomere structures reducing their length through the building blocks of a sarcomere sliding over each other [18].

It has previously been mentioned that muscles require attachment points on two separate bones to generate movement. These attachments may come in the form of tendons which are made of tough, fibrous tissue that extend from the muscle fibres and attach to the bone [19]. The connection referred to as the origin is on the bone that is not intended to move while the insertion connection is on the bone that should move. An example of this is the bicep in the upper arm that has its origin near the shoulder and its insertion on the lower arm in order to move the lower arm.

Muscles form lever systems where the muscle acts as the applied force at the insertion point, the joint between bones is the fulcrum and the far or distal end of the moving bone is the load. Basmajian [19] describes that as the insertion point

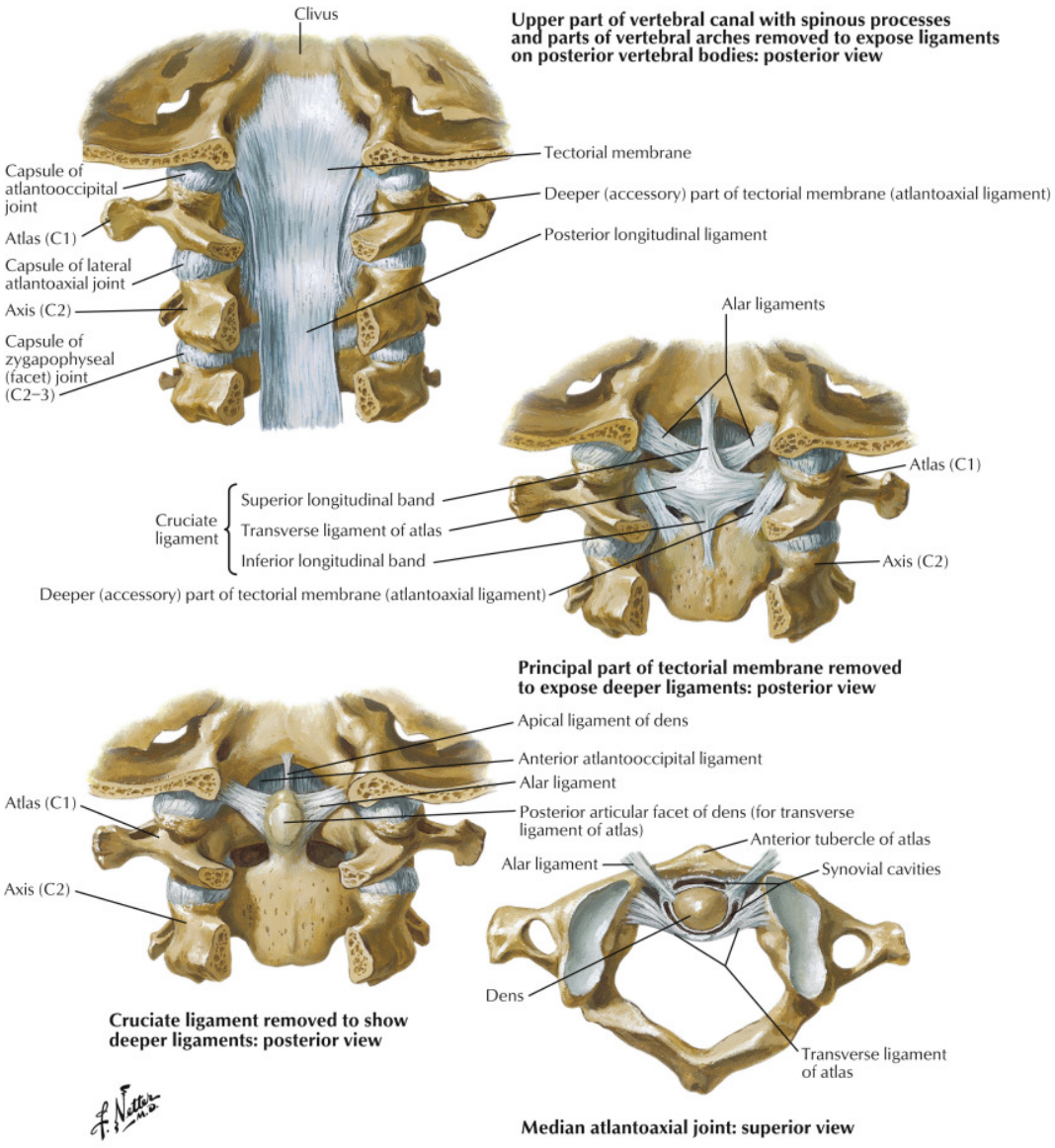

Figure 2.5: Diagram showing the ligaments for the atlas and axis (Image from: Netter [17])

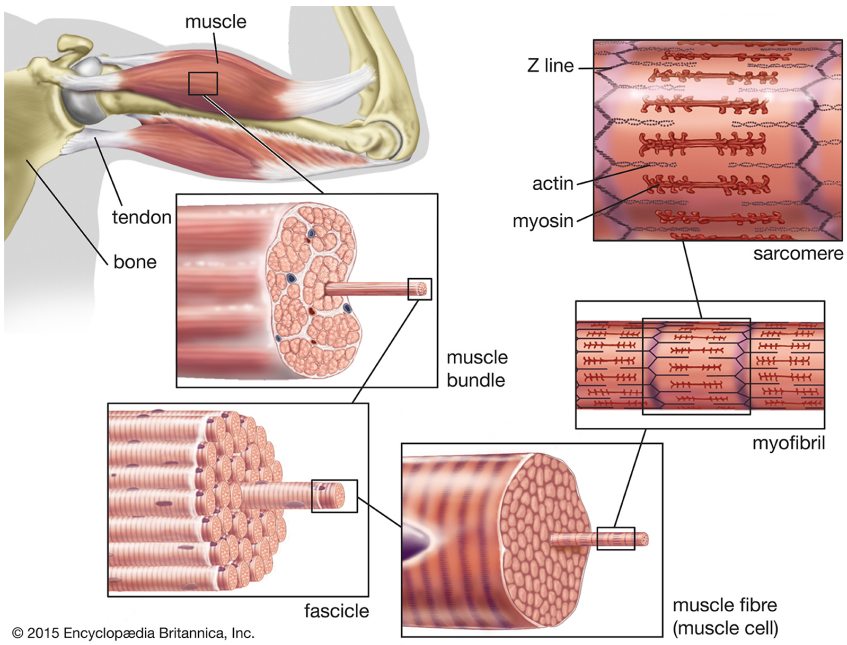

Figure 2.6: Structure of skeletal muscles (Image from: Encyclopædia Britannica [20])

nears (moves proximally to) the joint, the speed that the load travels at increases and the amount of force required to move the load also increases. Increasing the force produced by a muscle is as simple as placing more muscle fibres in parallel. Therefore, a greater cross-sectional area, also referred to as physiological Cross-Sectional Area (pCSA), is proportional to the strength of the muscle [18].

There are approximately 30 muscles that have either an origin or insertion point within the neck region. Many of these named muscles have multiple origin or insertion points that make understanding the direction of force more difficult. The muscles are divided into three regions, namely the anterior neck muscles, the lateral neck muscles and the posterior neck muscles.

The anterior neck muscles consist of the sternocleidomastoid, infrahyoid, suprahyoid and scalene muscles [21], while the lateral neck muscles are the longus capitis and the longus colli [22]. The remaining muscles are all found in the posterior region. These are the multifidus, the levator scapulae, the trapezius, the suboccipital muscles, the splenius capitis and cervicis, the longissimus capitis and cervicis, the spinalis capitis and cervicis, the semispinalis capitis and cervicis and the iliocostalis cervicis [15; 22; 23; 24]. These muscles are all listed in Table A.1 in Appendix A with their origin and insertion points and the resulting actions that each produces when contracting. Backman *et al.* [25] shows that the neck muscles in open-wheel car racing drivers is approximately 18 % stronger than those of other people of the same age.

2.1.6 Injuries

Injuries related to the neck can be described as either soft tissue injuries or bone injuries. Soft tissue injuries, also known as whiplash injuries, are as a result of high-impact hyperextension and hyperflexion. These injuries affect the ligaments, IV discs and muscles in the neck as well as other structures that pass through the neck region.

Soft Tissue Injuries

Ligamentous injuries usually manifest as sprains, but more severe cases may include complete ligament rupture when stretched beyond their physical limits. During hyperextension the anterior longitudinal ligament is most at risk, while hyperflexion places strain on the interspinous ligament and ligamentum flavum. Both hyperextension and hyperflexion occur during vehicle accidents and therefore the neck ligaments are at high risk. Furthermore, Li *et al.* [26] claims that an increase of more than 7×10^{-3} m in the length of the longitudinal band of the cruciate ligament during frontal impacts is indicative of failure. Also, a distance greater than 3×10^{-3} m between the odontoid process and its joint onto the atlas indicates failure of either the transverse ligament or the alar ligament. Other injury limits include a strain experienced by the ALL in excess of 0.222 and forces experienced by the alar and cruciate ligaments in excess of 200 N and 350 N respectively [26, p.93].

The IV disc injuries associated with whiplash motion are as a result of a complex combination of compression, distraction and shear forces. These forces result in cracking of the outer layer of the disc, disc herniation and disc separation. The major issue with these injuries is that they may place pressure on the spinal cord and create other complications. During a frontal impact, the IV disc between C2 and C3 are at greatest risk of injury [26]. The IV discs experience failure at approximately 850 N in tension, 3100 N in compression and 20 N m in flexion and extension [26, p.94].

The final soft tissue injury to consider is that of muscle injuries. Due to the ethical issues with testing the limits of muscles, it is difficult to provide accurate information [26]. However, one indicator of injury is elongation of the contractile element while the muscle should be contracting.

Bone Injuries

Dislocation, especially between the atlas and the OC, is a risk while axial forces are applied to the neck. These axial forces are most often seen during a frontal collision where the body is restrained and the head is free to fly forward [26]. During these same collisions, dislocation could be an issue at any of the facets between the cervical vertebrae. This will result in spinal instability which increases the risk of damaging the spinal cord since the cervical vertebrae involved cannot maintain their locations relative to each other [27].

Under compressive loading conditions, like those of a head making contact with a steering wheel during an accident, fractures may occur. Straight axial compression risks fracturing the atlas, while neck extension with compressive forces may fracture the axis [26].

Neck Injury Criteria

The injury mechanisms that have been discussed are difficult to measure during testing since this may be highly invasive or inaccurate due to the location of the required measurements. Criteria have therefore been developed that predict injury based on measurable velocities, accelerations and forces. The article by Li *et al.* [26] names five injury criteria.

The first of these is the Neck Injury Criterion (NIC) proposed by Boström *et al.* [28]. This formula makes use of the relative velocity (v_{rel}) and acceleration (a_{rel}) of the head to T1 with the formula

$$\text{NIC}(t) = 0.2a_{rel}(t) + v_{rel}(t)^2 \tag{2.1}$$

Injury is predicted to occur at a value greater that 15 m^2/s^2, but pain may be suffered beneath this critical point. This criterion is most often used to predict whiplash injury sustained during low-speed, rear-impact collisions [26].

The N_{ij} NIC was proposed to consider more serious cases, particularly for frontal impact. This formula is given by

$$N_{ij} = \frac{F_Z}{F_{Int}} + \frac{M_Y}{M_{Int}} \tag{2.2}$$

where F_Z is the axial force and M_Y is the bending moment for a frontal collision. F_{Int} and M_{Int} are known as the intercept values and are respectively 6160 N for compression, 6806 N for tension, 310 N m for flexion and 135 N m for extension. These values correlate to injury thresholds or tolerance levels for severe injuries [29]. The limit before injury is then equal to one.

Schmitt *et al.* [30] determined that the N_{ij} criteria was sufficient for frontal impacts, but resulted in problems with rear impacts due to different injury mechanisms. Schmitt *et al.* developed the N_{km} formula given by

$$N_{km}(t) = \frac{F_x(t)}{F_{Int}} + \frac{M_Y(t)}{M_{Int}} \tag{2.3}$$

where $F_x(t)$ is the shear force and $M_Y(t)$ is the bending moment in flexion or extension for measurements taken at the top of the neck. Minor injuries are predicted when the value of N_{km} exceeds 1 while F_{Int} is 845 N and M_{Int} is 47.5 N m in extension and 88.1 N m in flexion.

Another injury criteria is the Lower-Neck Load Index (LNL) that uses bending moments, axial and shear forces to determine the risk of injury. The formula takes the shape of

$$\text{LNL} = \frac{|M_y|}{M_l} + \frac{|F_x|}{F_{xl}} + \frac{|F_z|}{F_{zl}} \tag{2.4}$$

where M_y, F_x and F_z are the bending moment, shear stress and axial stress respectively, measured on the first thoracic vertebra. Injury is predicted when LNL exceeds one for intercept values M_l equal to 15 N m, F_{xl} equal to 250 N and F_{xl} equal to 900 N.

Finally, Schmitt *et al.* [30] proposed the Neck Displacement Criterion (NDC) to relate the physical position of the head relative to the position of T1. Schmitt *et al.* plotted the angle of the head and the vertical displacement of the head relative to T1 against the horizontal displacement of the head relative to T1 and indicated four regions based on how acceptable the motion is. The criteria then classifies these regions as excellent, good, acceptable and poor.

2.2 Head and Neck Models

Computer simulation models are designed to mimic real world structures and situations to allow for cost effective solution finding and testing. The challenge with developing these models is balancing the accuracy of the model with the complexity of the model. More complex models should provide more accurate results with respect to the real-world situation, but this is at the expense of greater computational requirements. Therefore, when repeatedly running the model, it may be necessary to simplify the real situation so that all the iterations may be completed within a reasonable amount of time.

Building models of biological systems suffers from the accuracy versus complexity trade-off since each component in the system may require a complex model of its own. A model of the human head and neck would require a minimum of bones, ligaments, IV discs and muscles. These components in the human head and neck are all composites of multiple materials that have their own unique mechanical properties and each could therefore be seen as its own model. This increases the computational time requirements since every step of the greater model will require each of the smaller models to be computed. As such, it is necessary to simplify some components into known forms such as springs and dampers. But in order to achieve this, the components may need to be in the form of a first order problem and this could result in the model only being valid for a limited range of input variables.

2.2.1 Modelling of Vertebrae

The two most prominent methods of modelling the head and neck are solid body modelling and the Finite Element Method (FEM). The solid body model assumes that the skull and vertebrae do not experience internal stresses and therefore do not deform due to force. This has the added implication that these bodies are assumed to be rigid and thus unbreakable. Solid body models rely on measuring the velocities and accelerations of the bodies as well as the forces from components acting on the bodies. These components may be the ligaments between

the vertebrae which could be modelled as springs with variable stiffness. Therefore, knowing the force exerted by the spring—which is the simulated force exerted by the ligament—may indicate whether the ligament is likely to be injured.

The FEM model attempts to correct the issue that solid body modelling does not simulate internal stresses by dividing each body into thousands of smaller bodies that act on each other. In this manner each body has internal stresses, even though they are only measurable at the boundaries of the subdivisions, and the body may undergo deformation. The advantage of using a FEM model is most often seen as an increase in accuracy of the results. This does however come at the expense of being more computationally intensive since each body has thousands of calculations that need to be computed at every time step.

Van Lopik and Acar [31] compared a FEM head and neck model to the solid body model of De Jager [32] and commented that De Jager's model was able to produce results nearly as accurate as a FEM model while being a thousand times faster. As such, in developing a model for iterative testing to minimise neck injuries, the solid body approximation may be more useful than the FEM model since it allows for many more iterations in the same timespan and injury to the muscles or ligaments will occur before injury to the bones. However, if the intention is to determine if a fracture will occur, then it would require knowledge of the internal stresses and a FEM model will need to be constructed.

The doctorate theses by De Jager [32], Van der Horst [33] and Van Lopik [34] investigated the process of generating a head and neck model. All three defined nine solid bodies with the first thoracic vertebra being the origin of the system. Development of the lower cervical spine (C3-T1) was separated from building the upper cervical spine (C0-C2) due to the changes in the general shape of the vertebrae.

Both De Jager and Van Lopik based their initial vertebral dimensions and positions for the vertebrae of the lower cervical spine on Nissan and Gilad [35]. Nissan and Gilad examined the X-rays of 157 individuals to determine the average geometric dimensions of cervical vertebrae and their position relative to each other. De Jager [32] built on this work by calculating the inertial properties of each vertebra with its surrounding tissue. Van Lopik [34] made similar assumptions as De Jager as to the relative positions of each vertebra as well as their centres of gravity, but then continued to improve the transverse process and articular facet dimensions.

The model by De Jager [32] provided mass and moments of inertia as well as locations of the atlas, axis and occiput, but neglected to mention the dimensions required for constructing the actual bones. Van Lopik [34] referenced the same mass properties from De Jager and then continued to reference various sources of physical dimensions for the upper cervical spine. The upper and lower cervical spine models were finally compiled into a single model.

2.2.2 Modelling of Intervertebral Discs

The IV discs provide connections between all vertebrae except the occiput and atlas and the atlas and axis. As such, the discs ensure that there are six degrees of freedom between successive vertebrae. The three forces (F_i) and three moments (M_i) exerted by these discs on adjacent vertebrae are given by

$$F_i = k_{ti} \cdot t_i + b_{ti} \cdot v_i \tag{2.5}$$

$$M_i = k_{\phi i} \cdot \phi_i + b_{\phi i} \cdot \omega_i \ \left(i = x, y, z\right) \tag{2.6}$$

where t_i and ϕ_i are the translational and rotational displacements, v_i and ω_i are the translational and rotational velocities and k and b are the stiffness and damping coefficients for each of the specified motions [32; 33; 34].

Moroney *et al.* [36] determined the average stiffness coefficients of cervical vertebrae through load displacement experiments for all directions of motion except tension. Moroney *et al.* assumed that the lateral shear, lateral bending and neck rotation stiffness coefficients are independent of direction. As such, Table 2.1 shows the values for the respective force directions. The tension values are available in the report by Yoganandan *et al.* [37] that specifically tested the biomechanics when experiencing tensile forces. The combination of the values by Moroney *et al.* and Yoganandan *et al.* are used in De Jager [32]'s model to simulate the responses of the IV discs. Due to a lack of information, De Jager [32] approximated the damping coefficients to be 1000 N s/m for the translational damping and 1.5 N m s/rad for the rotational damping. These assumptions were confirmed through parametric testing by De Jager [32] and Van Lopik [34] points out that these damping coefficients' purpose is for attenuation of vibration and therefore the assumptions should be acceptable.

The model by Van Lopik [34] used many of the same references as De Jager [32] and therefore has the same tension, shear, lateral bending and torsion coefficients. The compression, flexion and extension stiffness coefficients were taken from newer sources that showed them to be non-linear. The complete list of stiffness coefficients used by Van Lopik is in Table 2.1. With respect to the damping coefficients, Van Lopik used the same approximations made by De Jager. Furthermore, Van Lopik claimed that the dynamic stiffness of the IV discs is double that of the static stiffness. Implementation in the software of the model by Van Lopik used bushing constraints to represent the IV discs since these already limit all six possible motions and can easily incorporate spring constants and damping coefficients.

Although the model by Van der Horst [33] is largely based on De Jager [32], Van der Horst also determined that compression, flexion and extension should be non-linear. The values of these non-linear components were different from those of Van Lopik [34] since different sources were consulted. Van der Horst still used the same damping coefficients as De Jager, but also adapted the disc models such that the dynamic stiffness was twice that of the static stiffness.

Table 2.1: IV disc stiffness coefficients of various sources

	Force/Moment direction	Moroney *et al.* [36]	Yoganandan *et al.* [37]	Van Lopik [34]	Van der Horst [33]
N/m	Tension	-	63.5×10^3 – 82.2×10^3	63.5×10^3 – 82.2×10^3	53×10^3
	Compression	492×10^3	-	637.5×10^3 – 973.6×10^3	822×10^3 – 2931×10^3
	Anterior shear	62×10^3	-	62×10^3	62×10^3
	Posterior shear	50×10^3	-	50×10^3	50×10^3
	Lateral shear	73×10^3	-	73×10^3	73×10^3
Nm/degree	Flexion	0.21	-	Camacho *et al.* [38] load curve/2	0.022 – 5.4
	Extension	0.32	-	Camacho *et al.* [38] load curve/2	0.022 – 8.2
	Lateral bending	0.33	-	0.33	0.33
	Torsion	0.42	-	0.42	0.42

2.2.3 Modelling of Ligaments

Various ligaments are attached at multiple points on each of the cervical vertebrae to stabilise the head and neck. Between each of the lower cervical vertebrae acts six ligaments that were modelled as non-linear springs by De Jager [32]. These are the anterior longitudinal ligament (ALL), the posterior longitudinal ligament (PLL), the ligamentum flavum (LF), the interspinous ligament (ISL) and the two capsular ligaments (CLs). In the same model, the upper cervical spine has the continuation of the ALL, the PLL and the two CLs. In addition to these, the alar and cruciate ligaments are modelled to allow for the unique movement between the skull, atlas and axis.

The force that the ligaments exert on the vertebral bodies is proportional to the length of the ligament and only acts in tension. De Jager [32] added a damping component that adds force and expresses it in the following equation

$$F_{Ligament} = \begin{cases} F_e(\epsilon) + b_{Ligament} \times \dfrac{d\epsilon}{dt} & \text{where } \epsilon \geq 0 \\ 0 & \text{where } \epsilon < 0 \end{cases} \tag{2.7}$$

where F_e is the length-dependent elastic force, ϵ is the strain in the ligament and $b_{Ligament}$ is the damping coefficient. De Jager obtained the elastic force from curves that compare the normalised force to the normalised strain for each ligament. These curves all have the same shape and are divided into three straight-line regions with the middle region having the steepest gradient. This implies

that rate of force produced by a unit change in strain increases as the strain increases to a certain point, but then decreases before failure. The damping coefficient is assumed to be a constant 300 N s/m.

The difficulty with modelling the cruciate ligament is that its origin and insertion point are on the same vertebra and it produces its force by wrapping around the odontoid process. To overcome this problem, De Jager [32] treated the ligament as a frictionless belt in the modelling software. This allowed the odontoid process to rotate freely, but limits the appropriate translational displacement.

Van Lopik [34] used the same method of modelling the same six muscles in the lower cervical spine. However, Van Lopik upgraded from using force-strain relationships to using force-deflection curves that are more accurately defined. The damping coefficient was still approximated as 300 N s/m.

Van der Horst [33] used a similar approach to the modelling of the ligaments as the other two models with the most significant adaption being to the force formula. Van der Horst claimed that the damping coefficient should only be valid when the ligament is elongating. This results in a formula that looks as follows

$$F_{Ligament} = \begin{cases} F_e(\epsilon) & \text{where } \epsilon \geq 0 \text{ and } \dfrac{d\epsilon}{dt} \leq 0 \\ F_e(\epsilon)\left(1 + C_{Ligament} \times \dfrac{d\epsilon}{dt}\right) & \text{where } \epsilon \geq 0 \text{ and } \dfrac{d\epsilon}{dt} > 0 \\ 0 & \text{where } \epsilon < 0 \end{cases} \tag{2.8}$$

where $C_{Ligament}$ is a damping coefficient defined differently to $b_{Ligament}$. Van der Horst [33] uses a value of $C_{Ligament}$ equal to 40 for the alar and cruciate ligaments and 0.4 for all other ligaments.

2.2.4 Modelling of Muscles

The detail of muscle models appears to be increasing at a much quicker rate than the other components already discussed. This is seen throughout the three head and neck models previously referenced, where the muscle model changes drastically, but the IV discs and ligaments maintain the same model with newer values.

There are approximately 30 muscle pairs in the neck region, but modelling all of them increases the complexity and execution time of the model. As such it is necessary to select those muscles that contribute most to neck stability. De Jager [32] reduced this number to 13 muscle pairs. Most of his muscles had a single attachment point at each end, but this contradicts the real human body since most muscles in the neck region attach over multiple vertebrae. De Jager made one exception and that is the longus colli muscle which is divided into two. A total of 14 muscle segments were modelled on each side of the neck.

The model by De Jager [32] used simple Hill-type muscles. This means that there are two aspects of each muscle, a contractile element that produces a force to shorten when given an activation signal and an elastic element that acts in

parallel to the contractile element and passively resists lengthening of muscles. The contractile element equation is defined as

$$F_{CE} = q \cdot F_{max} \cdot f_H(v_r) \cdot f_L(l_r) \tag{2.9}$$

where q is the level of activation between zero and one, $f_H(v_r)$ is the normalised force-velocity equation and $f_L(l_r)$ is the normalised force-length equation. The parameter v_r is the dimensionless velocity with respect to the maximum velocity and l_r is the relative length to the muscle's rest length. The value of F_{max} was calculated by assuming all muscles have the same maximum stress and then multiplying this value by the pCSA of the relevant muscle. The elastic component was simply modelled as a non-linear elastic spring dependent on the strain in the muscle.

De Jager [32] listed the two parameters that change between muscles, pCSA and rest length, for each of the muscles used in the models. The other parameters required are constant for all muscles and are listed separately.

Van der Horst [33] used an identical Hill-type model to De Jager [32], but updated many of the values that were used. One major assumption was that no muscle is ever completely at rest and therefore the rest length needs to be scaled slightly. The other significant improvement that Van der Horst made was to include an additional three muscle pairs and to separate all the muscles into multiple segments. This allowed a single muscle to attach at many points on the neck as it does in real life. This new model consisted of a total of 16 muscles and 68 muscle segments on each side.

The model by Van Lopik [34] was also an improvement on De Jager's model in multiple ways. Firstly, Van Lopik included a total of 19 muscles that were subdivided into 69 segments. Next, these muscles curved around the neck by means of using intermediary points which resulted in the total muscle length and the direction of the force being more accurate. Finally, this model calculated the force that muscles produce in a Simulink model. The software that built the dynamic model exported the length of each muscle to Simulink and received the force of each muscle in return [39].

The Simulink model was based on an expanded form of the Hill-type muscle model that included a serial elastic element next to the contractile element and parallel elastic element combination [40]. The serial elastic element represented the tendon which attaches between the muscle and the bone and therefore the total length of the muscle was divided into the length of the contractile element and the length of the tendon. Each muscle consisted of both fast twitch and slow twitch cells in various ratios and this combination affected the maximum muscle velocity [40]. The other parameters that were muscle-segment specific were the contractile element length, the tendon length and the pCSA. All these parameters were incorporated in the Simulink muscle model through complex equations based on the same principals used in De Jager.

A newer Simulink model was developed by Haeufle *et al.* [41]. This model further expanded on the Hill-type muscle by including a damping element in

parallel with the series elastic element as shown in Figure 2.7. While this model does not account for fast and slow twitch muscle fibres, the added complexity of the damping does account for other velocity-dependent factors [41]. This muscle model also specifically considered the asymmetric effect that an increasing muscle length has on the force produced [41]. The model was initialised using the lengths of the contractile element and tendon, the maximum force that can be produced and a number of parameters constant to all muscles. During simulation, the muscle model receives the total muscle length, muscle velocity and activation level and outputs the total force that the muscle produces [41]. This newer model can be incorporated in a dynamic simulation in the same way that van Lopik and Acar [39] applied it.

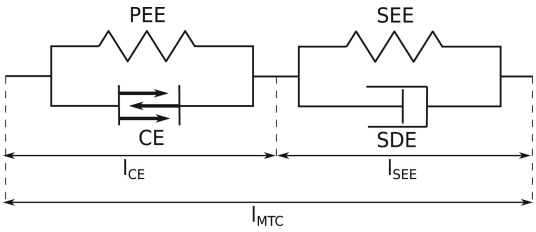

Figure 2.7: Hill-type muscle diagram (Image from: Haeufle *et al.* [41])

2.2.5 Validation of Model

There are two components to validating a head and neck model. The first is to verify that the individual segments, for example between two successive vertebrae, respond correctly to static loads and the second is to check that the full model behaves as expected during dynamic simulation [32; 33; 34].

Static load testing of the lower cervical spine elements involved fixing the lower of two vertebrae and applying a force or moment in each of the possible directions while no muscles were attached. All three of the models that have been discussed selected the C3-C4 and C5-C6 vertebrae to act as representatives of the lower cervical spine [32; 34; 33]. The linear or angular displacement was measured for each of the possible forces and compared to known results. The three models were all validated against data presented in Moroney *et al.* [36] for small loads. The vertebral segments were also validated against large loads where each direction of motion should not exceed a specified displacement value immaterial of the load magnitude. These displacement values were taken from White and Panjabi [42]. A newer source which is comparable with White and Panjabi [42] is Wheeldon *et al.* [43], but Wheeldon *et al.*'s data indicates that the cervical spine should have a greater range of motion than that which is reported by White and Panjabi. Wheeldon *et al.* claims that this is due to younger specimens showing a greater range of motion in flexion.

Validation of the upper cervical spine was completed using all three specified bodies. The axis was fixed and forces and moments were applied to the occiput

in the same manner as the lower cervical spine tests [32; 34; 33]. The linear and angular displacement were measured and then compared to the data from Oda *et al.* [44].

Dynamic verification took place on the completed model with all the muscles attached. The aim of this analysis was to verify that the motion of the solid bodies remain within specific bounds. Both Van der Horst [33] and Van Lopik and Acar [45] applied a changing angle and acceleration to the first thoracic vertebra to match the conditions that this vertebra experienced during a frontal impact as defined by Thunnissen *et al.* [46]. Thunnissen *et al.* defined reaction corridors for various measures of the head and neck during a frontal collision that Van der Horst and Van Lopik and Acar tried to match with their models.

The reaction corridors for frontal collisions by Thunnissen *et al.* [46] is based on nine sled tests using human volunteers conducted at the Naval BioDynamics Laboratory in New Orleans. Using a combination of accelerometers and high-speed camera footage, the displacements and accelerations of the first thoracic vertebra, the OC and the head's centre of gravity (CG) were obtained. A total of 11 corridors are defined based on the measured data. Firstly, the head link angle and neck link angle are defined as the angles measured from the vertical to lines joining the T1's CG to the OC and the OC to the head's CG, respectively. Both these angles are graphed against time, as well as against each other. Next, the corridors relating to the trajectory in the x- and y-axes are plotted, followed by the length of the neck against time. Two corridors exist which define the head's CG's linear acceleration in the mid-sagittal plane and angular acceleration about the z-axis. Finally, the OC's axial force, shear force and moment are calculated based on the measured acceleration and are plotted against time. The 11 corridors are used to fully validate the model under dynamic loading conditions.

2.3 Anthropomorphic Test Devices (ATDs)

During the 1950s, research determined that many fatalities were as result of secondary impacts sustained by occupants. This prompted the design of Anthropomorphic Test Devices (ATDs) with the intention that these devices should be used to evaluate restraint technology. Currently there are two Anthropomorphic Test Devices (ATDs) that are used for frontal impact assessment, namely the Hybrid III and the Test device for Human Occupant Restraint (THOR) [47]. Even though the THOR is the successor to the Hybrid III, the Hybrid III is still the most-used ATD for frontal impact analysis and will thus be modelled in this project [48].

2.3.1 Structure

The Hybrid III head and neck model was designed as three separate assemblies joined via an OC joint between the head and the neck and a solid joint between the neck and the mounting bracket. The response of the head and neck is dependent on the components of the neck and the OC joint, since the head and

mounting bracket are both solid. The purpose of the mounting bracket is to join the neck to the torso of the ATD.

The neck consists of five aluminium plates that represent the vertebrae of the neck. These plates are moulded within a block of butyl elastomer to form a single component [49]. Two of the aluminium plates are located at either end of the neck to provide attachment points. The butyl elastomer allows for flexion and extension of the neck, while also providing suitable damping during collision responses [49]. A steel cable is located at the centre of the neck to provide the required tension resistance during testing.

The head consists of a cast aluminium part with accurate human geometry, weight and inertial properties [49]. The OC joint attaches the head to the neck via a pin to allow rotation within the sagittal plane. Rotation within the sagittal plane is controlled by rubber blocks located posteriorly and anteriorly of the pin. The rubber blocks resist compression and attempt to maintain the head in its resting position. The head is fitted with a three-axis accelerometer within the its cavity and a force transducer is located between the OC joint and the base of the head [49]. Both these measurement devices may be used to calculate the risk of injury.

Both Spittle *et al.* [50] and Deng [51] attempted to describe the non-linear relationship between applied moments and the resulting angular deflection. Deng [51] reported these relationships as an angular spring constant and a constant damping value, while Spittle *et al.* [50] summarised the relationships in third-order polynomial equations. Both these sets of results may prove useful in the process of developing the model.

2.3.2 Validation

The validation process intends to determine how well a model matches that which it was designed to mimic by comparing the model's response to real-world targets. In the case of the Hybrid III, the neck calibration test could be used as a target since the calibration test is used to verify that the Hybrid III's neck reacts similarly to a human neck and therefore has clearly-defined response requirements. The calibration test involves mounting the head and neck to a pendulum in an inverted position [52]. The pendulum is used to provide a specific acceleration profile and initial velocity to the base of the neck, while the forces, moments and accelerations are measured by the force transducer and accelerometer. The calibration test provides targets in terms of the magnitudes and durations that need to be attained [52].

In addition to the calibration test, other authors have published articles that have relevance to the head and neck response of a Hybrid III ATD. Firstly, Mertz and Patrick [53] published safety corridors relating the rotation of the head to the moment at the OC. These corridors were used as design requirements for Culver *et al.* [54] in developing a mechanical neck and this neck was the precursor to the Hybrid III neck. Therefore, it would be important to validate the neck against the

safety corridors. Secondly, Zhang *et al.* [55] performed inverted pendulum tests with the Hybrid III and reported the angle of the head relative to the torso for the full duration of the test. Combining these different validation requirements may prove useful in designing a more robust model.

2.4 Head and Neck Restraint (HNR) System

The HNR system aims to reduce injuries to the head-and-neck region by limiting the head's range of motion. The initial design of such a device was patented by Hubbard in 1987 [56]. Hubbard specifically mentioned that this device is to protect any person operating a high-performance vehicle, not only racing car drivers. This HNR system has become known as the Head and Neck Support (HANS) device. Gramling *et al.* [57] summarised the design by saying, "A HANS device is worn on a driver's upper torso and is restrained with the torso by the shoulder belts. Tethers from the driver's helmet to the HANS restrain the head relative to the torso." Figure 2.8 shows a photo of a HANS device where the indentation for the shoulder belts can be seen, as well as a tether extending from the back of the device.

Figure 2.8: Image of a HANS device (Image from: Tiger Performance [58])

The initial HANS device was bulky and had trouble fitting into the cockpit of open-wheel racing cars [57]. As a result, the drivers were reluctant to use such a device and the FIA funded research into improving the HANS device. Gramling *et al.* [57] redesigned the HANS device for user comfort in a open-wheel car. The new design was tested against the original model and, despite its reduced size, the new design provided even greater safety benefits.

Shortly after the redesign of the HANS device, the FIA investigated using airbags mounted within the cockpit. Gramling and Hubbard [59] conducted this research which determined that both the HANS device and the airbag provided the same level of protection and that the use of both devices simultaneously did not provide any additional protection. Gramling *et al.* concluded with two observations. The first is that the HANS device had the advantage of constraining the driver's head to their body and therefore the relative velocity of the head to the restraining device is lower. The second is that the airbag system will require a new

design of a triggering mechanism to ensure that the airbag only deploys during a critical collision. As such, Gramling and Hubbard determined funding should be focused on the HANS device and this has become the standard neck protection throughout all racing. Since the tether is a non-negotiable piece of gear, the FIA defines the requirements of the tether system in Standard FIA 8858-2010 [2].

Recently Kaul *et al.* [60] presented a summary of the effects that the HANS device has had on the racing world. Kaul *et al.* described how the device reduces both tensile and shear loading in the upper cervical spine. Data collected during the last eight seasons of stock-car racing in North America shows how the HANS device protected drivers since no serious neck injuries were recorded [61]. The last racing fatality related to neck injuries was recorded in 2001 [60].

2.5 Optimisation Algorithms

Mathematical optimisation is the process of formulating and solving an optimisation problem that is in a specific form. This form includes the objective function which needs to minimised or maximised and the design variables that are altered during the optimisation process [62]. The final component required for optimisation is an algorithm which iteratively alters the design variables until the minimum or maximum objective function value is found. This section will specifically consider the components related to Bayesian optimisation.

2.5.1 Bayesian Optimisation

Engineering models are often described as black-box functions since the computation between giving an input and receiving an output is unknown. These functions often require long simulation durations or significant computational power. Therefore, it is essential to find optimisation algorithms that require fewer function evaluations [63].

One group of black-box optimisation algorithms attempt to fit a surrogate model to a set of sampled points such that the optimal value can easily be determined from the surrogate model [64]. These algorithms involve selecting a suitable function consisting of multiple parameters such that once the parameters have been tuned, the function may best approximate all the sampled points. The optimisation procedure then follows that a new point should be selected to be sampled according to the fitted function and then the parameters should be retuned to incorporate the newly-sampled point.

One method of finding the optimal value generated by a black-box function using a surrogate model is referred to as Bayesian optimisation. Bayesian optimisation relies on building a statistical model using Gaussian Process (GP) based on the sampled points. An acquisition function then selects the next point based on the mean and standard deviation predicted by GP. The process of building a GP model and sampling a new point is repeated until some stopping criteria is reached and the optimal point is determined.

Majority of engineering optimisation problems are constrained problems. Since their are no constraints acting between the variables of this system, this optimisation problem differs from most engineering optimisation problems. However, this also makes the problem well-suited for the Bayesian optimisation algorithm, since this algorithm is designed for unconstrained optimisation.

2.5.2 Gaussian Process

The first step of Bayesian optimisation involves building a GP model. GP allows a limited set of sampled points to be converted into a prediction for all points within the ranges of each of the variables. Not only is a prediction of the value made, but the standard deviation at each predicted point is also determined. Both the predicted value and the standard deviation are determined using a covariance function. The covariance function defines the relationship between two points and this relationship is used to predict any other points. The mean and standard deviation formulas are given in Equations 2.10 and 2.11, respectively, where k is the covariance function, X_* is the points that need to be predicted, X is the points that have already been sampled, $\boldsymbol{\theta}$ is the set of parameters specific to the covariance function and $\boldsymbol{y}$ is the output values at the sampled points.

$$f(X_*) = k(X_*, X, \boldsymbol{\theta}) \times k(X, X, \boldsymbol{\theta})^{-1} \times \boldsymbol{y} \tag{2.10}$$

$$\sigma^2(X_*) = k(X_*, X_*, \boldsymbol{\theta}) - k(X_*, X, \boldsymbol{\theta}) \times k(X, X, \boldsymbol{\theta})^{-1} \times k(X, X_*, \boldsymbol{\theta}) \tag{2.11}$$

It is expected that points which are close together should have similar values and the covariance function needs to indicate this. Therefore, most covariance functions start with a value of one when the distance between points is zero and continually decrease as the distance increases. One of the most common covariance functions is the squared exponential function shown in Equation 2.12 [65]. This function is dependent on a single parameter l which controls the shape of the function.

$$k(x_*, x) = \exp\left(-\frac{|x_* - x|^2}{2l^2}\right) \tag{2.12}$$

An argument is made that this covariance function results in unrealistically smooth predictions and that the Matérn class of covariance functions should be used [65]. Matlab's built-in Bayesian optimisation algorithm uses the automatic relevence determination (ARD) Matérn 5/2 function which is defined in Equation 2.13 since Snoek *et al.* [66] specifically suggests this covariance function as an alternative for the squared exponential function.

$$k(x_*, x, \boldsymbol{\theta}) = \sigma_f^2\left(1 + \sqrt{5r^2} + \frac{5r^2}{3}\right)e^{-\sqrt{5r^2}} \text{ where } \begin{cases} r^2 = \sum_{m=1}^{d} \dfrac{(x_{*m} - x_m)^2}{\sigma_{Lm}} \\ \sigma_L = e^{\theta_{1:d}} \\ \sigma_f = e^{\theta_{d+1}} \end{cases} \tag{2.13}$$

The variable d in this equation is the total number of dimensions and $\boldsymbol{\theta}$ is an array of parameters with a length that is one more than the number of dimensions. The ARD component of the covariance function provides each of the dimensions with a separate parameter that determines its dependence and therefore allows each dimension to have a different level of contribution to the covariation function [67].

Given that the new points and the sampled points in Equation 2.10 are the same, the predicted values need to equal the sampled values, but this is only possible if the covariance function's parameters are correctly selected. Rasmussen and Williams [65] state that the optimal parameter values can be determined by maximising the log marginal likelihood given in Equation 2.14, where n is the number of sampled points. Since both the partial derivatives for the log marginal likelihood and the covariance functions can be calculated, a gradient-based optimisation algorithm can be employed to determine the optimal parameter values.

$$\log p(\boldsymbol{y}|X;\boldsymbol{\theta}) = -\frac{1}{2}\left[\boldsymbol{y}^T k(X,X,\boldsymbol{\theta})\boldsymbol{y} + \log|k(X,X,\boldsymbol{\theta})| + n\log(2\pi)\right] \tag{2.14}$$

2.5.3 Acquisition Function

The next step in Bayesian optimisation is to determine where next to sample based on the GP model. It is possible to sample throughout the search space and in this way build a very accurate GP. However, the aim of Bayesian optimisation is to find the optimal point and therefore only points near where the optimal is believed to be, should be sampled [68]. These points are selected according to an acquisition function.

One option for the acquisition function is referred to as the Probability of Improvement (PI). Equation 2.15 provides the PI where CDF is the normal cumulative distribution function [68]. The acquisition function states that the next point to be sample should be the point that yields the greatest PI. The problem with this acquisition function is that it does not take into account how much the improvement may be and therefore has a tendency to become trapped in a local minimum [69].

$$PI(\boldsymbol{x}) = CDF\left(\frac{f(\boldsymbol{x}_{best}) - f(\boldsymbol{x})}{\sigma(\boldsymbol{x})}\right) \tag{2.15}$$

An alternative acquisition function is called Expected Improvement (EI). Equation 2.16 states the formula used for calculating EI where CDF is the normal cumulative distribution function and PDF is the probability density function [68]. The first term of the equation suggests that the EI will be great if a significant improvement is predicted by the GP model, while the second term indicates that the EI will be great if there is a high uncertainty [68]. While no acquisition function will always outperform all other functions, the EI function

appears to result in quicker convergence than the PI function [68; 69].

$$\begin{aligned} EI(\boldsymbol{x}) &= \left(f(\boldsymbol{x}_{best}) - f(\boldsymbol{x})\right) \times CDF(Z) + \sigma(\boldsymbol{x}) \times PDF(Z) \\ \text{where } Z &= \frac{f(\boldsymbol{x}_{best}) - f(\boldsymbol{x})}{\sigma(\boldsymbol{x})} \end{aligned} \tag{2.16}$$

Chapter 3

ATD Model

The Hybrid III ATD makes use of a combination of solid and deformable elements to model a human head and neck. The solid elements provide structure while the deformable elements control the model's response. This chapter starts with a discussion on the development of the ATD model before concluding with its validation.

3.1 Solid Elements

The solid elements of the Hybrid III model consist of all the parts in the head and neck region of the ATD that are made from metal. These consist of five aluminium plates stacked vertically with spaces between each as shown in Figure 3.1. The lowest of these plates attach solidly to an aluminium bracket that acts as a connector between the torso and neck. The topsmost plate attaches solidly to the aluminium nodding joint that allows the head to tilt about a pin. Finally, the neck transducer attaches between the nodding joint and the head. The nodding joint connection is through the pin, whereas the head is connected solidly.

A total of 14 solid bodies were identified and included in the model. The complete list of these elements is included in Table 3.1 and they are shown in Figure 3.1. The bodies were constructed in Autodesk Inventor 2018 based on the drawings of the Hybrid III ATD [52]. The only exception was the actual head, since the drawings include the dimensions for machining and therefore the general shape's dimensions were estimated.

The CG was calculated by assuming that each of the bodies have a uniform density. As such, the CG is equal to the centre of volume determined by

$$CG_X = \frac{\int_0^V x\,dv}{V} \tag{3.1}$$

where V is the volume of the element in question. The CG of each solid body is included in millimetres in Table 3.1.

The mass of each solid body was calculated as the product between the part's density and its volume. All the masses are recorded in kilograms in Table 3.2. Table 3.2 also includes the moments of inertia (I) for each of the elements in all

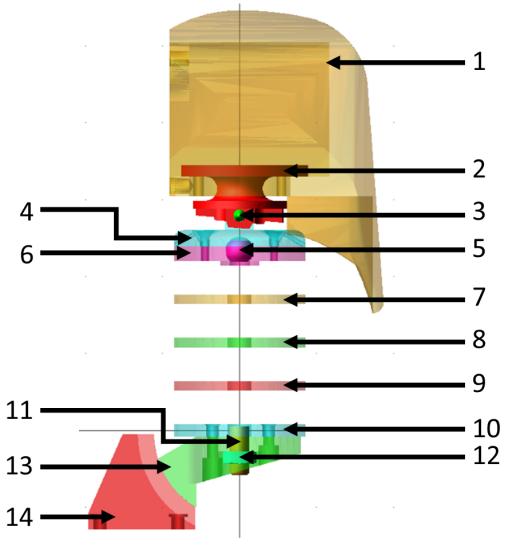

Figure 3.1: Image of ATD head and neck model with numbered solid bodies

Table 3.1: Full set of solid bodies for the ATD model and their centre of gravity locations (m)

Body No.	Name	CG_X	CG_Y	CG_Z
1	*Head*	20.8×10^{-3}	205.2×10^{-3}	0.0
2	*Neck_Transducer*	1.3×10^{-3}	158.3×10^{-3}	0.0
3	*Pivot_Pin*	0.2×10^{-3}	139.6×10^{-3}	2.3×10^{-3}
4	*Nodding_Joint*	0.0	125.1×10^{-3}	0.0
5	*Mount_Plate_Upper*	0.0	114.8×10^{-3}	0.0
6	*Cord_Ball*	0.0	116.7×10^{-3}	0.0
7	*IV_Plate_3*	0.0	85.2×10^{-3}	0.0
8	*IV_Plate_2*	0.0	57.0×10^{-3}	0.0
9	*IV_Plate_1*	0.0	28.9×10^{-3}	0.0
10	*Mount_Plate_Lower*	-0.03×10^{-3}	0.0	0.0
11	*Cord_Thread*	0.0	-12.9×10^{-3}	0.0
12	*Nut*	0.0	-17.6×10^{-3}	0.0
13	*Neck_Bracket_Cervical*	-11.8×10^{-3}	-17.9×10^{-3}	0.0
14	*Neck_Bracket_Thoracic*	-62.7×10^{-3}	-44.2×10^{-3}	0.0

Table 3.2: Masses (kg) and moments of inertia (kg m^2) for the ATD model's solid bodies

Body No.	Name	Mass	I_{XX}	I_{YY}	I_{ZZ}
1	*Head*	4.315	13.8×10^9	20.6×10^9	21.0×10^9
2	*Neck_Transducer*	0.221	107.7×10^6	145.0×10^6	102.5×10^6
3	*Pivot_Pin*	0.007	1.6×10^6	1.6×10^6	48.0×10^3
4	*Nodding_Joint*	0.141	67.5×10^6	124.4×10^6	61.6×10^6
5	*Mount_Plate_Upper*	0.143	68.0×10^6	133.6×10^6	68.0×10^6
6	*Cord_Ball*	0.007	205×10^3	234×10^3	205×10^3
7	*IV_Plate_3*	0.095	45.5×10^6	90.3×10^6	45.5×10^6
8	*IV_Plate_2*	0.095	45.5×10^6	90.3×10^6	45.5×10^6
9	*IV_Plate_1*	0.095	45.5×10^6	90.3×10^6	45.5×10^6
10	*Mount_Plate_Lower*	0.113	54.4×10^6	108.2×10^6	54.9×10^6
11	*Cord_Thread*	0.011	992×10^3	215×10^3	992×10^3
12	*Nut*	0.013	585×10^3	878×10^3	585×10^3
13	*Neck_Bracket_Cervical*	0.308	150.2×10^6	278.9×10^6	185.9×10^6
14	*Neck_Bracket_Thoracic*	0.333	307.0×10^6	307.8×10^6	197.7×10^6

three dimensions. The moment of inertia was calculated using the formula

$$I = \int_0^M r^2 \, dm$$

where M is the total mass of the body and r is the perpendicular length between the chosen axis and the infinitesimal mass for integration.

The CG, mass and moments of inertia of the head were obtained from Yoganandan *et al.* [70]. Yoganandan *et al.* provided the CG relative to the OC, which was located based on the neck transducer and the machining drawing of the head.

The solid bodies were imported into MSC Adams such that their CGs match that which is defined in Table 3.1. The properties of each body were defined according to Table 3.2. Contact forces were initialised between bodies that will move relative to each other so that two bodies cannot accidentally pass through each other.

3.2 Deformable Elements

Deformable elements are found between the solid elements and define how the solid elements translate and rotate relative to each other. The deformable elements are comprised of four rubber discs, two rubber *Nodding_Blocks*, one bushing between the head and the neck and a stainless steel cord that runs through the centre of the discs.

Each of the rubber discs are represented by an MSC Adams bushing constraint and two springs, as shown in Figure 3.2. The springs rely on force de-

flection curves derived from Spittle *et al.* [50]. Spittle *et al.* provided curves based on experimental data that relates the moment produced by the rubber discs to the difference in angle of the head. Assuming that the two springs in Figure 3.2 only act in compression, the force-deflection curves were calculated based on the horizontal displacement between the CG and the connection point of each of the springs. These springs are thus responsible for resisting compression in the y-axis as well as preventing bending about the z-axis. The compression resistance in the y-axis can be increased by placing the springs closer the CG of each of the aluminium plates, while the moment generated by the spring will remain the same.

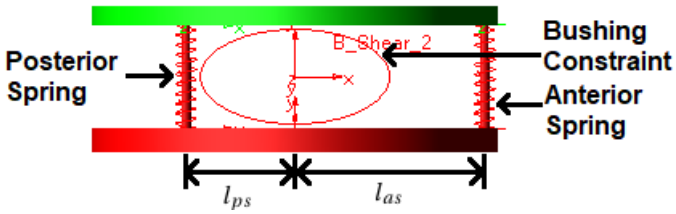

Figure 3.2: Springs and bushing constraint representing the rubber disc

The bushing constraint represents three translation springs along each of the axes, as well as three torsion springs about each of the axes. Each of these represented springs are able to be defined by unique spring constants. Since the translational motion in the y-axis and angular motion about the z-axis are already accounted for by the anterior and posterior springs, the spring coefficients in the bushing constraint are set to zero. The remaining four spring coefficients are set to the values indicated in Table 3.3. However, since the model assumes only frontal impacts, planar constraints are included between each of the aluminium plates such that the z-translational and x- and y-rotational bushing constraints are redundant.

Table 3.3: Spring constants representing the rubber disc

Name			Symbol	Value	
Anterior Spring			k_a	Flexion curve	
Posterior Spring			k_p	Extension curve	
Bushing	Constraint	x Translational	k_{tx}	1.65×10^6	N/m
		y Translational	k_{ty}	0.00	N/m
		z Translational	k_{tz}	1.65×10^6	N/m
		x Rotational	k_{rx}	12.12	N m/deg
		y Rotational	k_{ry}	3.90	N m/deg
		z Rotational	k_{rz}	0.00	N m/deg

The spring coefficients were calculated by assuming that the rubber discs are perfectly cylindrical and made of Butyl rubber with material properties as de-

fined in Forsythe [71]. This assumption was made since these are only initial values that will be tuned according to testing. The translational spring coefficients in the x- and z- directions assume that there is no slipping between the rubber discs and the aluminium plates and therefore all translation is as a result of the rubber disc deforming. This rubber disc was then seen as a beam and the relationship between force and deflection was determine as in Appendix B. Continuing in this line, the torsional spring coefficient about the y-axis was based on the formula that calculates the angle of twist of a cylindrical beam. Finally, the torsional spring coefficient about the z-axis was calculated relative to the moment generated by the reaction force of the rubber disc when compressed. The assumed linear relationship between the moment and the angle was calculated along with the other spring constants in Appendix B. Since these values represent the initial estimates, it was decided not to conduct physical testing of the rubber discs and to rely on the tuning process to obtain the best suited values. Therefore, the main benefit of physical testing would only have been to conduct a comparison between the measured results and the tuned values which was not the aim of this project.

The next deformable element is the bushing interface that connects between the head and the neck. To achieve this connection, the *Pivot_Pin* (body three of Figure 3.1) was fastened to the *Neck_Transducer* (body two of Figure 3.1) and a bushing encompasses the *Pivot_Pin*. The opposite surface of the bushing makes contact with the *Nodding_Joint* (body four of Figure 3.1). The bushing was given translational spring coefficient values for the x- and y-axes. The remaining four dimensions were assigned spring coefficient values of zero since the torque in the z-axis will be accounted for by the *Nodding_Blocks* and a planar constraint prevents the pin from moving out of plane relative to the *Nodding_Joint*.

The second pair of deformable elements are the two rubber *Nodding_Blocks* that are located between the *Nodding_Joint* and the *Neck_Transducer*, which are connected by a pivot joint. To provide stability to the head, one *Nodding_Block* was placed anteriorly to the pin connection, while the other block was placed posteriorly. Deng [51] provided a curve relating the moment induced by the *Nodding_Blocks* to the angle of the *Neck_Tranducer* relative to the *Nodding_Joint*. This curve was transformed into a force-deflection curve that was used to define the properties of both springs that represent the *Nodding_Blocks*. Similar to the rubber discs, these springs only apply a force in compression and the springs are located at a specific horizontal length from the pin to ensure the relationship provided by Deng is maintained.

The final deformable element is the cord that runs through the centre of the assembly. For the purpose of this model, this cord would attach between the *Cord_Ball* (body six of Figure 3.1) and *Cord_Thread* (body 11 of Figure 3.1) which are both solid bodies. The cord was modelled as a spring with its total length equal to the curved length following the centres of the aluminium plates. The force on the *Cord_Ball* acts in the direction of the centre of *IV_Plate_3*. The spring constant was calculated in Appendix B by assuming the definition of Young's

modulus is applicable and equal to 193 GPa as defined for stainless steel. This resulted in a spring constant equal to 87,832 MN/m.

Each of the elements were assigned damping coefficients to ensure forces do not become unmanageable. Excessive forces may result in the simulation oscillating and creating unusable results.

Prior to validation, the modelling parameters needed to be adjusted so that the model may pass validation. A detailed description of this process is discussed in Appendix C. This process started by identifying seven parameters that affect the response of the model and then determining which parameters have the greatest effect. The process continued with identifying two targets for which the response of the model should aim. These targets were Zhang *et al.* [55] and Mertz and Patrick [53] for which head angular deflection and OC moments were tuned, respectively. Each of the tuning iterations were manually conducted such that the choices of parameter values remains within logical bounds. The combination of the manual tuning process and the multiple tuning targets should prevent the parameter values from deviating towards values that do not make physical sense. It was determined that the parameter values in Table 3.4 and Figure 3.3 result in a model which sufficiently matches the specified targets.

Table 3.4: Tuned values of parameters for the ATD model

Variable	Tuned Value	Units
Location of Anterior Springs for Rubber Discs	55.00×10^{-3}	m
Central Cord Spring Coefficient	878.32×10^{3}	N/m
Damping Coefficients for Rubber Springs	2.20×10^{3}	N s/m
Locations of Head Springs for Nodding Blocks	18.75×10^{-3}	m
Location of Posterior Springs for Rubber Discs	20.00×10^{-3}	m
Translational Spring Constant for Bushing	1.00×10^{6}	N/m

3.3 Validation

The validation of the model was completed using the neck calibration test prescribed for the Hybrid III in 49 CFR 572 [52]. This test uses a pendulum and indicates the collision conditions of the pendulum, the angle of the head and the moment about the OC.

With respect to the collision conditions, 49 CFR 572 [52] indicates that the accelerometer on the pendulum arm has a velocity between 6.89 m/s and 7.13 m/s at the moment of impact. The validation test had a impact velocity 7.05 m/s which is within the requirements. Furthermore, the acceleration of the pendulum arm's accelerometer needs to measure between three different ranges at three different time stamps, as indicated in red on Figure 3.4. Finally, the descent of the acceleration pulse to 5 G should occur between 34 ms and 42 ms which is

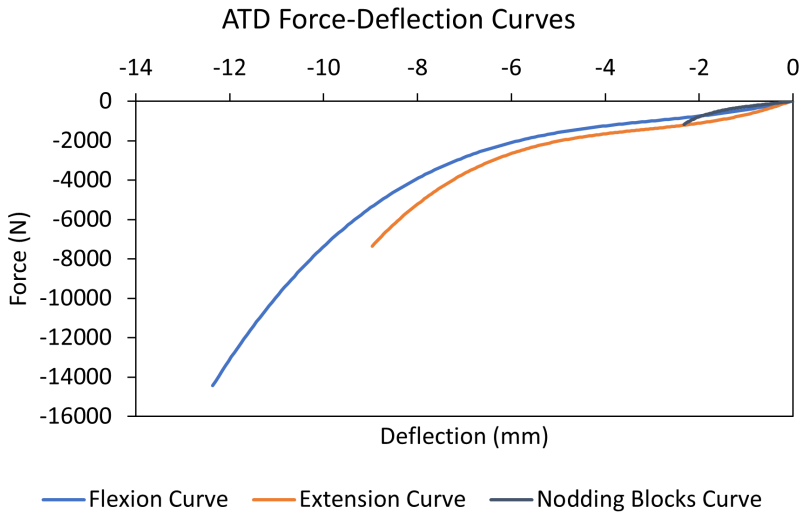

Figure 3.3: Force-deflection curves for the non-linear spring elements in the ATD model

also indicated in red on Figure 3.4. The measured acceleration pulse for the test is superimposed in blue on Figure 3.4 and passes through all requirements.

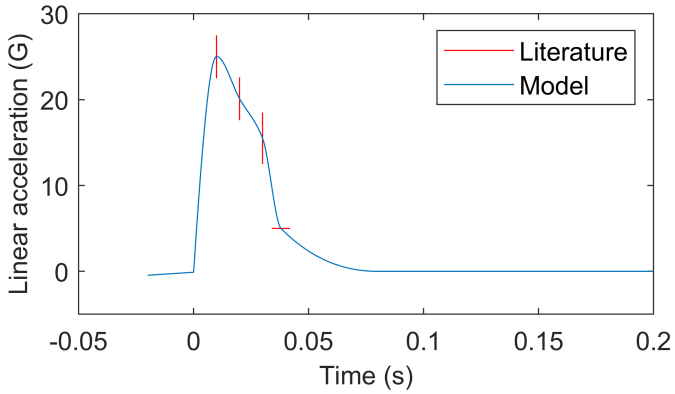

Figure 3.4: Linear acceleration of pendulum arm at location of specified accelerometer during collision, with calibration target values indicated in red

The next set of conditions that 49 CFR 572 [52] imposes is with respect to the angle of the head. The text specifies that the maximum angle of the head should be between 64 degrees and 78 degrees at a time between 57 ms and 64 ms. Also, the angle of the head should cross the zero degree line between 113 ms and 128 ms. These conditions are respectively indicated on Figure 3.5 as a red square and a red line. The measured angle of the head from the model is superimposed on Figure 3.5 and is seen to pass through the required zones even though they are near the time boundaries.

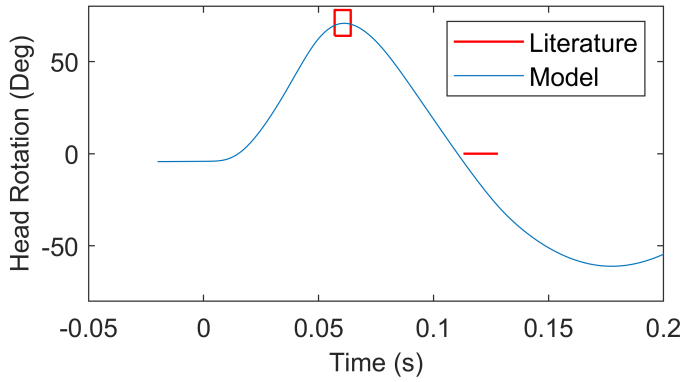

Figure 3.5: Angle of the head relative to the base during deceleration with calibration target values indicated in red

The final set of conditions required by 49 CFR 572 [52] concerns the moment about the OC. These requirements state that the maximum moment should be between 88.13 N m and 108.47 N m at a time between 47 ms and 58 ms and that the moment should return through zero between 97 ms and 107 ms. These requirements are indicated in red on Figure 3.6. The moment measured by the model is superimposed on Figure 3.6 as a blue line. This shows that the model achieves the maximum moment during the specified time, but the moment reduces to zero faster than required. The argument can be made that since the maximum moment is within the required range, it will be acceptable for calculating the NIC.

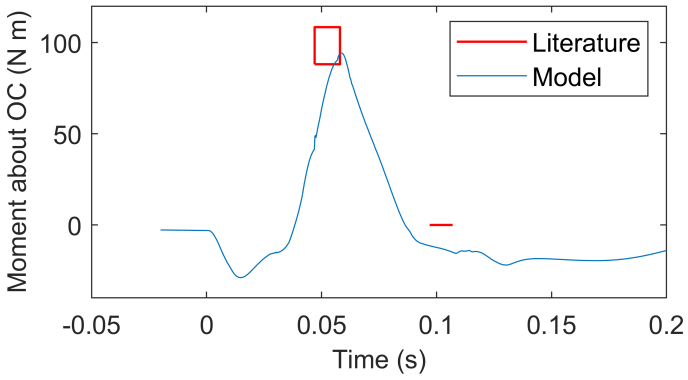

Figure 3.6: Moment about the OC during deceleration with calibration target values indicated in red

To conclude, the validation of the model attains all but one of the neck calibration requirements. This is undesirable, but should not have a significant effect on calculating the NIC. As such, it is believed that model is sufficient for further work.

Chapter 4

Human Model

A model of the human head and neck is required to be able to test the effect of changing the tether angle of the HNR. This model should be representative of a human and therefore needs to be validated against human data. This chapter considers the components that were used to build the model, as well as how the model was validated.

4.1 Solid bodies

The solid bodies of the human head and neck model consist of nine elements. These elements were obtained from the BodyParts3D [72] database which was created by Mitsuhashi *et al.* [73]. Mitsuhashi *et al.* obtained the required three-dimensional parts from Nagaoka *et al.* [74]. Nagaoka *et al.* used a full-body Magnetic Resonance Imaging (MRI) scan of a volunteer (22 years old, 172.8 cm tall and 65.0 kg in mass), with individual slices taken at 2×10^{-3} m intervals. The slices were analysed by medical staff to identify the various tissue layers and a full-body model was constructed based on these layers.

Each of the eight vertebrae were downloaded as individual wavefront files (with the file extension ".obj") containing the bones' structure. A local coordinate system was defined for each vertebra where the origin was placed at the geometric centre of the vertebral body, as shown in Figure 4.1. The X'-axis was defined in the mid-sagittal plane as the line joining the geometric centre to a point on the anterior surface of the vertebral body that is midway between the inferior and superior surfaces. The Y'-axis was set to point in the direction of the superior surface while being parallel to the mid-sagittal plane and the Z'-axis was set in accordance with the right-hand rule based on the X'- and Y'- axes. The vertebrae are shown in Figure 4.2.

The global coordinate system originates at the same point as the first thoracic vertebra's origin. The X- and Y-axes act in the mid-sagittal plane, with the positive Y-axis pointing in the opposite direction to gravity and the positive X-axis pointing forward. Since the wavefront files define the locations of the vertebrae in terms of the global coordinate system, the locations of each of the vertebrae were manually measured as the displacements from the global coordinate system to the vertebrae's local coordinate system origin. These locations are listed in Table 4.1. This table also provides the angle between global and local coordinate systems so that the vertebrae may be orientated correctly. Finally, De Jager

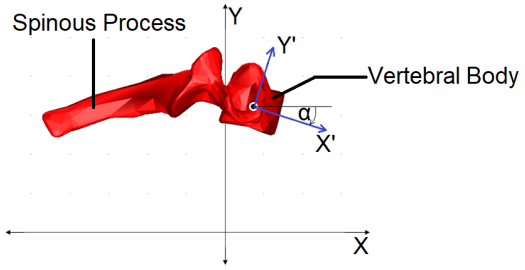

Figure 4.1: Lateral view of a vertebra with global and local axes indicated

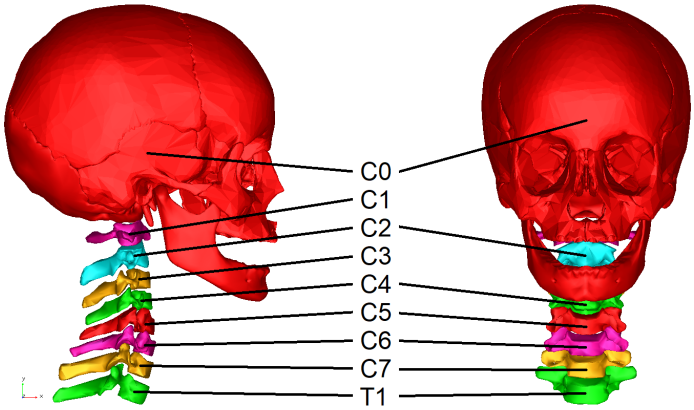

Figure 4.2: Lateral (left) and frontal (right) view of all vertebrae and the head

[32] assumed that the centre of gravity (CG) is located on the posterior surface of the vertebral body in line with the X'-axis. Under the same assumption, the locations of the CGs were listed in Table 4.1 with respect to the local coordinate system.

Table 4.1: Position of each body relative to the global axes and the CG relative to the body's axes in m. "C0" is the occipital bone and, by extension, the head.

	Body relative to global axis			CG relative to body axis	
Body	X	Y	α	X'	Y'
T1	0.0	0.0	25.93	-8.6×10^{-3}	0.0
C7	4.4×10^{-3}	17.2×10^{-3}	19.20	-7.6×10^{-3}	0.0
C6	7.5×10^{-3}	32.5×10^{-3}	17.67	-7.0×10^{-3}	0.0
C5	7.4×10^{-3}	47.1×10^{-3}	13.42	-7.0×10^{-3}	0.0
C4	5.6×10^{-3}	64.3×10^{-3}	−3.42	-6.8×10^{-3}	0.0
C3	4.0×10^{-3}	79.7×10^{-3}	−2.03	-6.8×10^{-3}	0.0
C2	1.3×10^{-3}	98.2×10^{-3}	4.78	-6.8×10^{-3}	0.0
C1	-4.7×10^{-3}	114.8×10^{-3}	−8.65	-8.8×10^{-3}	0.0
C0	-17.2×10^{-3}	129.0×10^{-3}	0.00	42.6×10^{-3}	37.5×10^{-3}

The head of the model consists of 13 wavefront files of different bones that are merged to form the solid body. The local coordinate system was defined similarly

to that of the vertebrae and the origin of the coordinate system is placed at the centre of the foramen magnum. The location of the head and its CG is provided in Table 4.1.

In contrast with using the wavefront files, both De Jager [32] and Van Lopik [34] needed to construct their own vertebrae in Computer Aided Drawing (CAD) software using dimensions determined by Nissan and Gilad [35]. In comparison with Nissan and Gilad's data, the vertebrae contained in the wavefront files are on average 15 % smaller. This indicates that using the wavefront vertebrae will result in a model where the maximum possible forward extension of the head will be less than that which is predicted by De Jager [32] and Van Lopik [34].

The masses of each of the vertebrae and the head, as well as their moments of inertia, are listed in Table 4.2. These parameters were calculated by van Lopik and Acar [39] while assuming that a straightened neck can be represented by a cylinder. These assumptions were based on an article describing the process of determining the mass and volume of the neck. Using a total neck mass of 1.63 kg and an average density of 1170 kg/m^3, the volume is calculated to be 1.39×10^{-3} m^3. This volume is assumed to have a constant radius which was calculated based on the total height of the assumed cylinder. The cylinder was then subdivided according to the height of each of the vertebrae and, making use of the known CG of each vertebra, the moments of inertia were calculated. As such, the masses and moments of inertia account for the tissue surrounding the vertebrae. The T1 body was not assigned a mass since it will be given an acceleration profile and therefore will not experience accelerations dependant on any forces. Furthermore, the T1 body will not undergo any rotation and therefore does not require the moments of inertia to be defined.

Table 4.2: Masses (kg) and moments of inertia (kg m^2) for the human model's bodies

Body	Mass	$I_{X'X'}$	$I_{Y'Y'}$	$I_{Z'Z'}$	$I_{X'Z'}$
T1	–	–	–	–	–
C7	0.22	220×10^{-6}	220×10^{-6}	430×10^{-6}	0
C6	0.24	240×10^{-6}	240×10^{-6}	470×10^{-6}	0
C5	0.23	230×10^{-6}	230×10^{-6}	450×10^{-6}	0
C4	0.23	230×10^{-6}	230×10^{-6}	440×10^{-6}	0
C3	0.24	240×10^{-6}	240×10^{-6}	460×10^{-6}	0
C2	0.25	250×10^{-6}	250×10^{-6}	480×10^{-6}	0
C1	0.22	220×10^{-6}	220×10^{-6}	420×10^{-6}	0
C0	4.69	18.10×10^{-3}	23.6×10^{-3}	17.3×10^{-3}	7.1×10^{-3}

4.2 Intervertebral Discs and Ligaments

The IV discs and ligaments are both discussed in this section due to their similarity when included in the model. This is partially due to the fact that both the ligaments and the IV discs in the lower cervical spine only attach between successive vertebrae. Therefore, a clear distinction is made between the upper and lower cervical spine with respect to how the ligaments are modelled.

4.2.1 Lower Cervical Spine

Six IV spaces were identified between the vertebrae of the lower cervical spine. Each of these was given a number ranging from one (between the C7 and T1 vertebrae) to six (between the C2 and C3 vertebrae). Since the ligaments and IV discs only act on bodies adjacent to the intervertebral space, these numbers correspond to the names of the ligaments or IV discs in the model.

The combination of the IV discs and ligaments restrict the motion of vertebral bodies in all six degrees of freedom. In order to model this, a combination of forces and torques were applied to each of the vertebrae. The torque associated with an IV space was applied such that both the applied body's and reactive body's moment is experienced at their CG. A third-degree polynomial function was used to relate the torque to the angle of rotation between successive vertebrae [75]. Zhang *et al.* [75] determined these functions for each of the IV spaces based on a collection of earlier data that had been published. One of the requirements for the data was that the specimens cannot have been altered and therefore the equations account for the effects of both the IV discs and the ligaments. The torque was also given a damping component to reduce any oscillating effect at a high rate of change in angles. The damping coefficient is 1.5 N m s/rad, based on the assumptions made by De Jager [32].

The forces acting on the vertebrae were divided into two sets. The first of these are related to the IV discs. These forces act at the mid-point between the adjacent vertebral bodies. It was assumed for frontal impact that rotation of the bodies will only be about the z-axis. As such, the rotation of the IV discs about the z-axis was assumed to be the average rotation of vertebral bodies and therefore the calculations of each of the forces were taken with respect to the rotated axes of the IV disc.

The IV disc forces were modelled as linear, translational springs and dampers, but the stiffness coefficients may change depending on the direction of displacement. The stiffness coefficients related to the shear forces were defined in terms of lateral, posterior and anterior shear. These coefficients are constant for each of the IV discs [36]. In contrast, the stiffness coefficients for compression and tension in the IV discs change for each disc [76]. Table 4.3 lists the values of each of the coefficients used [36; 76]. The dampers have a coefficient of 1000 N s/m in all directions [32].

The second set of forces in the IV spaces is related to the six ligaments consist-

Table 4.3: Translational stiffness coefficients (N/m) for IV discs

Name	Compression	Tension	Anterior Shear	Posterior Shear	Lateral Shear
IV_Disc_1	973.6×10^3	82.2×10^3	62.0×10^3	50.0×10^3	73.0×10^3
IV_Disc_2	829.7×10^3	69.0×10^3	62.0×10^3	50.0×10^3	73.0×10^3
IV_Disc_3	800.2×10^3	22.0×10^3	62.0×10^3	50.0×10^3	73.0×10^3
IV_Disc_4	784.6×10^3	66.8×10^3	62.0×10^3	50.0×10^3	73.0×10^3
IV_Disc_5	765.3×10^3	69.8×10^3	62.0×10^3	50.0×10^3	73.0×10^3
IV_Disc_6	637.5×10^3	63.5×10^3	62.0×10^3	50.0×10^3	73.0×10^3

ing of the anterior longitudinal ligament (ALL), posterior longitudinal ligament (PLL), ligamentum flavum (LF), interspinous ligament (ISL), and two capsular ligaments (CLs). While it is possible to model each of the six ligaments as individual springs acting at their respective attachment points, this would also cause a moment on the vertebrae. Since the torque equations from Zhang *et al.* [75] already account for the effect of the moment, the force of the ligament was placed near the centre of rotation between vertebrae. The magnitude of the force was defined in a three-dimensional spline where the dependent parameters are the change in distance between the vertebral bodies and the difference in angle between bodies. These two parameters, along with the approximate attachment points in Figure 4.3, allow for an estimation in length of each of the ligaments. The total force is the sum of each ligament's force, determined from the splines in Figure 4.4 and is based on the estimated change in length.

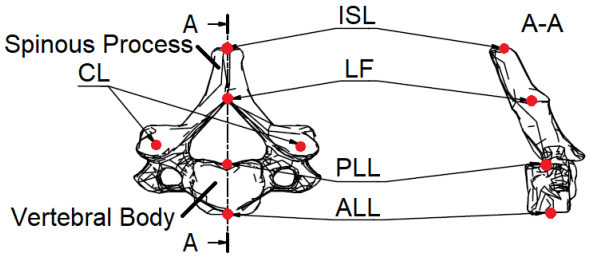

Figure 4.3: Cranial (left) and lateral (right) view of a vertebra with attachment points of lower cervical spine ligaments indicated in red

The splines in Figure 4.4 were obtained from Mattucci and Cronin [77] who conducted experiments to determine the shape of the curves. Mattucci and Cronin determined that the response to loading of the ligaments consists of three regions prior to failure. The first is a "Toe" region that follows the shape of an exponential graph, the second is a linear region and the third is a "Traumatic" region that can be approximated via a third degree polynomial function.

Mattucci and Cronin [77] also investigated the effect that the rate of deflection has on the force exerted and produced force-deflection curves for each defined

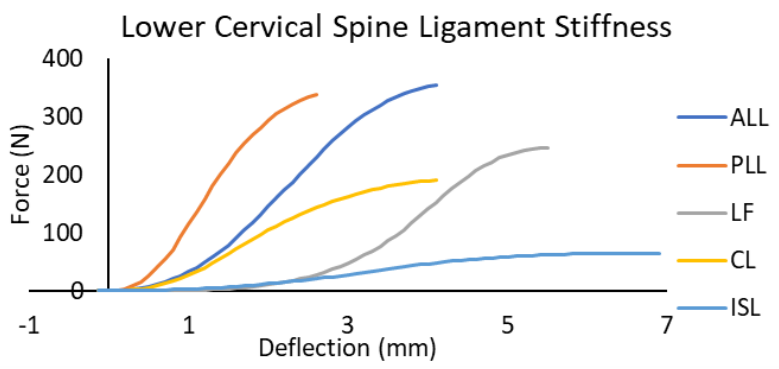

Figure 4.4: Graph of force-deflection curves for the ligaments of the lower cervical spine

rate. However, Mattucci and Cronin only conducted the study at three different strain rates, which is insufficient for extrapolating force values at in-between rates. Therefore, a damping component was included in the springs to account for the increase in force as the deflection rate increases. A value of 300 N s/m is used for the damping coefficient [32].

4.2.2 Upper Cervical Spine

The upper cervical spine differs from the lower cervical spine by not having any IV discs. This means that only ligaments attach the skull, atlas and axis to each other. Since these ligaments are critical in supporting the upper cervical spine, each individual ligament was modelled as acting at the real-life approximate attachment points.

In contrast with the lower cervical spine, some of the upper cervical spine ligaments span more than just the adjacent vertebral bodies. The apical ligament, two alar ligaments and the tectorial membrane are such examples. The apical ligament extends from the topmost point of the odontoid process to the anterior edge of the foramen magnum [34]. The alar ligaments extend laterally from the sides of the top portion of the odontoid process and attach to the side walls of the foramen magnum near the OC [34]. The tectorial membrane and the vertical component of the cruciate ligament were modelled as a single spring that attaches at the CG of the axis and extends to the anterior wall of the foramen magnum in a similar manner to the PLL of the lower cervical spine [34].

The transverse ligament allows for rotation of the atlas independent of the axis by wrapping around the odontoid process at midheight and having both ends of the ligament attached to the atlas. Since this model will only consider frontal impact, the atlas should not rotate independently to the axis and therefore it was assumed that two spring elements can attach between the odontoid process and the lateral walls of the atlas to serve the purpose of the transverse ligament [34].

The remaining upper cervical spine ligaments are the anterior membrane,

the posterior membrane and the capsular ligaments. The anterior membrane is a continuation of the ALL where the atlanto-axial component attaches at mid-height of each of the respective vertebrae and the atlanto-occiput component attaches from the midheight of the atlas to the anterior border of the foramen magnum [34]. Similarly, the posterior membrane is a continuation of the LF with the topmost attachment point at the posterior border of foramen magnum [34]. Finally, the capsular ligaments (CLs) attach between the facet joints. Following the example of Van Lopik [34], the atlanto-axial CLs were split into four spring elements located on the anterior, posterior and both lateral edges of the facet joint, relative to the centre of the facet. Similarly, the atlanto-occiput CLs were split into three spring elements with one being in the centre and the other two being on the anterior and posterior edges of the facet joint [34]. The CLs in the upper cervical spine were split into multiple components since they are much larger than that of the lower cervical spine.

The upper cervical spine ligaments have a force-deflection curve that consists of three regions. While detailed force-deflection curves exist for the lower cervical spine ligaments, the same does not appear to be true for the upper cervical spine ligaments and therefore straight line approximates were assumed for each of the regions, as shown in Figure 4.5. Table 4.4 provides the values required to generate the force-deflection curves for each of the required ligaments [76; 78]. It should be noted that the forces for the CLs needed to be divided by the number of spring elements used to represent each CL. Since these ligaments will also experience an increase in force as the rate of deformation increases, a damping component is included with a coefficient equal to 300N s/m [32].

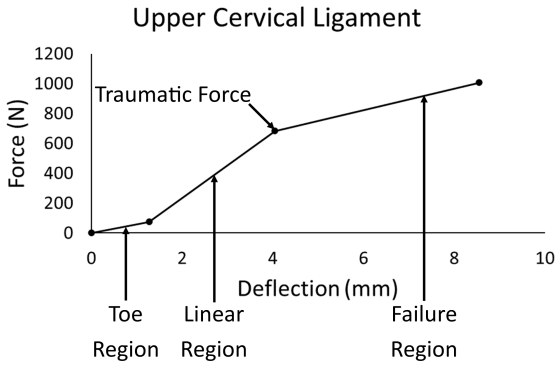

Figure 4.5: Diagram of three regions of loading experienced by the upper cervical spine ligaments

Table 4.4: List of upper cervical spine ligaments with ligament-specific values for generating the force-deflection curve

Ligament	Location	Toe Region Maximum		Linear Region		Failure Region Maximum	
		Force (N)	Elongation (m)	Stiffness (N/m)	Traumatic Force (N)	Force (N)	Elongation (m)
Apical	C2-C0	26	1.27×10^{-3}	75×10^{3}	235	346	8.55×10^{-3}
Alar	C2-C0	28	1.27×10^{-3}	83×10^{3}	257	379	8.55×10^{-3}
Tectorial Membrane	C2-C0	21	1.27×10^{-3}	61×10^{3}	191	281	8.55×10^{-3}
Transverse	C2-C1	36	2.29×10^{-3}	156×10^{3}	344	392	5.22×10^{-3}
Anterior Atlanto-axial Membrane	C2-C1	120	0.95×10^{-3}	221×10^{3}	702	1068	6.59×10^{-3}
Posterior Atlanto-axial Membrane	C2-C1	43	1.35×10^{-3}	43×10^{3}	54	97	8.15×10^{-3}
Atlanto-axial Capsular Ligament	C2-C1	37	1.17×10^{-3}	160×10^{3}	265	331	5.49×10^{-3}
Anterior Atlanto-occiput Membrae	C1-C0	105	1.56×10^{-3}	155×10^{3}	432	512	6.01×10^{-3}
Posterior Atlanto-occiput Membrae	C1-C0	36	1.21×10^{-3}	68×10^{3}	142	177	6.44×10^{-3}
Atlanto-occiput Capsular Ligament	C1-C0	64	1.8×10^{-3}	187×10^{3}	485	593	4.76×10^{-3}

4.3 Sectional Validation

The head and neck model currently consists of the vertebrae, IV discs and the ligaments. The effect of the IV discs and ligaments on the vertebrae can be tested on sections of cadavers since none of these components require a living person in the way that muscles require impulses. As such, various researchers have sectioned parts of the cervical spine and applied forces and moments to be able to record the displacement [36; 42; 43; 79]. It was important to use this data to ensure that the modelled IV discs and ligaments provide the required support prior to the addition of muscles.

4.3.1 Lower Cervical Spine

The first set of data considered was extracted from Moroney *et al.* [36]. Forces and moments were applied to sections of two consecutive vertebrae with all ligaments and the IV disc still intact. The displacement in all six degrees of freedom was measured.

Only two sections of the lower cervical spine were tested since C3-C4 and C5-C6 were considered to be representative of the lower cervical spine [39]. The testing procedure used by Moroney *et al.* involved extracting each of these sections from the rest of the cervical spine and then fixing the lower of the two vertebrae as a base. A shear force of 19.6 N, a compression force of 73.6 N or a moment of 1.8 N m was then applied to the upper vertebra at the centre of the IV disc. The displacement was measured with respect to the initial location of the upper vertebra. The same procedure was applied in software to validate the model.

Figure 4.6 indicates the measured displacements—in red crosses for the C3-C4 section and blue circles for the C5-C6 section—for each of the possible forces and moments that should be encountered in a frontal impact. The mean and standard deviation determined by Moroney *et al.* [36] from their 35 fresh cadavers is used to create the error bars shown in Figure 4.6. While most forces or moments result in almost all measurements being within a single standard deviation, this is not true when applying a 1.8 N m moment in extension. During extension, the spinous process of upper vertebra makes contact with the spinous process of the lower vertebra. To reduce pressure, the upper vertebra rotates so that the IV disc acts in torsion and this results in contact between facet joints which causes lateral bending. This process of errors leads to multiple displacements being out of the ideal range.

The second set of data used for sectional validation was from Wheeldon *et al.* [43]. While this study is limiting in comparison to Moroney *et al.* [36] in terms of only using moments in flexion and extension, it does have the advantage of considering the entire lower cervical spine. This experiment requires that the first thoracic vertebra be fixed in place while a moment is applied to the second cervical vertebra. A total of five moments were applied in both extension and flexion, while the angular displacement between each of the vertebrae was measured.

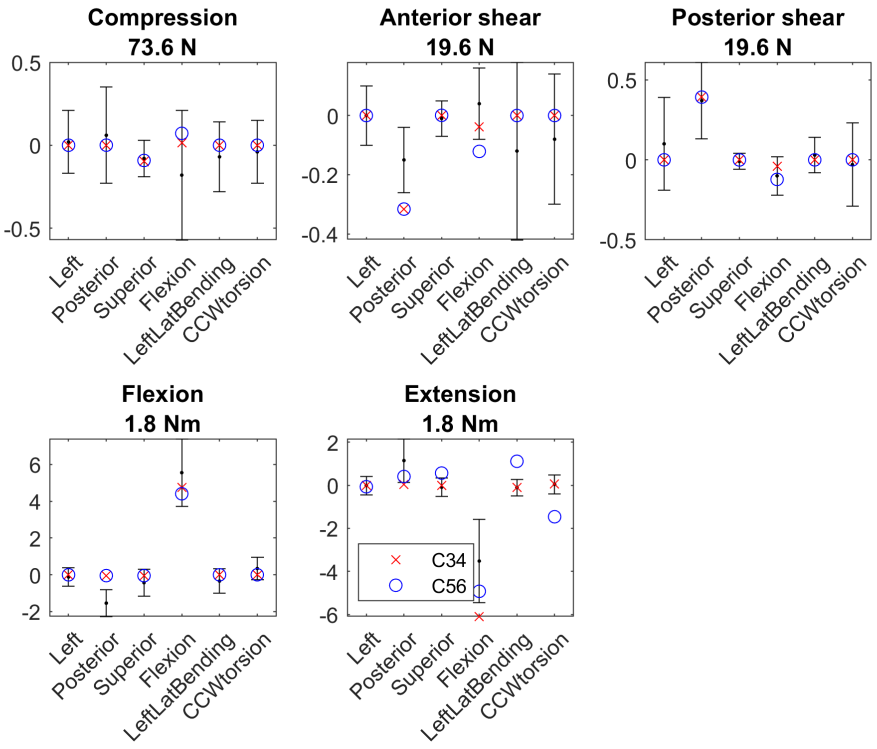

Figure 4.6: Graphs indicating the displacement of representative sections relative to error bars determined from data in Moroney *et al.* [36]

Figure 4.7 indicates the measured angular displacement against an error bar with the error being one standard deviation from the mean, as reported by Wheeldon *et al.* [43]. From each of these plots, it is clear that the lower cervical spine is nearly too stiff in flexion while being too flexible in extension. To achieve these responses, many of the moment-rotation functions are scaled to best match the data provided by Wheeldon *et al.* [43].

Figure 4.8 shows the total displacement experienced in the lower cervical spine. This graph once again indicates that the spine is slightly stiffer in flexion than it should be, but making it any more flexible will result in the response exiting the indicated error regions in extension.

4.3.2 Upper Cervical Spine

The requirements for validating the upper cervical spine under static loading conditions were extracted from Panjabi *et al.* [79]. Panjabi *et al.* conducted their experiments by fixing the C3 vertebra to the test apparatus and applying a moment to the occiput. The relative angular displacements between C0 and C1 and C1 and C2 were measured. The article recorded these results as a mean with a standard deviation.

In validating the model's upper cervical spine, moments were only applied in

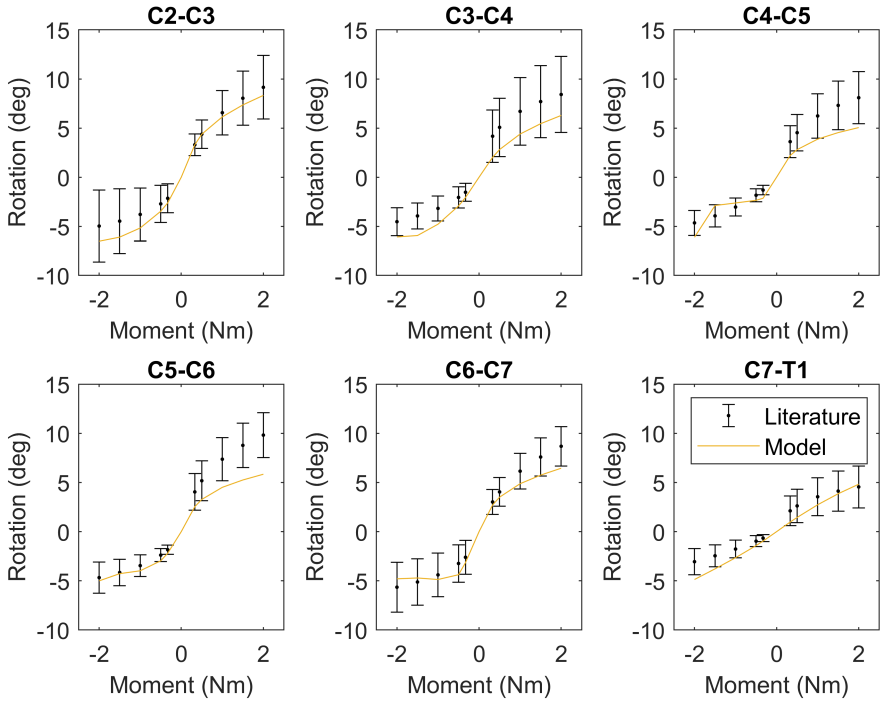

Figure 4.7: Graphs indicating the model's angular displacement at each joint of the lower cervical spine compared to data from Wheeldon *et al.* [43]

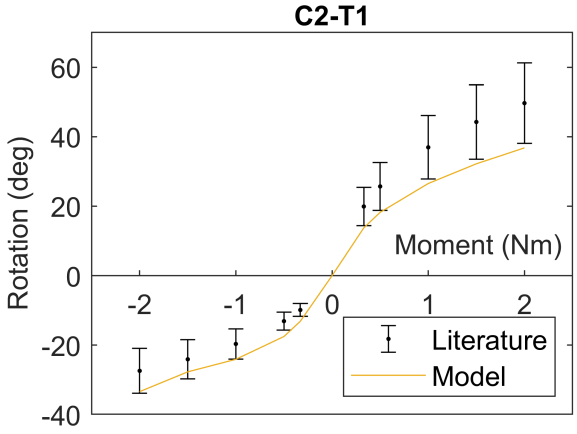

Figure 4.8: Graph indicating the model's total angular displacement of the lower cervical spine in comparison to data from Wheeldon *et al.* [43]

flexion and extension and the angular displacement was measured in the same plane. Figure 4.9 shows the results obtained during testing of the model while indicating a region of one standard deviation from the mean, based on the data from Panjabi *et al.* [79].

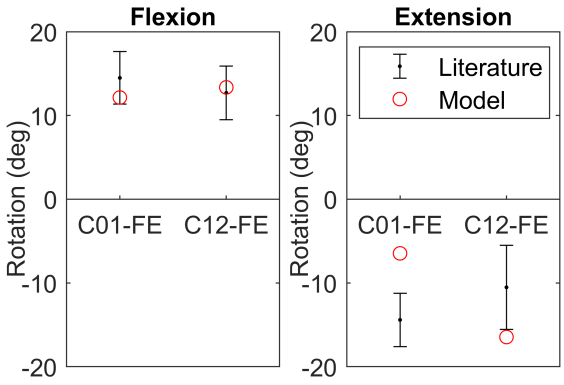

Figure 4.9: Graph indicating the model's angular displacement of the upper cervical spine in flexion and extension against error bars based on data from Panjabi *et al.* [79]

While Figure 4.9 indicates that the upper cervical spine is within range for flexion, this was not the original case. Initially, the C01 joint was too stiff. Since the upper cervical spine is dependent on ligaments for its response, the force-deflection curve of the posterior atlanto-occiput membrane is scaled to 60 % of its original force for the same displacement. In a similar manner the anterior atlanto-occiput membrane is scaled to 25 % and the anterior atlanto-axial membrane is scaled to 110 % of their original forces to try and improve the response in extension. While scaling these ligaments does not ensure that the upper cervical spine is within the specified response regions for extension, it does bring it much closer to this response region requirements.

It is expected that the dominant angular displacement during a frontal collision will be in flexion and therefore it is more important for the validation data to be within the requirements in flexion than in extension. It is therefore believed that the model's upper cervical spine sufficiently represents that of an actual upper cervical spine.

The upper cervical spine was also subjected to a range of motion test for flexion and extension based on the data from White and Panjabi [42]. Similar to the other upper cervical spine validation test, a moment was applied to the occiput while the C2 vertebra is fixed in place. The applied moment was gradually increased to a maximum of 20 N m and the angular displacement was measured between appropriate vertebrae.

Figure 4.10 shows the recorded angular displacement as the moment was increased. The boundaries set by White and Panjabi [42] are also indicated on the graphs. Both graphs show that, especially in flexion, the upper cervical spine

joints exceed the set boundaries. Oscillations, which are unexpected, are shown on both graphs and could be explained by thinking of the springs between successive vertebrae as not having sufficient damping. This means that the rotation between the vertebrae overshoots the steady-state rotation associated with a specific applied moment, before rebounding and oscillating until it reaches a steady state.

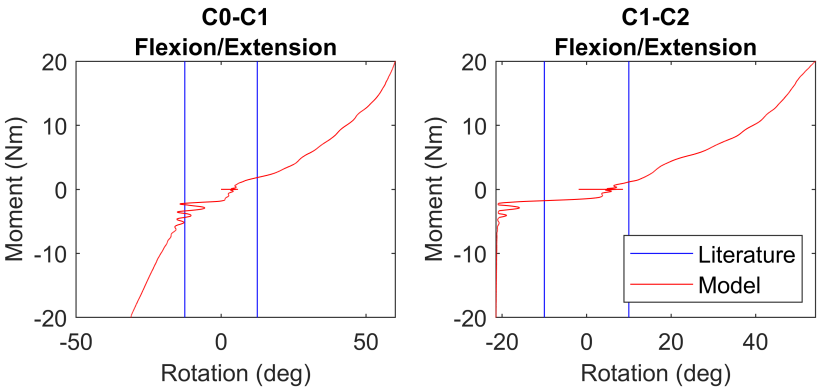

Figure 4.10: Graph displaying the relative angular displacement of upper cervical spine vertebrae as the applied moment is increased, with boundaries set from White and Panjabi [42] indicated in blue (flexion is positive)

4.4 Muscles

The addition of muscles to the model can be divided into two components. The first component consists of where the muscles affect the model and is therefore the component executed in MSC Adams. As such, this component includes the location of each of the muscles and the direction in which each of the muscles will act. The second component determines the force with which the muscles act. This component extracts data from the MSC Adams model to determine the magnitude of the muscles' forces based on a Simulink muscle model from literature [41].

4.4.1 Types of Muscles

A total of 19 muscles were included in this model. This is fewer than that which was mentioned in Section 2.1.5, but the nine muscles that were not included are believed to have little effect on the model during frontal impact.

The eight muscles associated with the infrahyoid and suprahyoid groups were excluded since their main purpose is to shift the hyoid bone during swallowing. They may also move the mandible while chewing and speaking, but since the mandible was fixed for the purpose of this model, it is believed that these muscles will not have a significant effect on the flexion of the head [21]. The final muscle

that was excluded is the iliocostalis cervicis. While this muscle does extend into the lower neck region, the focus of this muscle is more often associated with the lower back [24]. Furthermore, the iliocostalis muscle is located laterally to the spine and therefore is believed to have less of an effect in a model that focuses on frontal collision.

The muscles that were included in the model are the sternocleidomastoid and the three scalene muscles from the anterior of the neck, the longus capitis and longus colli muscles from the lateral portion of the neck and the 13 posterior muscles. These 13 muscles are the levator scapulae, longissimus capitis, longissimus cervicis, multifidus, semispinalis capitis, semispinalis cervicis, splenius capitis, splenius cervicis, trapezius and the four suboccipital muscles.

This model consists of 19 individual muscles, but due to the fact that most muscles' attachment points are across multiple vertebrae, many of the muscles were sectioned into various segments [33; 34]. This resulted in 69 segments which attach between only two solid bodies in the model and each of these segments can be treated as individual muscles due to the direct proportionality between pCSA and maximum muscle force.

4.4.2 Location of Muscles

Each muscle segment requires an origin and an insertion point at which the muscle force would act. Table 4.5 contains the full list of segments with the bodies that the forces act on and the points at which the forces were applied on the bodies. These points were based on anatomical markers on the bodies and have therefore been included in the table as abbreviations with the full description given in Table 4.6 due to the length of the descriptions.

Some of the segments attach to vertebrae that are not included in this model. These are typically muscle segments that have their origin in the thoracic spine. To account for this, the origin was fixed to the T1 vertebra, but the point is still located at the anatomical marker of the actual vertebra.

The length of muscle segments vary, but the longest may stretch from the skull to the thoracic spine. The problem with such long segments is that if the neck is in flexion, then a straight line between the origin and insertion point would intersect with the solid bodies. This is not possible and an actual muscle would follow the curve of the neck. Following the example of van Lopik and Acar [39], intermediate points were added along the muscle path. These points were attached to vertebrae located between the origin and insertion body via fixed constraints such that the points will move and rotate with the vertebral bodies. The intermediate points do not interact with each other and only provide an approximation of the curved muscle length based on the curvature of the neck as a result of translating and rotating vertebrae. The total muscle length was calculated as the sum of the lengths between consecutive intermediate points of the same muscle segment. The number of intermediate points depended on the length of the segment and how many solid bodies were located between the ori-

gin and insertion points. Also, muscles that were closer to the spinal column have more intermediate points since they will experience more bending than those muscles that are further from the spine. The total number of intermediate points for each muscle segment is recorded in Table 4.5.

The force calculated for each muscle segment is only a magnitude and a direction still needs to be determined. Since the muscle has intermediate points to represent curvature and the muscle can only contract, the force was directed from either the origin or the insertion point to its nearest intermediate point. In the MSC Adams model, a three-dimensional force was placed on both ends of the muscle and the proportion of the force's magnitude in each of the three axes was determined from the relative position of the closest intermediate point.

4.4.3 Force Exerted by Muscles

The force exerted by each of the muscle segments was determined by the Simulink model developed by Haeufle *et al.* [41]. A short overview of this model is provided in Section 2.2.4. This muscle model consists of the contractile element (CE) with the parallel elastic element (PEE) to represent the muscle fibres. In series with these components is a parallel combination of the serial elastic element (SEE) and the serial damping element (SDE) which represents the tendon of a muscle. These four components are all shown in Figure 2.7.

The force exerted by the CE is dependent on the current length of the CE, the current velocity of the CE and the activation level given to the muscle. The effect of the length on the force can be visualised as a bell curve with non-symmetric sides. The peak of the curve is located at the initial CE length. This indicates that the force exerted by the muscle decreases as the muscle changes length. The effect of the velocity on the CE is summed up as two hyperbolae graphs with force on the y-axis and velocity on the x-axis. The first hyperbola defines the force for a shortening CE with a horizontal asymptote below zero such that the force reaches zero for high speed shortenings. The second hyperbola defines the force for a lengthening CE such that the horizontal asymptote is located above the maximum force and therefore the force produced for a lengthening CE may exceed the maximum force of the muscle. The vertical asymptotes are placed such that both hyperbolae have the same force value at zero velocity. The shape of the hyperbolae are dependent on the current length of the muscle and its activation level [41].

The PEE spring has an exponential force-to-length relationship. Since this spring is in parallel with the CE, the dependent length is the same length as the CE. Since the muscle is never completely at rest, the zero length of the PEE was set to 90 % of the initial length of the CE [41]. This simulates some force even when the muscle is at its full length and is not activated. For lengths shorter than the zero length, the force produced by the PEE is equal to zero.

The SEE is also a non-linear spring. The difference between the SEE and the PEE is that the SEE becomes linear after a certain length, but starts with a non-

Table 4.5: Complete list of all the muscle segments with their attachment locations in the model. The abbreviations are explained in Table 4.6.

Name	**Segment No.**	**Origin Body**	**Origin Point**	**Insertion Body**	**Insertion Point**	**No. of Intermediate Points**
Levator Scapulae	1	C1	TP	T1	MBS	0
	2	C2	TP	T1	MBS	0
	3	C3	TP	T1	MBS	0
	4	C4	TP	T1	MBS	0
Longissimus Capitis	1	C4	TP	C0	MP	0
	2	C5	TP	C0	MP	0
	3	C6	TP	C0	MP	1
	4	C7	TP	C0	MP	1
	6	T1	TP of T2	C0	MP	2
Longissimus Cervicis	1	T1	TP of T2	C2	TP	1
	2	T1	TP of T2	C3	TP	1
	3	T1	TP of T2	C4	TP	1
	4	T1	TP of T2	C5	TP	1
	5	T1	TP of T2	C6	TP	0
Longus Capitis	1	C3	ATTP	C0	BOB	1
	2	C4	ATTP	C0	BOB	1
	3	C5	ATTP	C0	BOB	2
	4	C6	ATTP	C0	BOB	2
Longus Colli	3	C5	ATTP	C1	ATVB	1
	5	T1	ASB	C2	ASB	2
	6	T1	ASB	C3	ASB	1
	7	T1	ASB	C4	ASB	1
	8	T1	ASB	C5	ATTP	1
Multifidus	1	T1	TP of T4	C7	SP	0
	2	T1	TP of T3	C7	SP	0
	3	T1	TP of T3	C6	SP	1
	4	T1	TP of T2	C6	SP	1
	5	T1	TP of T2	C5	SP	1
	6	T1	TP	C5	SP	1
	7	T1	TP	C4	SP	1
	8	C7	SAP	C4	SP	1
	9	C7	SAP	C3	SP	1
	10	C6	SAP	C3	SP	1
	11	C6	SAP	C2	SP	1
	12	C5	SAP	C2	SP	1
Obliquus Capitis Inferior	1	C2	SP	C1	TP	0

Obliquus Capitis Superior	1	C1	TP	C0	BNL	0
Rectus Capitis Posterior Major	1	C2	SP	C0	LINL	0
Rectus Capitis Posterior Minor	1	C1	PT	C0	MINL	0
Scalenus Anterior	2	C4	ATTP	T1	STFR	2
Scalenus Medius	3	C3	PTTP	T1	SBFR	2
Scalenus Posterior	2	C5	PTTP	T1	ESSR	1
Semispinalis Capitis	1	C4	AP	C0	BNL	1
	2	C5	AP	C0	BNL	1
	3	C6	AP	C0	BNL	1
	4	C7	AP	C0	BNL	2
	7	T1	TP of T3	C0	BNL	4
Semispinalis Cervicis	1	T1	TP	C2	SP	2
	2	T1	TP of T2	C3	SP	2
	3	T1	TP of T3	C4	SP	2
	4	T1	TP of T4	C5	SP	1
	5	T1	TP of T5	C6	SP	1
	6	T1	TP of T6	C7	SP	0
Splenius Capitis	1	C7	SP	C0	MP	2
	3	T1	SP of T2	C0	MP	3
Splenius Cervicis	1	T1	SP of T3	C1	TP	3
	2	T1	SP of T3	C2	TP	2
	3	T1	SP of T3	C3	TP	2
Sternocleido-mastoid	1	T1	ASMS	C0	LSMP	4
	3	T1	SSC	C0	LSMP	4
	4	T1	SSC	C0	LSNL	4
Trapezius	1	T1	Acr	C7	SP	0
	2	T1	SCC	C6	SP	0
	3	T1	SCC	C5	SP	0
	4	T1	SCC	C4	SP	1
	5	T1	LTC	C3	SP	1
	6	T1	LTC	C2	SP	1
	7	T1	LTC	C1	SP	2
	9	T1	LTC	C0	NL	2

linear toe region. The parameters defining the spring's response allow for the changing of the length of the toe region, as well as the ability to set the gradient of the linear region [41]. A further difference between the SEE and the PEE is

Table 4.6: Abbreviations associated with Table 4.5

Short Name	Full Name
Acr	Acromion of scapula
AP	Articular process
ASB	Anterior surface of bodies
ASMS	Superior part of anterior surface of manubrium sterni
ATTP	Anterior tubercle of transverse process
ATVB	Anterior tubercle of vertebral body
BNL	Between superior and inferior nuchal lines
BOB	Basilar part of occipital bone
ESSR	External surface of 2nd rib
LINL	Lateral of inferior nuchal line
LSMP	Lateral surface of mastoid process of the temporal bone
LSNL	Lateral half of superior nuchal line of the occipital bone
LTC	Lateral third of clavical
MBS	Medial border of scapula
MINL	Medial part of inferior nuchal line
MP	Mastoid process
NL	Nuchal line of occipital bone
PT	Posterior tubercle
PTTP	Posterior tubercle of transverse process
SAP	Superior Articular process
SBFR	Superior border of first rib
SCC	Superior crest of scapula
SP	Spinous process
SSC	Superior surface of medial third of the clavicle
STFR	Scalene tubercle on the inner border of the first rib
TP	Transverse process

that the SEE's dependent length is the difference between the current length of the muscle and the current length of the CE. This can also be called the tendon length.

The final component is the SDE. This damper is located in parallel with the SEE and is dependent on the velocity of the tendon length and the total force produced by the muscle. To simplify the explanation of the dependencies, the force is equal to the product of a damping coefficient and the velocity of the tendon length. The damping coefficient has a linear relationship to the total muscle force and passes through zero [41].

To complete the muscle model it is necessary to know the length of the CE at all times, but this length cannot be measured from the model. Therefore, the muscle model calculates the acceleration of the CE based on the forces acting on the CE. Integrating the acceleration yields the new CE length.

All these muscle model components were combined into a single Simulink

block that takes the muscle length, muscle velocity and activation level as inputs and outputs the total muscle force. This is the "MuscleTendonUnit" shown in Figure 4.11. The rest of the figure shows the interface to MSC Adams, where the first input is the magnitude of the length of the muscle and the second input is the magnitude of the velocity. The direction of the velocity was determined based on the change in length and this direction is added to the measured velocity. Finally, a unit conversion is done to convert the millimetres measured in MSC Adams to the metres used in the muscle model.

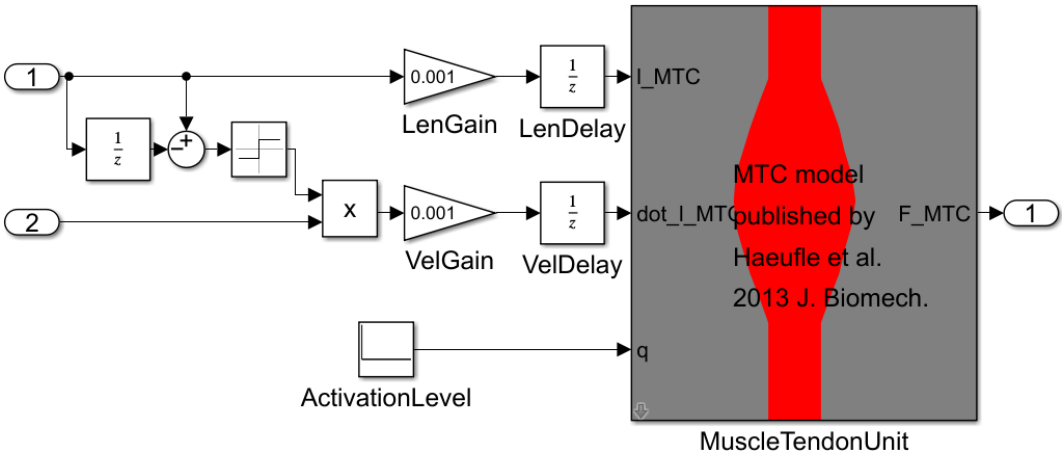

Figure 4.11: Image of an individual muscle segment in Simulink

Each muscle segment required initialisation parameters. Four such parameters are specific to each muscle segment while all other parameters are either constant for all muscles, or are derived from the dependent parameters [41]. The muscle-dependent parameters are listed in Table 4.7. The maximum force for the whole muscle or a section thereof was obtained from Vasavada *et al.* [80]. This maximum force was proportionally divided between each of the segments, based on their pCSAs. The CE lengths listed in the Table 4.7 were obtained directly from Van Lopik [34] since the two models used the exact same muscle segments. Finally, the muscle length was measured from the model and the tendon length is the difference between the muscle length and the CE length.

4.5 Full Validation

The complete head and neck model, consisting of vertebrae, ligaments, IV discs and muscles, required validation. This validation differs from the sectional validation in Section 4.3 by considering the model as a whole. Also, this validation considered the response of the model during a frontal collision, whereas the sectional validation applied static forces while measuring the response.

Full validation aims to have the reaction of the model match the results reported by Thunnissen *et al.* [46]. Thunnissen *et al.* obtained these results from

Table 4.7: Properties of each of the muscle segments required to run the muscle model

Name	Segment No.	Maximum Force (N)	Contractile Element (CE) Length(mm)	Muscle Length (mm)	Tendon Length (mm)
Levator Scapulae	1	19	10.3	15.5	5.2
	2	19	10.3	13.0	2.7
	3	19	10.3	12.9	2.6
	4	19	10.3	11.8	1.5
Longissimus Capitis	1	6.2	6	7.8	1.8
	2	6.2	6	9.2	3.2
	3	6.2	6	10.5	4.5
	4	6.2	6	11.4	5.4
	6	6.2	6	14.1	8.1
Longissimus Cervicis	1	4	4.4	9.6	5.2
	2	4	4.4	8.4	4.0
	3	4	4.4	7.2	2.8
	4	4	4.4	5.9	1.5
	5	4	4.4	4.6	0.2
Longus Capitis	1	8.25	1.5	6.3	4.8
	2	8.25	3.4	8.1	4.7
	3	8.25	4.8	9.5	4.7
	4	8.25	5.6	11.1	5.5
Longus Colli	3	10	3.6	7.2	3.6
	5	3.33	6.5	10.2	3.7
	6	3.33	6.5	8.7	2.2
	7	3.33	6.5	7.1	0.6
	8	10	3.6	5.6	2.0
Multifidus	1	40.3	4.2	7.3	3.1
	2	34.1	4.2	5.4	1.2
	3	12.4	4.2	6.5	2.3
	4	12.4	4.2	5.3	1.1
	5	6.2	4.2	5.7	1.5
	6	6.2	4.2	5.2	1.0
	7	4.65	4.2	5.7	1.5
	8	4.65	4.2	4.3	0.1
	9	4.65	4.2	5.3	1.1
	10	4.65	4.2	4.8	0.6
	11	4.65	4.2	5.8	1.6
	12	4.65	4.2	5.0	0.8
Obliquus Capitis Inferior	1	45	3.8	6.1	2.3

Obliquus Capitis Superior	1	37	2.5	4.7	2.2
Rectus Capitis Posterior Major	1	33	3.7	5.6	1.9
Rectus Capitis Posterior Minor	1	18	1.9	2.5	0.6
Scalenus Anterior	2	51	4.2	10.3	6.1
Scalenus Medius	3	72	5	11.4	6.4
Scalenus Posterior	2	55	6.2	15.1	8.9
Semispinalis Capitis	1	16	6.8	8.0	1.2
	2	16	6.8	9.2	2.4
	3	16	6.8	10.2	3.4
	4	16	6.8	11.5	4.7
	7	64	6.8	15.7	8.9
Semispinalis Cervicis	1	2.27	6.8	7.9	1.1
	2	4.53	6.8	7.6	0.8
	3	6.63	6.8	8.5	1.7
	4	13.95	6.8	9.6	2.8
	5	17.44	6.8	11.0	4.2
	6	19.18	6.8	12.2	5.4
Splenius Capitis	1	50	8.6	14.0	5.4
	3	50	8.6	17.9	9.3
Splenius Cervicis	1	16.67	9.3	18.1	8.8
	2	16.67	9.3	16.1	6.8
	3	16.67	9.3	15.1	5.8
Sternocleido-mastoid	1	69	12.2	19.7	7.5
	3	34	12	16.6	4.6
	4	34	11	19.5	8.5
Trapezius	1	377	8.4	15.5	7.1
	2	18.2	8.4	14.7	6.3
	3	18.2	8.4	15.0	6.6
	4	18.2	8.4	15.5	7.1
	5	5.44	11	13.6	2.6
	6	5.44	11	14.5	3.5
	7	5.44	11	16.5	5.5
	9	7.09	11	19.8	8.8

sled tests conducted with living, human volunteers and therefore is appropriate for validating the model with active muscles. A description of the various results reported by Thunnissen *et al.* is provided in Section 2.2.5. The acceleration profile used as input to the model is the mean linear acceleration of the first thoracic vertebra reported by Thunnissen *et al.*. This acceleration profile is shown in Figure 4.12.

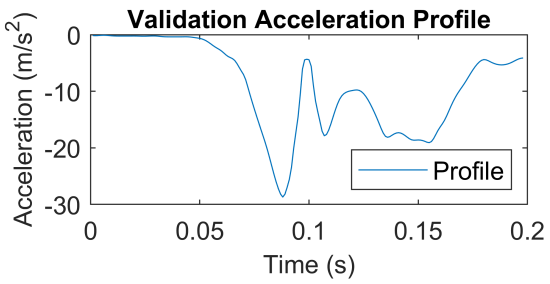

Figure 4.12: Acceleration profile applied at the first thoracic vertebra for validation [46]

The model was assumed to be sufficiently validated during the sectional validation prior to the addition of muscles and therefore the only parameters that needed to be changed in the full validation were those related to the muscles. Unfortunately, this does include a tuning element within the validation procedure, but due to no other target data being available, it was accepted as being an unavoidable necessity. The muscle model only considers three input parameters during a simulation—these are the muscle length, muscle velocity and activation level. The length and velocity are parameters that depend on the muscle in the model, but the activation level should be dependent on the impulse received from the brain via neuromuscular transmission (NMT). Since the model does not include NMT, the activation level was user-defined. The activation level needed to be altered such that the model's response would fall within the corridors provided by Thunnissen *et al.* [46].

Thunnissen *et al.* [46] defined a neck link angle and a head link angle. These are the angles made by the lines joining the base's CG to the OC and the OC to the head's CG, respectively. It is expected that the head link angle will be dependent on only the muscles that connect to the head and therefore a distinction in activation levels of the muscles was made based on where they connect. Therefore, two activation level profiles were defined, where the first profile is for all muscles that have a connection point on the head and the second profile is for all muscles that only have connection points on the neck.

The activation levels were defined by a series of points joined by straight-line interpolation. These points were limited to having a range of 0.01 to 1 and the activation level must be defined for the entire period from 0 to 0.2 s. An iterative approach was taken to altering these points in order to improve the response of the model. This approach involved isolating a point in the activation level profile and providing this point with a set of potential coordinates within the specified limits. The coordinates associated with the best results based on the validation corridors were set in place and another point was altered. This process repeated until no further improvement occurred. Figure 4.13 shows the resultant activation levels of the iterative approach.

The activation levels could also be determined using an optimisation algorithm. Appendix D discusses the process of optimising the response of the model

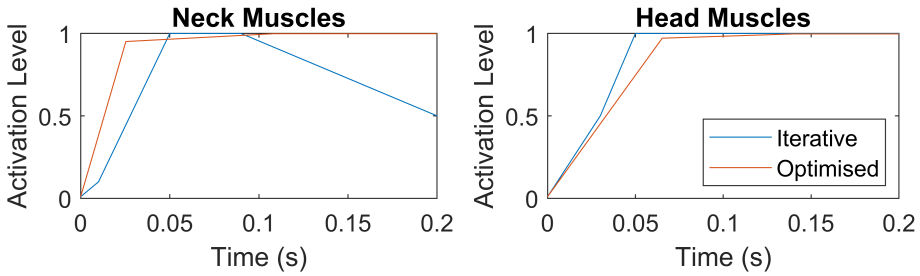

Figure 4.13: Activation levels of the muscles during simulation

for each of the validation curves. The optimisation process made use of the Bayesian optimisation algorithm and was limited to 30 iterations. The optimisable parameters were the coordinates of the points of the activation levels. An assumption was made that the head and neck angles, as well as the OC compression force and moment, are more important for the final model since these are directly linked with the optimisation of the tether. This assumption was justified by considering that these four measurements would be able to predict the values of all the other measurements since they are dependent on each other. An error value based on the root mean square (RMS) of these four validation curves was used as the objective function that needed to be minimised. The optimised activation level curves, also shown in Figure 4.13, yielded better results than the iteratively determined activation level curves and therefore the head and neck model uses the former. A further advantage of using the optimisation approach to determine the activation levels is that, should a different validation procedure be required, the objective functions could easily be adjusted to reflect the new validation requirements and the optimisation procedure could be executed in the exact same manner. This would make finding the activation levels associated with new validation data less arduous.

The validation graphs associated with the optimised activation levels in Figure 4.13 are shown in Figure 4.14 and Figure 4.15. Each of the results obtained from the model are plotted against the corridors specified by Thunnissen *et al.* [46].

Figure 4.14 includes the head link angle and the neck link angle. The maximum of the head link angle overshoots the maximum of the validation corridor, while the maximum of the neck link angle undershoots the maximum of the validation corridor. This implies that the motion-controlling components keeping the head attached to the neck are not stiff enough, while the springs and forces that control the motion of the neck vertebrae are slightly too stiff.

The stiffer neck is also visible in the OC location plot in Figure 4.15 where the OC extends far enough in the x-direction, but does not use the full range of the corridor in the y-direction. The OC location is also affected by the neck link length in Figure 4.15 which does not shorten as the validation corridor shows after 100 ms, but this does not affect the maximum y-deflection of the OC.

The head CG location is a combination of the head link angle, the neck link

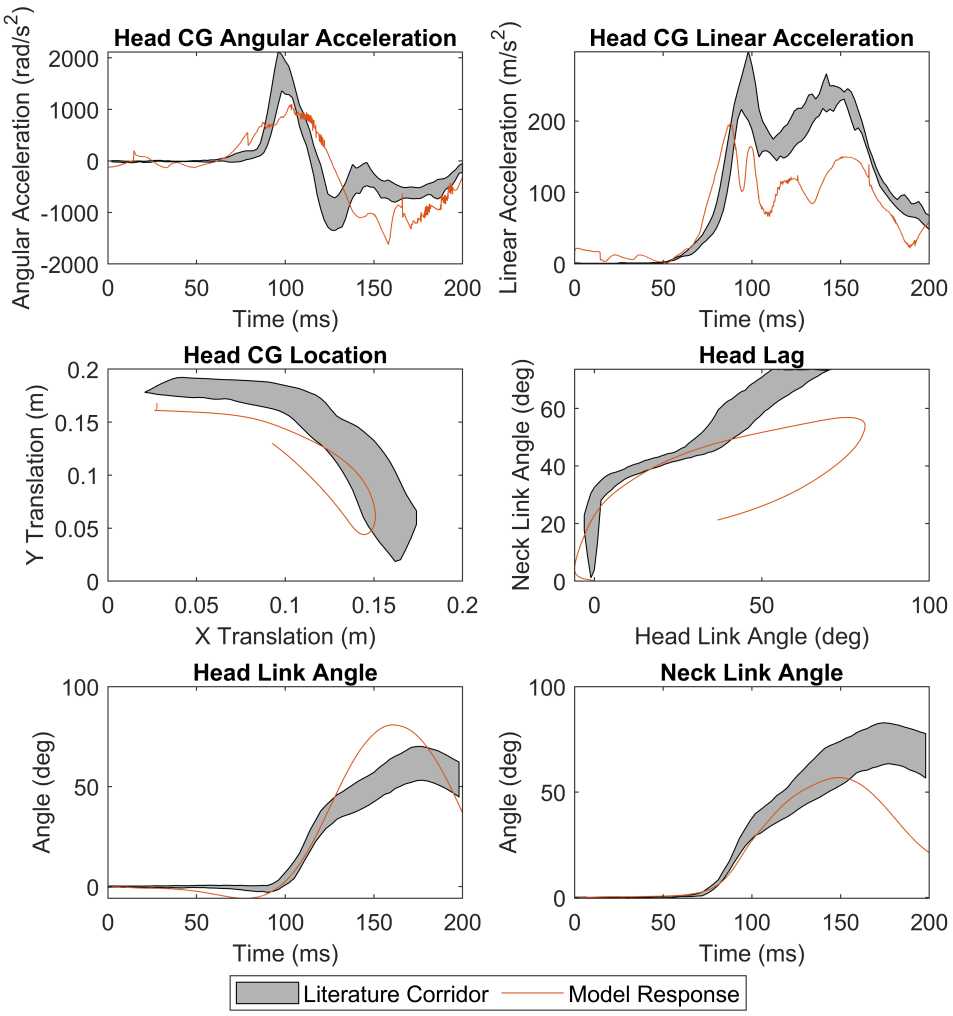

Figure 4.14: Validation graphs of acceleration, head and neck angles and head CG location for the human head and neck model with the corridors obtained from Thunnissen *et al.* [46]

angle and the neck link length. In this graph in Figure 4.14, the starting point is slightly lower due to the parameters of the model and therefore is often outside the corridor. Adjusting the starting point to be the same as the starting point of the corridor would suggest that the model follows the corridor. This implies that the overshoot of the head link angle and the undershoot of the neck link angle cancel each other out in terms of the head CG location.

Figure 4.14 contains the two validation graphs related to acceleration. Both of these graphs show that the model's response follows a similar shape to the corridors of Thunnissen *et al.* [46], but with slight problems. The head's CG angular acceleration lags slightly behind the given corridor. The head's CG linear acceleration appears as if it has been linearly scaled from the validation corridor and thus does not reach the same magnitudes that the corridor requires.

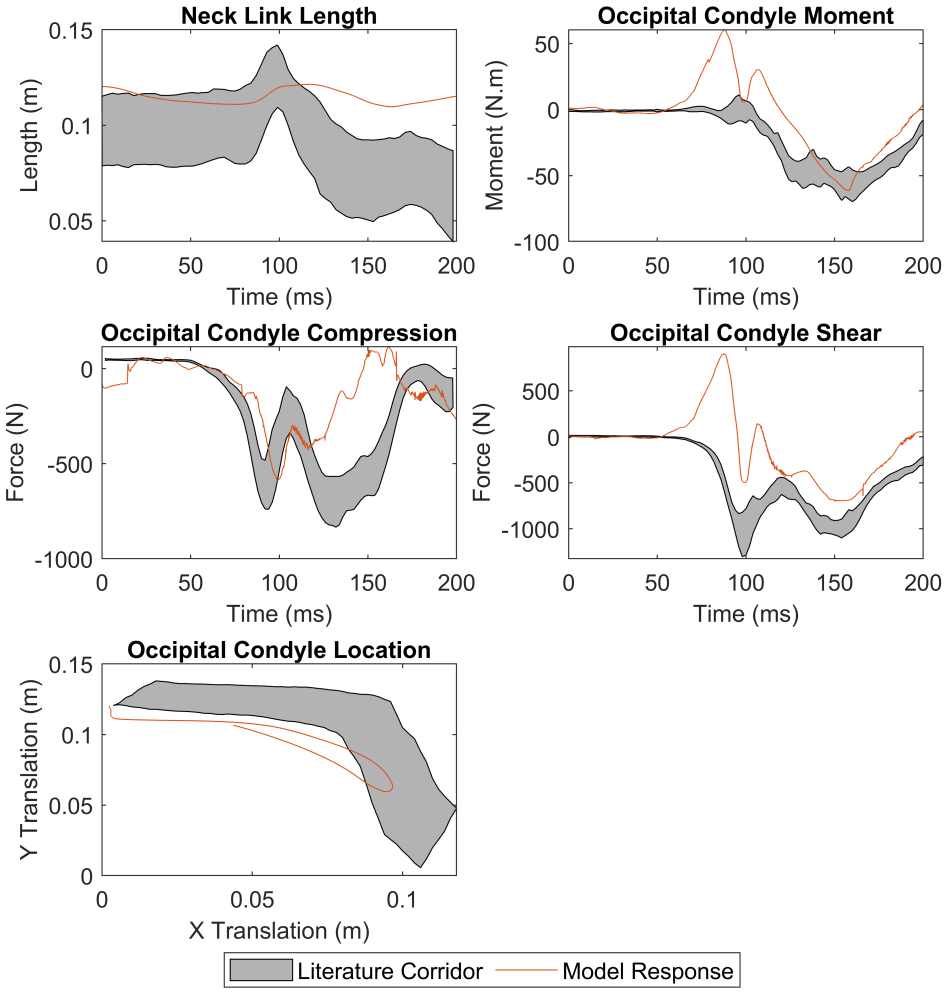

Figure 4.15: Validation graphs of neck link length, forces and moments at the OC and OC location for the human head and neck model with the corridors obtained from Thunnissen *et al.* [46]

The final aspects to consider from the validation curves are the forces and moment about the OC, shown in Figure 4.15. Both the OC moment and shear exhibit a significant spike prior to 100 ms that should not occur according to the validation corridor. Fortunately, both recovered such that they followed the general shape of the validation corridor, even if they were not within the corridor. Also, the maximum magnitude of the moment is within the validation corridor and this is advantageous for calculating the NIC. The OC compression contradicts the moment and shear by initially following the corridor up to about 120 ms and then deviating from the validation curve. Even though the compression curve exits the specified validation corridor, the OC remains in tension for the majority of the response, as is expected.

The most concerning aspect of the validation procedure is that neither the

OC compression, nor the OC moment follow the validation corridors accurately, since the NIC will be calculated based on these values. Further improvement of the model's response by editing the activation levels of the muscles is not believed to be possible since the optimisation process should have selected the best parameters. Therefore, serious alterations would need to be made to improve the model. The first option would be to provide each muscle with its own activation level, but this would require significantly more computing power to determine the optimal activation levels since the number of optimisable parameters would increase by a minimum factor of 10. The second option would be to change the values of the muscle models' fixed parameters which were initially obtained from literature. Due to the number of fixed parameters, it may be necessary to obtain potential parameter values from other, previously unknown literature sources instead of blindly changing parameter values. Finally, if none of these options yield better results, it would be necessary to review the parameters used to model the ligaments and IV discs and potentially find newer literature sources with improved mechanical properties for human tissues.

In conclusion, the model has potential for further improvement, but none of it is possible without significant alterations that may be difficult to implement. Therefore, the model was accepted as validated based on the fact that the maximum predicted magnitudes of the OC moment and compression force are within the range of maximum magnitudes indicated in the literature. This still raises concerns for calculating the NIC, since the NIC does not only rely on the maximums of the OC compression force and moment. To compensate for this, the optimisation process will not only consider minimising the maximum NIC, but will also attempt to minimise the maximum moment and the maximum axial force in separate cases.

Chapter 5

Model Comparison

Two models of the head and neck were developed and validated. The responses of these models should be compared to each other since they should provide similar results. The comparison is divided into two sections based on the acceleration profiles applied to the models.

5.1 Validation Acceleration Profile

The first comparison applied the acceleration profile shown in Figure 4.12 to both the human and the ATD models. This comparison was further extended to include models with and without helmets. In order to include the helmet on the respective models, both the mass and the moments of inertia were required.

The maximum helmet mass is defined as 1.8 kg [4]. The helmet was assumed to be the maximum mass, since it should have the greatest effect on the model. The moment of inertia was calculated by modelling the helmet as a hollow sphere. Formula 5.1 calculates the moment of inertia about all three axes where m_{helmet} is the mass of the helmet, t_{helmet} is the thickness of the helmet and r_{head} is the radius of the head.

$$MOI = \frac{2 \times m_{helmet}}{5} \left(\frac{(r_{head} + t_{helmet})^5 - r_{head}^5}{(r_{head} + t_{helmet})^3 - r_{head}^3} \right) \tag{5.1}$$

The head radius was determined from Standard FIA 8860-2018 [4] where a maximum and minimum head circumference is given as 0.61 m and 0.5 m, respectively. The helmet thickness was assumed to be 0.05 m. Both the moments of inertia for the minimum and maximum head circumferences were calculated and the average, 16.7×10^{-3} kg m^2, was used as the helmet's moment of inertia.

Njus *et al.* [81] calculated the moments of inertia of army helmets, American football helmets and bicycle helmets to determine a linear line of best fit for each of the axes. Extrapolating from these lines to 1.8 kg, Njus *et al.* predicts moments of inertia of 14.5×10^{-3} kg m^2 about the x-axis, 16.7×10^{-3} kg m^2 about the y-axis and 18.5×10^{-3} kg m^2 about the z-axis. Unfortunately, Njus *et al.* did not calculate the moments of inertia for racing helmets, but these values indicate that a moment of inertia of 16.7×10^{-3} kg m^2 for the helmet in the model is reasonable.

The parallel axis theorem could be used to join the head and the helmet's moments of inertia. However, the helmet's CG was assumed to be close to the head's

CG because of the manner in which the helmet encloses the head. Therefore, the mass and moments of inertia of the helmet were added to the mass and moments of inertia of the head without using the parallel axis theorem.

Figure 5.1 shows the responses of both models, with and without helmets, superimposed on the validation corridors associated with the acceleration profile [46]. These responses are limited to the head's CG and OC trajectories and the OC moment and axial force. The validation corridors should only be compared to the ATD without a helmet response since Thunnissen *et al.* did not measure responses with helmets attached and a detailed discussion has already been done for the human model. All the trajectories, as well as the validation corridors, are aligned such that they start from the point $(0,0)$, since this makes it easier to compare the trajectories to each other.

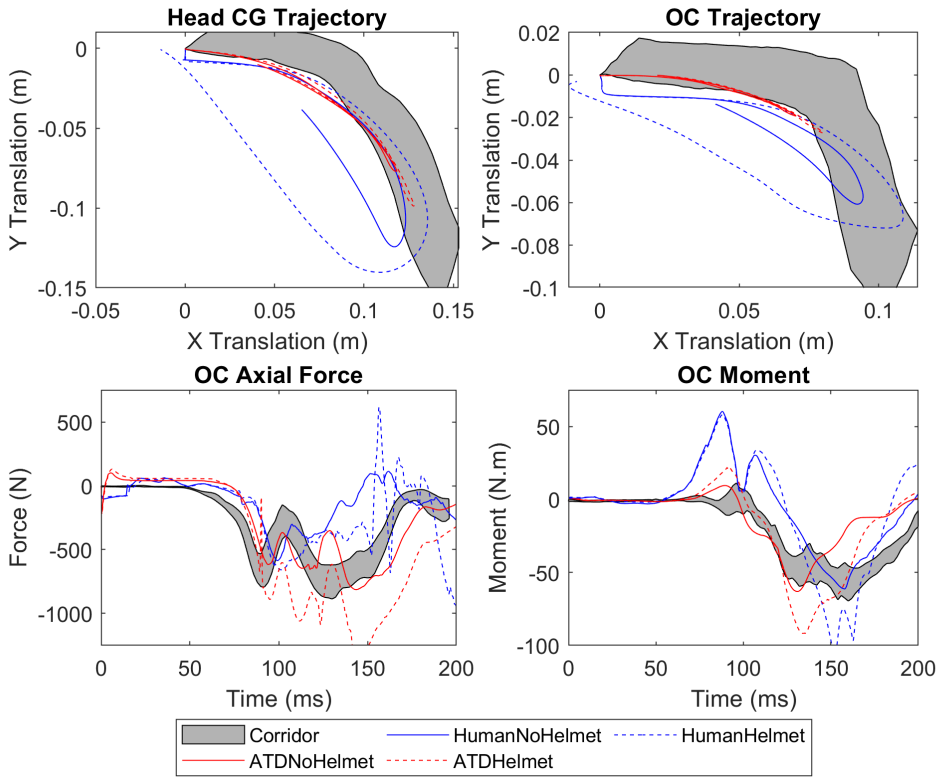

Figure 5.1: Comparison graphs of human and ATD models, with and without helmets, for validation acceleration pulse.

The head CG trajectory shows that all four model responses follow a very similar initial path up until the maximum displacement of the ATD without a helmet. At this point, the ATD without a helmet rebounds along a similar trajectory as it had just taken. This trajectory appears to be nearer to the validation corridor than the human model. The ATD with a helmet's trajectory is also very similar to the ATD without a helmet, except that it displaces further before rebounding. Both human models differ from the ATD models in the sense that the trajectory

has a more rounded shape. On the rebound, the distance between the base of the neck and the head CG shortens and therefore the trajectory follows a new path on the rebound. The rounded shape of the response of the human with helmet model is more exaggerated in comparison with the human without helmet model.

The OC trajectory shows very similar features to the head CG trajectory. Both the ATD models follow the same path on rebound as on the initial extension while the model with a helmet only displaces further. The ATD without a helmet's trajectory stays within the validation corridor, but does not extend as far as the corridor predicts which is possibly due to the higher stiffness of the ATD. The human models show rounded trajectories due to axial displacement within the neck from tension and compression. The helmeted human model once again shows an exaggerated trajectory in comparison with the model without a helmet.

Both the head's CG and OC trajectories show that the human model with a helmet rebounds much further than the human model without a helmet, in the same amount of time. This is expected since the forward displacement is greater and this results in the non-linear springs producing a significantly larger force that causes a greater acceleration and results in a quicker rebound. The initial forward displacement is greater due to the additional mass of the helmet.

The potential problem of the shorter displacement of the ATD models is with respect to the HNR tether. As the head displaces in the y-direction, the angle between the attachment point on the helmet and the attachment point on the HNR changes. Therefore the human models will have a greater change in angle than the ATD models. If it is assumed that the angle of the tether of both models at the maximum NIC is the same, then it follows that the initial angles of the tethers must be different due to the greater change in angle of the human model's tether angle. The converse of this implies that the optimal tether angle for the ATD model will not provide the optimal support for the human model.

The graph of the OC moment in Figure 5.1 shows that the maximum magnitude of the human and ATD models without helmets are within 3 % of each other, even though the ATD experiences a slightly quicker rise time. Similarly, the maximum magnitudes of moment of the two helmeted models are within 10 % of each other. It is concerning that the human models show a very large spike prior to 100 ms which is not exhibited by the ATD models and this should be monitored while determining the N_{ij} NIC. A maximum N_{ij} NIC for the human models prior to 100 ms could be related to the spike and therefore not predictive of injury.

The axial force graph shows that all four sets of results start similarly, but after 100 ms, each of the graphs have a widely differing range of values. Between the two models without helmets, the graphs diverge at about 125 ms and where the ATD model reaches its maximum magnitude, the human model has a near-zero force. Toomey *et al.* [82] conducted tests with real-world set-ups where it was found that the ATD's initial axial loading is very similar to a human's axial loading. However, once the externally applied forces overcame the initial stiffness of the human neck, the axial force experienced by the ATD increases in compari-

son with that which a human would experience. Even though the results align with that which Toomey *et al.* [82] found, the difference between the measured axial forces is problematic because at the same time as the maximum axial force magnitude of the ATD model, the model is experiencing a high moment magnitude and it will be expected that the maximum N_{ij} NIC will be experienced near this time. Therefore, the maximum N_{ij} NIC of the ATD model will have significant contributions from both the OC moment and axial force, while the human model will rely on the contribution from the OC moment to predict the risk of injury.

The combination of the OC moment and axial force in the N_{ij} NIC makes for a more robust prediction of injury, but it has been shown that there are potential problems with the prediction of the axial force by the human model. An alternative to optimising the angle of the tether based on the maximum N_{ij} NIC would be to only optimise based on the maximum predicted moment. It could be argued that the predicted optimal angle would not hold in real-life, but this would be able to determine if there is a difference between the ATD and human predicted angles.

5.2 HNR Certification Acceleration Profile

The second comparison applies the acceleration profile associated with HNR certification testing to both the ATD and human models with and without helmets [9]. The certification testing only provides the acceleration for the sled, but the models require the acceleration at the base of the neck. Such data was not available, but acceleration profiles of the chest are available and are assumed to be close enough to the base of the neck to be used as the input acceleration profile. This profile is shown in Figure 5.2 [83].

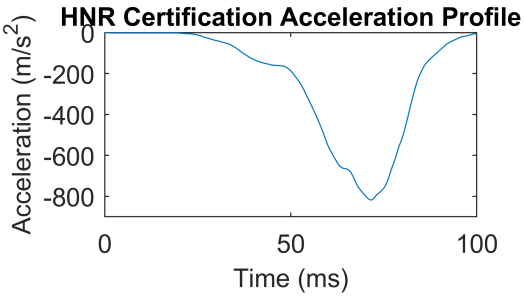

Figure 5.2: Assumed acceleration of the T1 vertebra during HNR certification

The four sets of results from applying the acceleration profile in Figure 5.2 to the models are shown in Figure 5.3. Once again, these results are limited to the head's CG and OC trajectories and the OC moment and axial force graphs. No validation corridors are included in these these graphs since none were found for this acceleration profile.

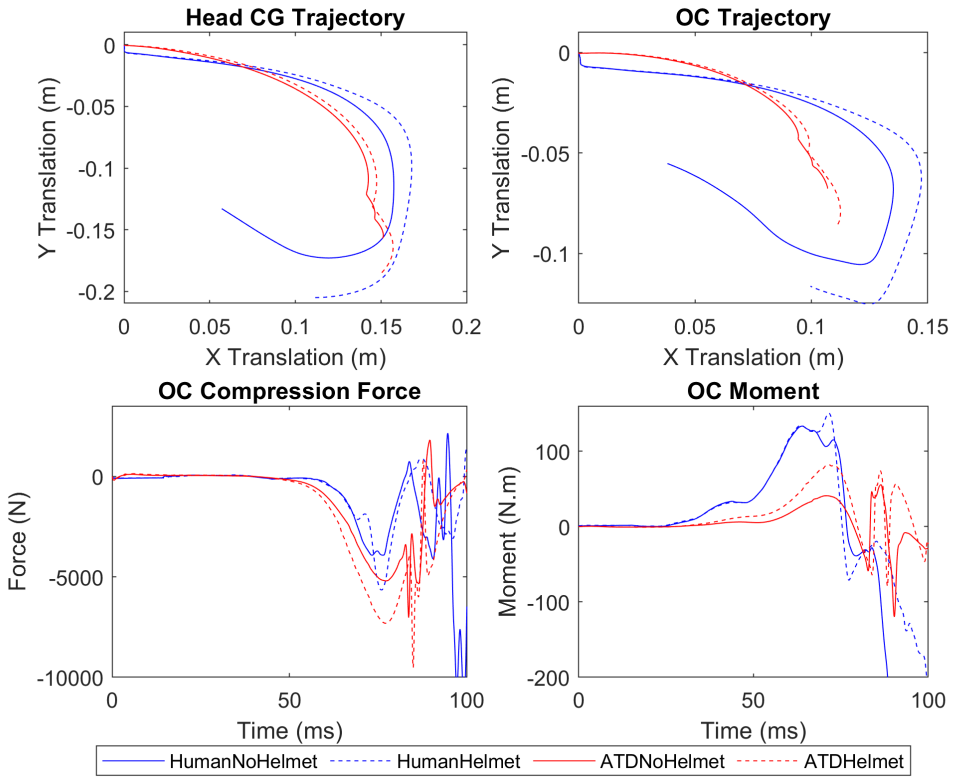

Figure 5.3: Comparison graphs of human and ATD models, with and without helmets, for HNR certification acceleration pulse.

With respect to the head's CG and OC trajectories, the same comments about x- and y-displacement as mentioned in Section 5.1 can be made even though the displacements are greater. The major difference here is that the ATD models exhibit a strange disturbance in trajectory at the start of their rebounds. This disturbance results in an increase in both x- and y-displacement and is due to the head making contact with the base of the neck. Fitting an HNR tether is believed to prevent such contact from being made.

The non-helmeted ATD's disturbance in trajectory occurs at 82.7 ms, while the helmeted ATD's disturbance occurs at 84 ms and these disturbances feature on both the OC axial force and moment graphs. In both these graphs, this is shown as large, high frequency oscillations. These oscillation are not representative of the human response and would not occur if the head did not make contact with the base of the neck. Once the tether is attached to the helmet it is believed that the unexpected OC axial forces and moments should not occur.

The helmeted and non-helmeted human models appear to have more normal trajectories, but the OC moment and axial force graphs still predict unexpected, large spikes in the data. These spikes may be related to the greater displacements experienced in trajectory due to the greater forces generated by the ligaments and IV discs as they stretch further. The higher magnitudes of force result in the head rebounding from the maximum displacement with greater ac-

celeration. Within the simulation, this has a ripple effect where the model overshoots its starting position, which causes other force-generating components to overextend, thereby causing excessive forces. This all results in the model appearing to be out of control and generating inaccurate predictions. Therefore, it is safe to assume that the results from the model as it rebounds are questionable and should not be trusted due to the excessive displacement of the head's CG and OC. This assumption correlates with the results in Figure 5.3 since the model starts its rebound at 81.8 ms without a helmet and 80.6 ms with a helmet and these times are just prior to the large unexpected spikes in OC moment and axial force.

Prior to the unreliable portions of the predicted OC moments and axial forces, the human models predict similar trends. With respect to the axial forces, all four simulations predict a peak magnitude between 75.9 ms and 77.2 ms, but the magnitude of human models are about 75 % of the magnitude of the ATD models for both non-helmeted and helmeted. In contrast with the axial forces, the predicted maximum moments of the human models are much greater than that of the ATD models. The maximum moment predicted for the human model is 2.7 and 1.8 times greater than that of the ATD for the non-helmeted and helmeted models, respectively.

5.3 Comparison Conclusion

The human and ATD models were compared to each other with and without helmets for two different acceleration profiles. The first acceleration profile is the same as what was used for validation of the human model in Section 4.5. This showed that the maximum OC moments predicted by the human and ATD models correlate very well, which is good for calculating the N_{ij} NIC. However, the OC axial force predictions of the human and ATD models differ greatly, which complicates the N_{ij} NIC calculations.

The second acceleration profile used is obtained from the HNR certification test and exhibits much higher acceleration magnitudes. Due to multiple concerns, the predictions of the models are only feasible up until the rebound of the head. Prior to the rebound, the OC axial force predicted by the ATD model is slightly greater than that which is predicted by the human model, while the OC moment predicted by the ATD model is significantly smaller than that which is predicted by the human model.

It is not possible to say from these results that either the OC moment or axial force is more reliable, but the differences could be manifestations of underlying problems. Moving forward, it will be necessary to consider not only the combination of the OC moment and axial force in the form of the N_{ij} NIC, but to also consider the OC moment and axial force independently. This may be done in the manner of finding an optimal tether angle for each of the N_{ij} NIC, moment and axial force and then comparing those results.

Chapter 6

Tether Optimisation

Development of the ATD and human models was necessary to determine the optimal tether orientation. This chapter discusses the method in which the tethers are modelled and applied to the ATD and human models, as well as the optimisation procedure. Thereafter, the results are given and the chapter concludes with a discussion of the results.

6.1 Tether Model

The HNR is dependent on the tether that limits the frontal flexion of the head relative to the torso. Therefore, in order to be able to optimise the angle at which the tether should act to minimise potential injuries, the tether needed to be modelled so that it could be implemented on the models. The relevant standards do not specify the materials from which the tether should be made [2; 9]. However, the FIA standard for seatbelts specify that seatbelts should be made from webbing consisting of polyester or other webbing material provided that it complies with the strength requirements [1]. Therefore, it was assumed that the tether will also be made from webbing.

The webbing of the tether was modelled as a spring. Since the webbing can be made out of a combination of materials, it was difficult to predict the force-to-displacement curve that will model the tether. In general, the force-deflection curve of webbing is non-linear with a slight increase in stiffness of the webbing as it is stretched [84; 85]. Standard FIA 8858-2010 [2] specifies that the webbing is only tested to 7 kN, which is relatively low in comparison with the maximum forces that webbing can withstand and therefore it was assumed that the webbing would still be in a near-linear region [84; 85]. The tether was thus modelled as a linear spring.

The maximum allowable displacement of the tether under a 7×10^{-3} N load is 0.04 m [2]. Therefore, it was assumed that the minimum spring constant should be 175×10^{3} N/m. While this value provides a good estimation, there was no evidence to justify the use of this spring constant for all tethers. Alternatively, the tether's properties could have been experimentally determine, but this was decided to be excessive for the purpose of these models which was to offer a comparison between the human and ATD models. Therefore, it was decided that the spring constant should be left as a variable and the optimisation process can determine the most suitable value. This will have the added benefit of determining

how great an impact the tether's mechanical properties have on the effectiveness of the HNR.

6.2 Implementation in Model

The spring model of the tether was included on the MSC Adams model as forces acting on the helmeted head. The effect of the helmet in terms of mass and moments of inertia was calculated in Section 5.1 and applied to the original head in the same manner. In order to apply the force directly to the head, two assumption were made: firstly, the helmet cannot rotate independent of the head and secondly, the spring constant of the tether accounts for any linear displacement of the helmet relative to the head from compression of the helmet's inner sponge.

The two ends of the tether will be referred to as the fixed end and the moving end, where the fixed end is attached to the HNR's shoulder support and the moving end is attached to the model's head. The fixed end was placed relative to the first thoracic vertebra at a location behind the neck such that the fixed end will maintain its position relative to the first thoracic vertebra while the model accelerates. The location at which the moving end of the tether acts relative to the head's CG is 85.8×10^{-3} m posterior, 29.1×10^{-3} m inferior and 90.0×10^{-3} m lateral [3; 4; 86]. The tether has two attachment points on the helmet and therefore two forces were placed on the head, symmetric about the mid-sagittal plane.

The spring model was implemented in Simulink with constants containing the coordinates of the fixed end, the length of slack in the tether and the spring constant. The coordinates of the moving end of the tether, measured from the first thoracic vertebra, are passed from MSC Adams to Simulink through co-simulation. The force that the tether acts with along each of the axes is calculated in Simulink and then passed back to MSC Adams.

The optimisation process was initially performed on the simple case of one pair of tethers acting on the head at a specified angle, as shown in Figure 6.1. The tethers were only defined to act parallel to the motion of the model due to the model only being validated for frontal collisions and therefore the z-coordinate of the fixed end was equal to the starting z-coordinate of the moving end. The angle was used to calculate the x- and y-coordinates of the fixed end based on a constant tether length and a constant slack length. Therefore, two constants needed to be defined prior to starting the optimisation process. The first was the length of the tether, which is 0.14 m, and the second was the slack length in the tether, which equals 0.02 m [87]. The only design variables are the tether angle and the tether's spring constant.

Three potential objective functions are available for the optimisation problem. The options are the minimum N_{ij} NIC, the minimum OC moment or the minimum OC axial force. The N_{ij} is the sum of the linearly scaled OC moment and axial force such that a value greater than one indicates injury. The maximum pure flexion moment associated with injury is 310 N m while the maximum extension moment is 135 N m and the maximum pure axial force in compression is

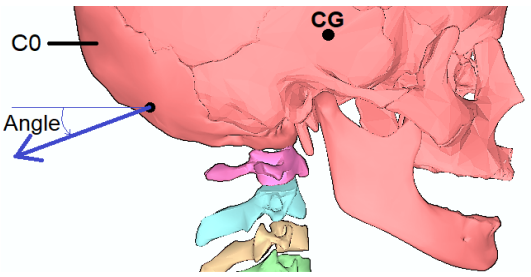

Figure 6.1: Sagittal view of one-tether attachment and tether angle

6160 N, while in tension is 6806 N [29]. Since the N_{ij} indicates that the required moment for injury in extension is less than in flexion, it will also be necessary to scale the maximum moment according to the same maximum moment values as in the N_{ij} prior to using the maximum moment as an objective function. This is also necessary for the axial force objective function for similar reasons. Therefore, each of the possible objective functions indicate injury at a value of one and are thus comparable.

The Bayesian optimisation method with a maximum of 30 function evaluations was used to determine the optimal angle and spring constant. The final GP model that was generated can be used to predict the objective function values at any point within the range of the variables. This may provide insight into the overall effect of each of the variables.

The optimisation problem was expanded to include two other set-ups of the HNR tethers. The first of these is a set-up with two tethers, both acting at the same point on the helmet. This set-up has four optimisable parameters with each of the tethers having a variable angle and spring constant. The two-tether set-up is shown in Figure 6.2. The second set-up consists of a single tether where the attachment point on the helmet is adjustable. This is referred to as the adjusted-one-tether set-up. This set-up requires five design variables, where tether angle and spring constant are the same as previously defined, but x- and y-displacement and tether length are new variables. The x- and y-displacement are defined relative to the previous attachment points, as seen in Figure 6.2. It was decided to add the tether length as a variable since the adjustment of the attachment point on the helmet may make the tether too short to effectively be able to attach to the HNR.

A total of seven design variables were generated for all three set-ups. These variables are listed in Table 6.1 along with the range of values for which they are defined in the optimisation problem. The ranges are only defined if the set-up requires the variable, otherwise the range is left blank.

6.3 Optimisation Results

A total of 18 sets of results were generated by the optimisation process. This was due to each model having three tether set-ups and three possible objective func-

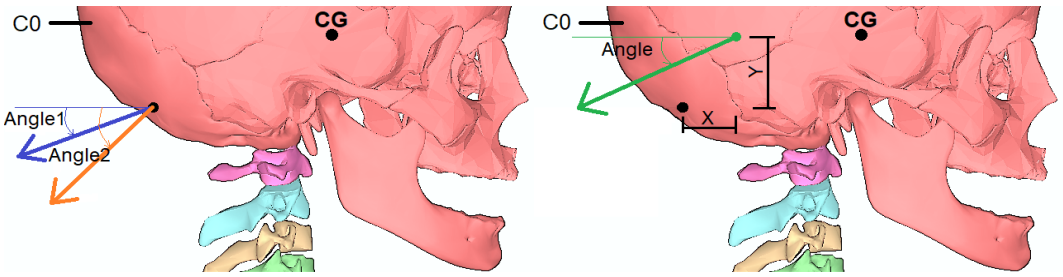

Figure 6.2: Sagittal view of two-tether attachment (left) and adjusted-one-tether attachment (right) with tether angles indicated

Table 6.1: Range of values associated with each variable related to each of the set-ups

Variable	1-Tether	2-Tether	Adjusted-1-Tether
Angle 1 (degrees)	-45 to 90	-45 to 90	-45 to 90
Angle 2 (degrees)	-	-45 to 90	-
Spring Constant 1 $\times 10^3$(N/m)	50 to 250	50 to 250	50 to 250
Spring Constant 2 $\times 10^3$(N/m)	-	50 to 250	-
Tether Length (m)	-	-	0.08 to 0.2
X Displacement (m)	-	-	-0.05 to 0.1
Y Displacement (m)	-	-	-0.05 to 0.1

tions. The results include a list of the optimal values for the design variables and the final GP model.

6.3.1 Optimal Value Results

The optimal values of the design variables are shown in Table 6.2, Table 6.3 and Table 6.4. Each of the tables follow the same structure of seven columns with the first column giving the name of the design variable, the second to fourth columns giving the results for each of the objective functions using the ATD model and the last three columns giving the results for each of the objective functions using the human model.

The various optimal values of the parameters were applied to their respective models in order to measure the OC moment and axial force and then to determine the N_{ij} NIC. Figure 6.3 shows each tether set-up's maximum N_{ij} value predicted for each of the objective functions. The figure also indicates the maximum N_{ij} predicted for both the human and ATD models without a tether attached. Based on the maximum N_{ij} values, the tethered models' N_{ij} values are less than 60 % of the untethered models' values due to the addition of the tethers and therefore, none of the tether set-ups predict injury.

There are two other aspects worth noting in Figure 6.3. Firstly, for the ATD

Table 6.2: Values of the optimised parameters using the one-tether set-up for each of the possible objective functions

	ATD 1-Tether			**Human 1-Tether**		
Variable	**N_{ij}**	**Moment**	**Force**	**N_{ij}**	**Moment**	**Force**
Angle 1 (deg)	-0.15	9.99	-17.77	8.83	-1.97	0.57
Spring Constant 1 $\times 10^3$ (N/m)	248.6	140.5	248.4	172.5	158.5	200.9
Function Value	0.362	0.048	0.153	0.501	0.470	0.112

Table 6.3: Values of the optimised parameters using the adjusted-one-tether set-up for each of the possible objective functions

	ATD Adjusted-1-Tether			**Human Adjusted-1-Tether**		
Variable	**N_{ij}**	**Moment**	**Force**	**N_{ij}**	**Moment**	**Force**
Angle 1 (deg)	-5.33	-28.30	-0.29	-26.33	-22.31	-9.59
Spring Constant 1 $\times 10^3$(N/m)	119.4	127.4	185.6	149.1	247.5	248.8
Tether Length $\times 10^{-3}$(m)	198.0	199.7	110.9	199.4	136.0	83.8
X Displacement $\times 10^{-3}$(m)	17.0	-49.9	99.1	12.5	-19.0	61.6
Y Displacement $\times 10^{-3}$(m)	26.4	38.9	47.8	38.6	45.5	19.9
Function Value	0.142	0.110	0.085	0.412	0.394	0.066

Table 6.4: Values of the optimised parameters using the two-tether set-up for each of the possible objective functions

	ATD 2-Tether			**Human 2-Tether**		
Variable	**N_{ij}**	**Moment**	**Force**	**N_{ij}**	**Moment**	**Force**
Angle 1 (deg)	-13.78	12.44	-11.90	3.67	-3.58	-8.24
Angle 2 (deg)	-11.89	-9.42	-11.37	-44.19	26.16	2.76
Spring Constant 1 $\times 10^3$(N/m)	102.9	131.4	238.3	206.9	110.4	219.6
Spring Constant 2 $\times 10^3$(N/m)	243.0	53.6	246.7	157.2	50.8	57.5
Function Value	0.351	0.082	0.115	0.531	0.466	0.122

model, the one-tether and two-tether set-ups predict values that are very similar between the various objective functions, while the adjusted-one-tether set-up predicts a large change in N_{ij} values. The second aspect is that the human set-ups predicted values that are very similar to each other and therefore the minimum predicted N_{ij} is 0.41, while the maximum is 0.57.

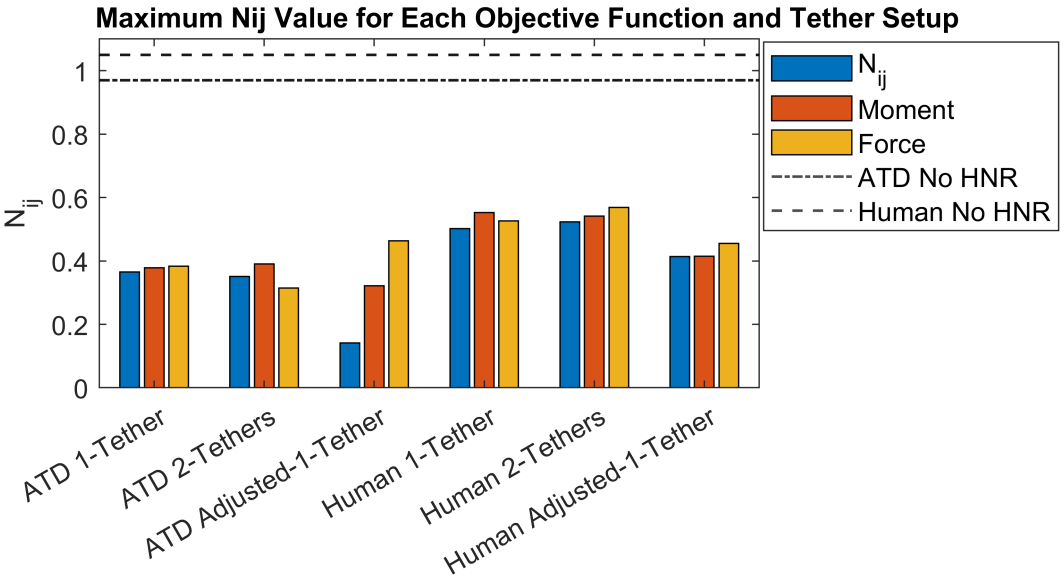

Figure 6.3: Bar plot of the maximum predicted N_{ij} with the model set-ups on the x-axis and the optimisation objectives indicated in the legend (Horizontal lines indicate the maximum values obtained without the use of an HNR)

Figure 6.4 and Figure 6.5 show the maximum and minimum values of OC moment and axial force, respectively. Both these graphs have the objective function indicated in the legend and also include the maximum and minimum values predicted without the tether. In the case of the moments, Figure 6.4 shows flexion as positive and extension as negative. For axial forces, Figure 6.5 shows compression as positive and tension as negative.

The average flexion moments of the ATD and human models are 34 N m and 140 N m respectively, while the average extension moments are 15 N m and 59 N m respectively. For the ATD model, the tether resulted in an average decrease of 59 % in the maximum flexion values and 69 % in the maximum extension values, while the human model's average maximum flexion and extension values decreased by 7 % and 17 %, respectively. The average compression forces of the ATD and the human models are 1013 N and 854 N respectively, while the average tension forces are 591 N and 749 N respectively. The untethered models both predicted negligent compression values and the therefore the tethered models' compression values are five to nine times that of the untethered values. Even though such a great increase is measured, the compression values are still

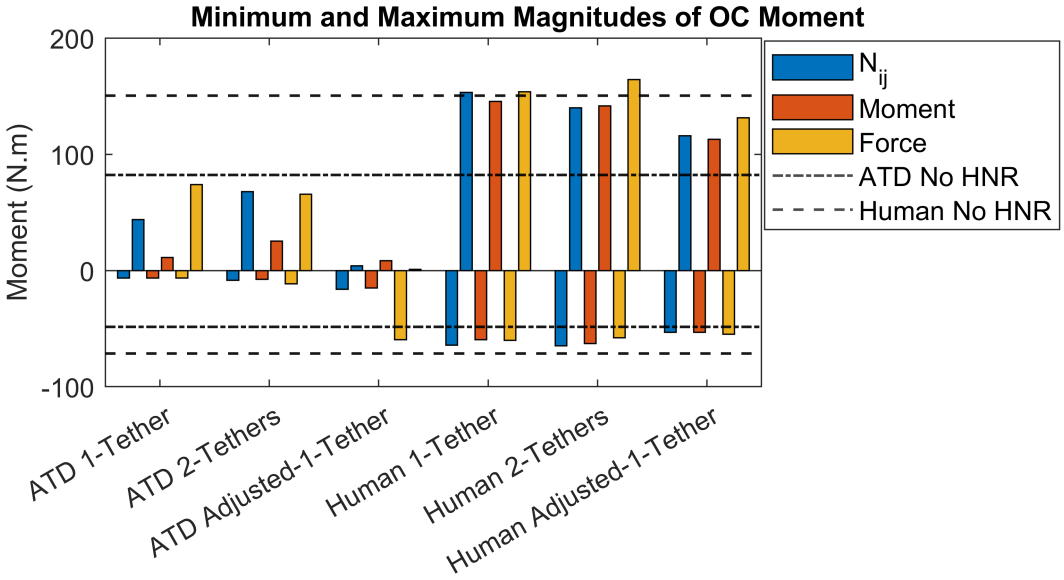

Figure 6.4: Bar plot of the maximum and minimum predicted OC moments with the model set-ups on the x-axis and the optimisation objectives indicated in the legend (Horizontal lines indicate the maximum and minimum values obtained without the use of an HNR)

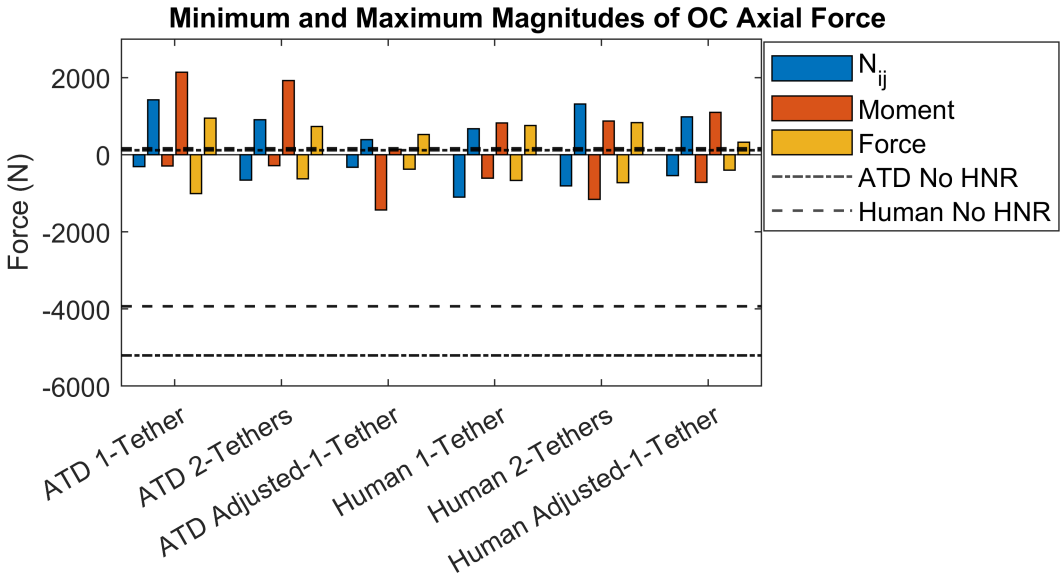

Figure 6.5: Bar plot of the maximum and minimum predicted OC axial forces with the model set-ups on the x-axis and the optimisation objectives indicated in the legend (Horizontal lines indicate the maximum and minimum values obtained without the use of an HNR)

less than 16 % of the intercept values used to calculate the N_{ij}. The ATD and human model's maximum tension values are reduced by 87 % and 81 % from that of the tethered models, respectively. While the tethered models do experience an increase in compression values in comparison to the untethered models, the overall maximum magnitude of the axial forces decreases due to the significant decrease in tension values, and this indicates an overall decrease in the risk of injury.

The large change in N_{ij} values between the various objective functions of the adjusted-one-tether set-up ATD can be explained by investigating the graphs of the maximum OC moment and axial force. These graphs show that while optimising for the moment, the maximum axial force increases and vice versa. The exception is that, when optimising for N_{ij}, both the maximum OC moment and axial force are similar to their optimised values when optimising for each individually. This proves the worth of using the N_{ij} since it provides the optimal solution when both the OC moment and axial force needs to be taken into account.

The minimum and maximum moments predicted for the human model show that optimising for moments always yielded the smallest value, but the moments measured for the other objective function were only 2.5 % greater on average. The adjusted-one-tether set-up predicted the smallest maximum moments, while the remaining two set-ups' values were about 20 % greater. Considering the predicted axial forces for the human model, it is once again observed that the minimum axial force per set-up was observed while using the force objective function. The adjusted-one-tether set-up showed a decrease in predicted axial force from the N_{ij} of 65 %, while the other set-ups only showed an average decrease of 21 %.

6.3.2 GP Model Results

The GP model is used to predict the objective function value at any point on the range of each of the design variables. This prediction is based on the 30 points that were sampled during the Bayesian optimisation procedure. The model can be used to interpret the effective contributions of each of the design variables to the optimal value and thereby the importance to the optimal tether set-up.

The Shapley value is a method for determining the relative contributions of features at a specific point of investigation. The formula for the Shapley value was given in Lundberg and Lee [88] as

$$\phi_i = \sum_{S \subseteq F \setminus \{i\}} \frac{|S|!\,(|F| - |S| - 1)!}{|F|!} \left[f_{S \cup \{i\}}\left(x_{S \cup \{i\}}\right) - f_S\left(x_S\right) \right] \tag{6.1}$$

where i is the variable in question, f is the GP model, F is the collection of all variables and S is a subset of F excluding i. The simplest interpretation of this formula is that it is the weighted average of the difference between excluding and including the variable i for all possible subsets of the remaining variables. In order to compute this, excluding variables were interpreted as the mean of all func-

tion evaluations where the excluded variables cycle through each possible number combination within their ranges. In contrast, to include a variable meant that the variable's value remains set to a constant that had been provided as the point of investigation. Implementing this approach on mathematical models is referred to as SHapley Additive exPlanations (SHAP) [88].

The ranges of each of the variables were limited to a discrete set of values that correspond to the points that were sampled during the Bayesian optimisation process. Since the GP model's predictions at these points are the exact values predicted by the human or ATD models, calculating the SHAP values based on these limited ranges would be the equivalent of calculating the SHAP values directly on the human or ATD models. This removes the risk of making incorrect assumptions about the variable importances based on the estimates of the GP model.

A feature of the SHAP values is that the sum across each of the variables yields the difference between the function value at the point of investigation and the mean across all other points. Therefore, it was possible to scale the SHAP values according to the total difference such that the sum of the scaled SHAP values will equal 100 percent. This allowed for easier comparison between different set-ups and objective functions.

Since the SHAP value requires an investigation point, it was logical to calculate the value for each of the design variables at the point where the minimum objective function has been located. Figure 6.6 includes the scaled, relative contributions as percentages based on the calculated SHAP values for each of the set-ups and objective function. Within the bar chart, the order in which the variables appear from top to bottom corresponds to the decreasing mean of the three bars.

The tether angle for the two one-tether set-ups in Figure 6.6 has a much larger effect than the spring constants. However, comparing the mean spring constant contributions shows that the human model's is 29 %, whereas the ATD model's is 18 %. This could indicate that the spring constant value has greater importance in the human model than the ATD model.

Both the adjusted-one-tether set-ups in Figure 6.6 list tether angle and y-displacement as the first two variables and thereby indicate that they have the greatest effect on both models. On average, these two variables account for 85 % of the total effect on both models. With the ATD model, the tether angle always has a greater effect than the y-displacement. This same relationship does not exist in the human model, where the y-displacement has the greatest effect for the N_{ij} and force objective functions and the tether angle has the greatest for the moment objective function.

With respect to the two two-tether graphs in Figure 6.6, the same is shown as in the one-tether set-ups, where the tether angles always have a greater effect than the spring constants. For the human model, the first tether angle dominates with a 77 % contribution on average, while the other angle only contributes an average of 11 % to the total effect. Similarly, the ATD model shows that the first

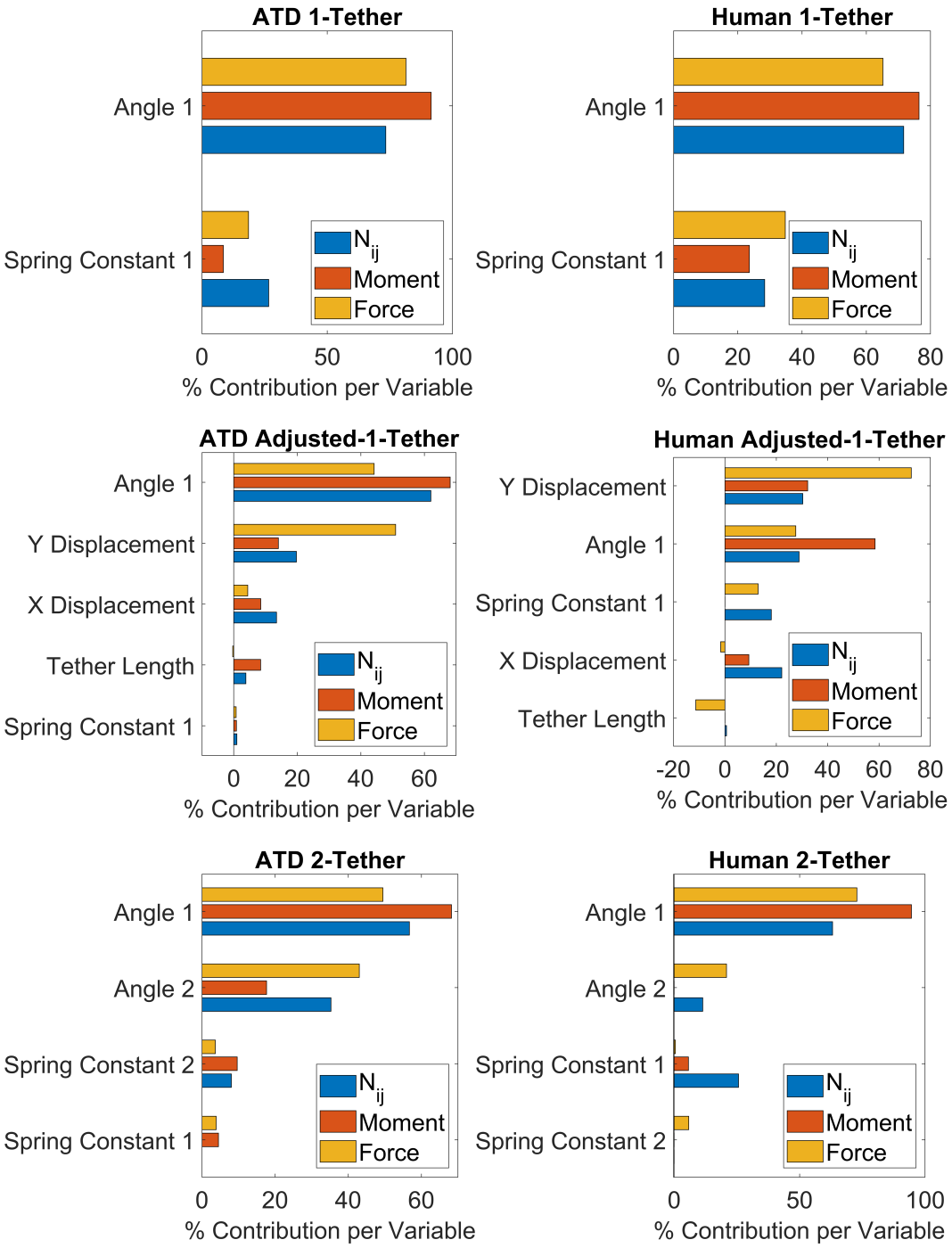

Figure 6.6: Bar chart of SHAP values for each tether setup and objective function

angle accounts for an average of 58 % of the total effect on the model, while the second angle accounts for 32 % of the effect on average.

6.4 Discussion

The results provided in Section 6.3 are extensive, but meaningless without interpretation. Therefore, it is important to highlight certain aspects of the results that can be used to form meaningful conclusions. This section is sub-divided into a general discussion and then discussions specific to each of the tether set-ups.

6.4.1 General

The first aspect to discuss is the use of SHAP to interpret the contributions that each variable makes. One drawback of SHAP is that it does not give a global interpretation of the variable effects, but is rather limited to the given point of investigation. This would have been problematic if it were necessary to understand the effects of the variables over the full range of values, but since the aim has been to determine the optimal variable values, it is logical that the effects of the variables need only be known at these optimal points. SHAP also has the advantage over many global interpretation methods in the sense that it only needs the points that have already been sampled during the Bayesian optimisation procedure to calculate the SHAP value. Therefore, it does not have to estimate the points according to the GP model where the GP model's uncertainty is high. This also means that the SHAP values are directly calculated for the head and neck models, and not for the GP model that estimates the objective function values of the head and neck models. Therefore, SHAP is applicable for the given circumstances.

A general comparison of the ATD and human models shows that the human model predicts an N_{ij} value that is on average 45 % greater. Breaking the N_{ij} into its components, it was calculated that the moments and axial forces of the human model experience a 157 % increase and a 20 % decrease, respectively, in comparison with the ATD model. These differences were predicted in the conclusion of Chapter 5. Furthermore, the N_{ij}, moment and axial force values should not be compared directly between the models, but rather used for relative comparison between the various set-ups of the same model.

While the differences in predicted values between the two models seem significant, it is important to remember that the tether reduces the N_{ij} by more than 50 % on average for both models. In order to achieve this, it appears as though the tether reduces the maximum magnitude of the moment or force by increasing its maximum magnitude in the opposite direction. The overall smallest maximum force or moment is usually found when their scaled maximum and minimum value magnitudes are equal.

6.4.2 One-Tether Set-Up

The differences in tether angles between the ATD and human models for N_{ij}, moment and force objective functions are nine, 12 and 18 degrees, respectively. This indicates that the optimal tether angle determined using an ATD should not be assumed to be the same for a human. The human model shows that at 8.83 degrees below the horizontal, the HNR is most effective at minimising the risk of injury.

The effectiveness of the HNR is dominated by the tether angles according to the SHAP values, however the spring constant's effect is more significant in the human model. The implication of this is that testing real-world tether straps with varying spring constants on ATDs will have less of an effect than that which would be experienced by a human. This is also seen where the range of optimal spring constant values for the ATD is more than double that of the human model's spring constant values.

6.4.3 Adjusted-One-Tether Set-Up

The adjusted-one-tether set-up results in N_{ij} values for the ATD and human models that are lower than the other set-ups by 0.05 and 0.11, respectively. This appears to be possible due to both the moments and axial forces being able to achieve lower maximum values when optimising for moments and forces, respectively. The downside is that, as the maximum moment decreases, the maximum force increases and vice versa. Therefore, it is critical to optimise for the N_{ij} value.

According to the SHAP values, the one of the greatest contributors to the improved results is the optimal tether angle. The average tether angles of the ATD and human models are 11 degrees and 19 degrees, respectively, above the horizontal. The differences in tether angles between the ATD and human models for each of the objective functions are 21, six and nine degrees, which shows that similar to the one-tether setup, the two models require different angles in order to minimise the risk of injury.

Across both models, the proposed x- and y-displacements are on average 20.2×10^{-3} m and 36.2×10^{-3} m, respectively, while their standard deviations are 49.10 and 9.96, respectively. This indicates that the both the models, with all their set-ups, suggest y-displacement values that are very similar to each other when compared to the x-displacement. Combining this fact with the knowledge that the SHAP value implies that the y-displacement is equally as important as the tether angle, would suggest that the location of the attachment point in the y-direction should be changed. Irrespective of the model, it is believed that raising the attachment point by 36.2×10^{-3} m will result in a tether that can reduce the risk of injury even further.

6.4.4 Two-Tether Set-Up

Two options are identified from the results for the manner in which the optimal tethers are set up. The first is that both tether angles could be nearly identical, in which case these tethers could be combined into one. Consulting the SHAP values suggests that the effectiveness that each tether provides is very similar and therefore supports the idea that they could be joined into a single tether. The second option is that one of the second tether's parameters is very near to the search boundary of the optimisation problem. This results in a tether that either has a very low spring constant or a large angle from the horizontal and therefore does not is not very effective at producing a force to counteract the forward motion of the head. The SHAP values associated with the second tether in these set-ups show that the second tether does not appear to provide any meaningful benefit.

The two-tether set-up results in nearly no change in the N_{ij} in comparison with the one-tether set-up. The only advantage of this set-up is that it appears to reduce the average maximum moment slightly, but this is at the expense of increasing the maximum axial force. In general, the additional complexities of adding a second tether cannot be justified if the N_{ij} does not predict better results than the one-tether set-up and therefore the two-tether set-up should not be considered a viable solution.

Chapter 7

Conclusion

The aim of this project was to determine the optimal angle at which the tether in an HNR system should attach to the helmet to minimise the risk of injury. Secondary to this, the project also aimed to investigate the differences between the Hybrid III ATD neck and the human neck. These differences were considered within the specific context of the HNR system. These aims required the building and validation of two models in simulation software which were based on the head and neck of an ATD and a human.

The model of the ATD head and neck represented the aluminium components as solid bodies, while the rubber components were converted into a combination of springs and dampers. This model was validated against the neck calibration test for Hybrid III ATDs. It was found that the response of the model deviated from the validation data after reaching a maximum forward displacement. While undesirable, it was determined that this should not have a significant effect on the model's ability to predict the risk of injury using the N_{ij} NIC since the NIC uses the maximum combination of moments and forces which was found to approximately coincide with the maximum displacement.

The human head and neck model represented the vertebrae and skull as solid bodies, while the ligaments, IV discs and muscles were modelled as forces which control the motion of the solid bodies. The model was validated against data obtained from human volunteers that were subjected to a low-acceleration frontal impact. While the model's response was found to be similar to that of the human volunteers, the main concern was related to the OC axial force and moment. Both these measurements showed similar ranges of values to the validation data and this would be good for the calculation of the N_{ij} NIC, but there were also unexplained spikes that differed from the validation data. It was decided that the model may be used for further work provided that further work does not rely solely on the NIC, but also investigates the OC axial force and moment.

As part of the aims of the project, a direct comparison was drawn between the two models using the acceleration profile used for HNR certification. It was found that both models provide unreliable results while rebounding. Prior to the rebound, the results showed that the ATD predicted higher axial forces that the human model, while the human model predicted higher moments. This enforced the idea that it was necessary to investigate the NIC, OC axial force and OC moment individually while testing the HNR tether.

Determination of the optimal angle of the tether was conducted using three

tether set-ups that were optimised for individually. The tethers were modelled as linear springs acting from a specified point on the helmet to a fixed point determined by the tether angle at the start of the simulation. The one-tether and two-tether set-ups applied their forces on the helmet at a point determined from the applicable standards. The adjusted-one-tether set-up expanded on the one-tether set-up by allowing the attachment point on the helmet to move. It was found that the two-tether set-up does not reduce the risk of injury more than the one-tether set-up while the adjusted-one-tether set-up provides a substantial decrease in the risk of injury.

An analysis of the relative importances of the tether parameters using SHAP revealed that the tether angle had the greatest influence on the one-tether set-up's effectiveness. For the human model, the optimal tether angle was found to be 8.83 degrees below the horizontal. An average difference of 13 degrees was found between the optimal tether angles of the human model and the ATD model. This indicates that real-world HNRs that have been designed using Hybrid III ATDs may not be optimally designed for human users.

Similar to the one-tether set-up, SHAP revealed the tether angle to be one of the most significant parameters for the adjusted-one-tether set-up, while the tether's attachment height on the helmet was found to be the other most significant parameter. Again it was found that there was a difference between the optimal tether angles for the human and ATD models, but both models suggest that the attachment point should be 36.18×10^{-3} m higher than it currently is. This can be further investigated using real-world tests since both models suggest a similar increase in height and therefore the effect of the increased height on the ATD could be similar to the effect which it would have on a human. Finally, the addition of a second tether to the HNR does not appear to improve the HNR's ability to reduce the risk of injury.

While this study yields some interesting results, there are at least two aspects that have not been considered due to the limits of the models. Firstly, the models were only designed for frontal impacts and therefore it was not possible to test the effect of the tether for oblique and lateral impacts. Secondly, the optimisation process solely relied on the N_{ij} NIC. While this is a good starting point, further work may discard the NIC and attempt to minimise the forces predicted for the ligaments and IV discs in the human model. Expanding on this, a FEM model may provide more accurate results in terms of the forces experienced by the ligaments and IV discs and therefore it may be necessary to build such a model to ensure that the optimal tether set-ups predicted in this project do not cause unintended damage to the neck.

Appendix A

Muscles of the Neck

The neck is made up of 30 identifiable muscles and most of these consist of pairs. Table A.1 provides a list of these specified muscles with their attachment points and their purpose.

Table A.1: List of neck muscles with their attachment points and functions

Muscle	Origin	Insertion	Purpose	Source
Scalene				
Scalenus anterior	C3 - C6 transverse process	Top border of 1st rib	Pull 1st rib up	[21]
Scalenus medius	C2 - C7 transverse process	Top border of 1st rib lateral to scalenus anterior	Pull 1st rib up	[21]
Scalenus posterior	C4 - C6 transverse process	Top border of 2nd rib	Pull 2nd rib up	[21]
Infrahyoid (4 muscles)	Sternum, clavicle and scapula	Hyoid bone	Lowers jaw during swallowing	[21]
Suprahyoid (4 muscles)	Skull	Hyoid bone	Lowers mandible and raises hyoid bone	[21]
Sternocleidomastoid	Mastoid projections beneath the ear	Sternum and first third of clavicle	Flexion and tilting of the head	[21]
Longus colli	Anterior tubercles and surfaces of C3 - T3	Anterior portions of C1 - C6	Neck flexion and some rotation	[22]
Longus capitis	Anterior tubercles of transverse processes of C3-C6	Basilar portion of the occipital bone	Neck and head flexion	[22]
Trapezius	Spinous process of C7, T1 - T10	Clavicle, acromion and scapula	Elevate and rotate scapula	[21]

Muscle	Origin	Insertion	Purpose	Source
Suboccipital muscles				
Rectus capitis posterior major	Spinous process of axis	Inferior nuchal line of occiput	Extension of head and neck	[15]
Rectus capitis posterior minor	Posterior tubercle on the atlas	Occiput	Extension of head and neck	[15]
Obliquus capitis inferior	Transverse process of C1	Spinous process of C2	Extension of head and neck	[15]
Obliquus capitis superior	Transverse process of C1	Between superior and inferior nuchal lines of occiput	Extension of head and neck	[15]
Splenius capitis	Spinous process of cervicothoracic vertebrae	Base of the occipital bone	Extension and lateral flexion	[15]
Splenius cervicis	Spinous process of cervicothoracic vertebrae	Transverse processes of upper cervical vertebrae	Extension and lateral flexion	[15]
Iliocostalis cervicis	Transverse processes of C4 - C6	Ribs 3 - 6	Extension and hyperextension of neck	[23]
Longissimus capitis	Transverse processes of T1 - T5 and articlular tubercles of C4 - C7	Mastoid process and temporal bone	Extension and hyperextension of head	[22]
Longissimus cervicis	Transverse processes of T1 - T5 and articlular tubercles of C4 - C7	Transverse processes of C2 - C6	Extension and hyperextension of neck	[23]

Muscle	Origin	Insertion	Purpose	Source
Spinalis cervicis	Spinous process of C4 - T2	Spinous process of C2	Extension and lateral flexion of neck	[22]
Spinalis capitis	Spinous process of C7	Between superior and inferior nuchal lines of occipital bone	Extension of head and neck	[22]
Semispinalis cervicis	Articular processes of C4 - C7 and Transverse processes of T1 - T6	Spinous processes of C2 - C5	Extension and rotations with lateral flexion of the neck	[22]
Semispinalis capitis	Articular processes of C5 - C8 and transverse processes of T1 - T6	Between superior and inferior nuchal lines of occipital bone	Extension and rotations of head and neck	[22]
Multifidus	Articular process of C4 - C7	Spinous process 2 - 4 bones above origin	Rotation and slight extension of vertebrae	[23]
Levator scapulae	Transverse processes of C1 - C4	Scapula	Lateral flexion and stabilization	[22]

Appendix B

ATD Rubber Disc Calculations

The calculations on the following two pages show how the initial spring constants were determined to be used in the ATD model. These calculations are only simplified expressions and therefore cannot be assumed to provide an accurate representation of a head and neck model.

ATD Model Initial Parameters

The rubber discs are modelled as cylinders to calculate the initial parameters.

$d := 63,754\ \text{mm}$

$h := 21,7932\ \text{mm}$

$E := 7\ \text{MPa}$ (Young's modulus)

$G := 3\ \text{MPa}$ (Shear modulus)

Cylinder Dimensions:

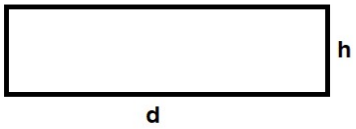

$A := \pi \cdot \frac{d^2}{4} = 3192,3078\ \text{mm}^2$

$I := \frac{1}{4} \cdot \pi \cdot \left(\frac{d}{2}\right)^4 = 8,1096 \cdot 10^{-7}\ \text{m}^4$

Bushing Linear Spring Coefficients

y-axis:

The bushing constraint does not resist movement in the y direction.

$k_y := 0\ \frac{\text{N}}{\text{mm}}$

x- and z-axis:

Based on the deflection equation of a beam.

Formula of a cantilever beam's deflection at its furthest point is given as

$$v = \frac{F \times h^3}{3EI}$$

where $I = \frac{1}{4}\pi r^4$ Rewriting this equation follows that

$$k_x = k_z = \frac{F}{v} = \frac{3EI}{h^3}$$

$k_x := \frac{3 \cdot E \cdot I}{h^3} = 1645,341\ \frac{\text{N}}{\text{mm}}$

$k_z := k_x = 1645,341\ \frac{\text{N}}{\text{mm}}$

Bushing Rotational Spring Coefficient

z-axis:

The bushing constraint does not resist movement about the z axis.

$k_{rz} := 0 \ \frac{\text{N mm}}{\text{rad}}$

x-axis:

The moment about point O is simply described by the formula:

$$M = \frac{2}{3} \times F \times r$$

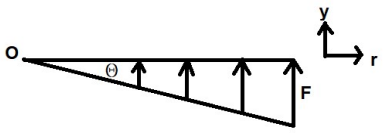

The force dependent on the stress-strain relationship is

$$F = \frac{E \times A \times \Delta y}{h}$$

Therefore moment is given as

$$M = \frac{2EA \times \Delta y \times r}{3h}$$

The angle due to the compression of one side of the rubber disc is:

$$\theta = \arctan\left(\frac{\Delta y}{r}\right)$$

Assuming that the angle remains small

$$\theta = \frac{\Delta y}{r}$$

The resulting rotational spring coefficient is:

$$k_{rx} = \frac{M}{\theta} = \frac{2EA \times r^2}{3h}$$

$k_{rx} := \frac{2}{3} \cdot \frac{E \cdot A \cdot d^2}{h \cdot 4} = 12123,354 \ \text{N} \ \frac{\text{mm}}{\text{deg}}$

y-axis:

Based on the angle of twist formula.

$J := \frac{\pi}{2} \cdot \left(\frac{d}{2}\right)^4 = 1,6219 \cdot 10^{-6} \ \text{m}^4$

$k_{ry} := \frac{J \cdot G}{h} = 3896,7924 \ \text{N} \ \frac{\text{mm}}{\text{deg}}$

Central Cord Spring Coefficient

$E_{cord} := 193 \ \text{GPa}$

$d_{cord} := 0,31 \ \text{in} = 7,874 \ \text{mm}$

$A_{cord} := \pi \cdot \frac{d_{cord}^2}{4} = 48,6946 \ \text{mm}^2$

$l_{cord} := 107,0 \ \text{mm}$

$k_{cord} := \frac{E_{cord} \cdot A_{cord}}{l_{cord}} = 87832,2956 \ \frac{\text{N}}{\text{mm}}$

Appendix C

Determining the ATD Parameter Values

The initial ATD model made many assumptions about the properties of the deformable elements which control the response of the model. These assumptions were not expected to provide a model that can pass validation, but rather provide a starting point for tuning. This appendix covers the process of tuning the model in order to pass validation.

C.1 Parameter Tuning

The process of tuning the model to fit the data started by identifying seven parameters that may have an impact on the reaction of the model. The parameters are the horizontal distances of the anterior and posterior springs, as well as the horizontal distance of the springs between the *Nodding_Joint* and the *Neck_Transducer*. Also, the damping coefficients of the springs are considered to be important parameters. Finally, the force-deflection curves of all the springs and the spring constant of the central cord are considered as parameters.

The effect that the parameters have on the model needed to be quantified in order to be able to adjust the model to match the literature. As such, each of the parameters were altered individually to a range of possible values and the maximum deflection of the head relative to the base is measured in the x- and y-axes as well as the root mean square of the acceleration in the x-axis. In order to compare the results between the different parameters, the values of the parameters were scaled according to the formula

$$x_{si} = \frac{x_i - x_0}{x_0}$$

where i is the test number, x_i is the value of the parameter for test i and x_0 is the original value of the parameter. Similarly, the measured values were normalised according to the formula

$$y_{si} = \frac{y_i - \mu}{\sigma}$$

where y_i is the difference between the original measured value and the new value, μ is the mean of y_i and σ is the standard deviation of y_i.

Table C.1 shows the Pearson correlation coefficients between the parameter values and the normalised measured values. This shows very high negative correlations for the X and Y deflection relative changes, while the correlation coefficients for the X acceleration relative change shows poorer correlations.

Table C.1: Pearson correlation coefficient between the scaled parameter values and the normalised output measurements

Variable	X Deflection Relative Change	Y Deflection Relative Change	X Acceleration Relative Change
Location of Anterior Springs for Rubber Discs	−0.941	−0.990	0.868
Central Cord Spring Coefficient	−0.921	−0.948	0.562
Damping Coefficients for Rubber Springs	−0.998	−0.992	0.934
Locations of Head Springs for *Nodding_Blocks*	−0.845	−0.937	0.757
Location of Posterior Springs for Rubber Discs	−0.999	−0.995	0.453
Scaling of Flexion and Extension Force-Deflection Curves	−0.990	−0.981	−0.426
Scaling of *Nodding_Block* Springs Force-Deflection Curve	−0.999	−0.981	0.311
Root Mean Square	0.958	0.975	0.654

Considering that the correlation values are so high, a linear assumption is made and the gradient is calculated between the smallest and greatest scaled parameter value for each of the parameters. While the linear assumption may not hold for all cases, the purpose of calculating the gradient was only to indicate the potential effect that each parameter has on the model. Figure C.1 shows the gradient of all three measurements for each of the parameters. This shows that changing the location of the anterior springs will have the greatest effect on the model, while scaling the force-deflection curve of the *Nodding_Block* springs is nearly inconsequential.

Knowing the effect of changing the parameters is useless unless a target for the model's response is established. Therefore, two sources were identified that

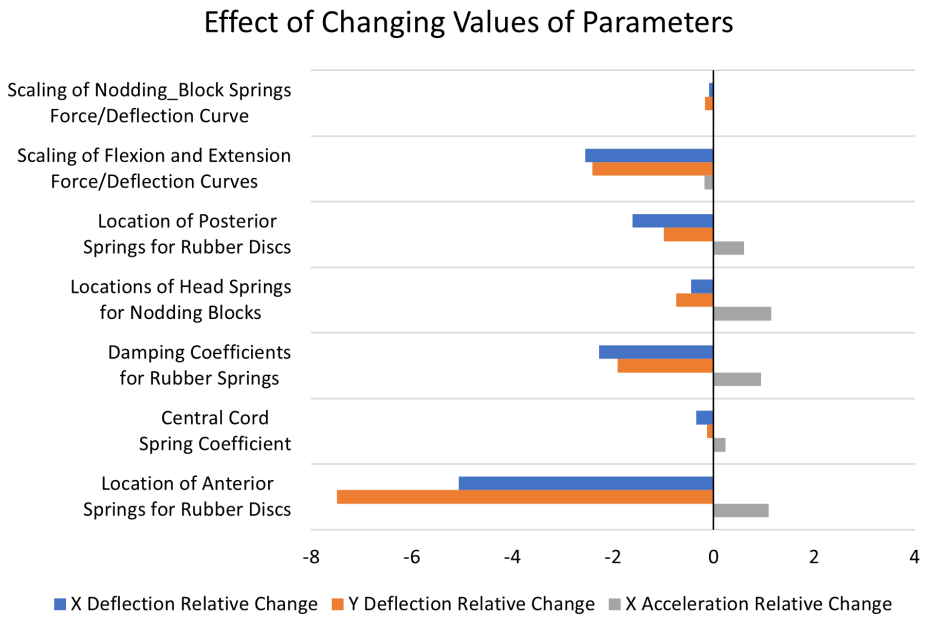

Figure C.1: The bar chart shows the expected effect on chosen variables by increasing the value of a selected parameter.

will act as targets.

The first source is Zhang *et al.* [55]. Zhang *et al.* used the neck calibration pendulum as prescribed by 49 CFR 572 [52] where the base of the neck is attached to a pendulum and the pendulum is released from a specified height to be stopped by an aluminium honeycomb block. Zhang *et al.* used the stipulated 7 m/s impact speed of the pendulum and reports the angle of the head over time. For the purpose of the model, the impact of the pendulum with the aluminium honeycomb needed to be converted into an acceleration profile. 49 CFR 572 [52] specifies the deceleration values resulting from the pendulum arm's impact at specific durations after impact for an impact velocity of 7 m/s and this data was used to generate the required acceleration profile. This acceleration profile is shown in Figure C.2.

The second source of target values is Mertz and Patrick [53] which determined response corridors for the moment about the occipital condyles with respect to the angle of rotation of the head. This source is relevant since the development of the Hybrid III is based on a mechanical neck designed by Culver *et al.* [54] which uses Mertz and Patrick for validation [49]. Culver *et al.* applied a square wave deceleration, as shown in Figure C.2, to bring the base of the neck to rest. The required data is recorded and the plot of moment versus head angle was created and compared to the specified corridor. For tuning, a similar square wave deceleration was applied to the base of the neck and the parameters were adjusted till the resulting moment versus head angle plot remains within the set corridor.

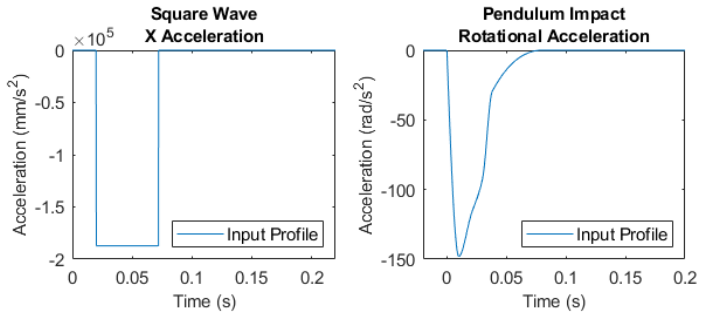

Figure C.2: Acceleration profiles used for parameter tuning of the model

C.2 Results of Tuning

The purpose of tuning the model was to determine the required parameters that will allow the model to behave as defined in literature. The chosen values of the parameters that are constant are listed in Table 3.4 and the force-deflection curves are shown in Figure 3.3.

The primary comparison of the model was to ensure that the angle of the head relative to the base matches that which is described in literature. Figure C.3 shows the comparison of the model to the results obtained by Zhang *et al.* [55]. From this graph it is clear to see that the model overshoots the maximum head rotation by approximately three and a half degrees. Aside from this, the general shape of the response reasonably close to that in literature to determine that the model may yield acceptable results.

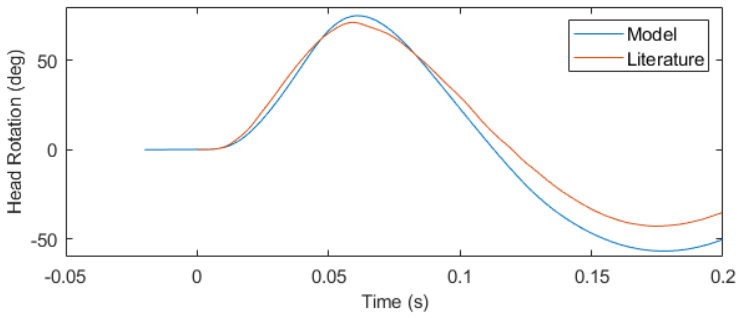

Figure C.3: Angle of the head over time for comparison with Zhang *et al.* [55]

The next comparison was determining whether the moment about the occipital condyles relative to the head rotation is within the loading corridor prescribed by Mertz and Patrick [53]. The measured moment is superimposed on the loading corridor in Figure C.4. The measured moment starts at approximately five degrees and remains within the corridor to the maximum moment before the moment reduces and subsequently exits the corridor. While it is undesirable to have the any aspect of the measured moment outside of the corridor, it is pos-

itive that the maximum moment is within the corridor since this value is used in the calculation of various neck injury criteria.

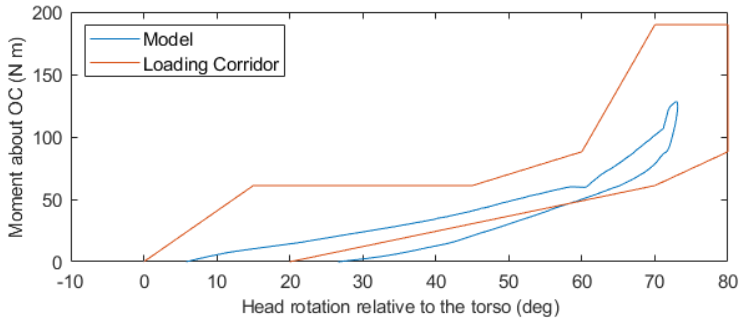

Figure C.4: Moment about the occipital condyle plotted against the angle of the head with corridors defined by Mertz and Patrick [53]

To conclude with the results of tuning the model, the model sufficiently aligns with the rotation of the head during under inertial loading and provides an maximum moment that is comfortably within the loading corridor. While there are some deviations from the literature, the model should be sufficient for the purpose of this project.

Appendix D

Optimising Activation Levels of Human Model

Section 4.5 provides an initial solution for the human model in terms of defining the activation levels of the muscles over the duration of the simulation. It is however possible for the model's response to be optimised using an appropriate algorithm. This appendix provides the methodology and the results of the optimisation process.

D.1 Methodology

Optimisation of the model required that the resulting validation curves be converted to numeric values and this was accomplished by calculating the error of each graph. The error calculation is based on the RMS of the error at each time value. The equation representing the error is Equation D.1, which requires the upper bound (ub) and lower bound (lb) from Thunnissen *et al.* [46], as well as a y for n values of x from 0 to 0.2 s. The values calculated in Equation D.2 are scaled in Equation D.1 according to the maximum range of the given corridors such that the error calculated can be comparable across all validation curves. This process assumed that the value of x is constantly increasing and therefore can only be used on the graphs that have time on their x-axis.

$$Error = \sqrt{\frac{\sum_{i=1}^{n}\left(\frac{err_i}{\max(ub)-\min(lb)}\right)^2}{n}} \tag{D.1}$$

$$err_i = \begin{cases} y_i - ub_i & \text{if } y_i > ub_i \\ 0 & \text{if } lb_i \leq y_i \leq ub_i \\ lb_i - y_i & \text{if } y_i < lb_i \end{cases} \tag{D.2}$$

where the subscript i denotes the value at x_i such as $err_i = err(x_i)$

With the process of quantifying the error completed, it was possible to optimise, but most forms of optimisation can only optimise for a single objective. Each of the validation graphs form a new objective and therefore there are eight

possible objectives to optimise for. These eight objectives were reduced to four by considering which may have the greatest effect on the tether angle optimisation procedure. The first two are the head link angle and the neck link angle, since they quantify how far the head moves forward. This is important, since the tether only acts as the head moves forward and therefore the model is expected to contain this information. The last two objectives are the OC compression force and moment. These objectives were selected since they determine the predicted level of injury according to the NIC.

The four objectives needed to be reduced to a single objective before being able to execute most optimisation algorithms. Therefore, the RMS of these objectives was taken as the overarching objective function.

For any optimisation problem, design variables are required. In this case, these variables were related to the activation levels as specified in Section 4.5. A total of eight variables were selected to make up the activation level curves. This concludes setting up of the optimisation problem.

The Bayesian optimisation algorithm was selected to determine the optimal activation levels. This is due to its ability to find to minimum objective value with a relatively low number of function evaluations.

D.2 Results and Discussion

The stated optimisation problem considered the RMS of the four identified objectives. However, it was also possible to optimise for other combinations of these objectives and therefore three different sets of optimisation results were obtained. These results were for the RMS of all four selected objectives, the RMS of the OC compression force and moment and lastly for the RMS of the head and neck angles. Each of the optimal activation levels are shown in Figure D.1 and compared to the manual process described in Section 4.5.

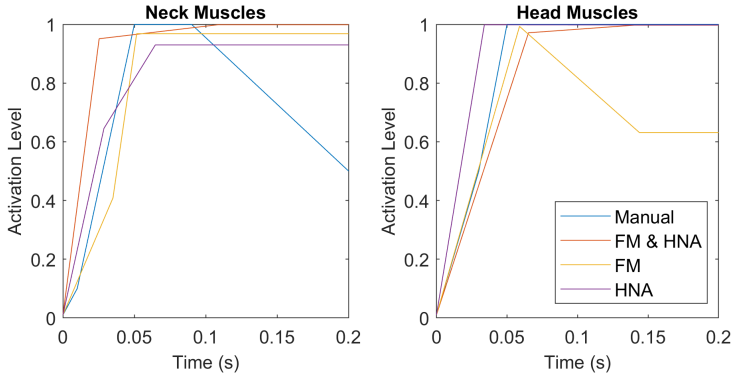

Figure D.1: Optimised activation levels based on the various combinations of optimisation objectives (FM = OC compression force and moment; HNA = Head and neck angles)

The three optimised activation level curves related to the muscles of the neck show very similar shapes, especially after 0.05 seconds where all are at a maximum above 90 % activation. The curves related to the head muscles are not as similar to each other as in the previous case, since the curve related to optimising for compression force and moment drop its activation level to just above 60 % toward the end. This is in contrast with the other two optimised curves that maintain an activation level of near 100 % towards the end of the time period.

The validation curves of the three different optimised activation levels are so similar that plotting them against each other is nearly impossible to read sensible information. Therefore, the mean and standard deviation is obtained for each of the validation curves and a corridor of one standard deviation around the mean is shown in Figure D.2. Considering the standard deviation that can be seen in Figure D.2, it becomes clear that the differences between the various optimised activation levels do not have a significant effect on resulting validation curves.

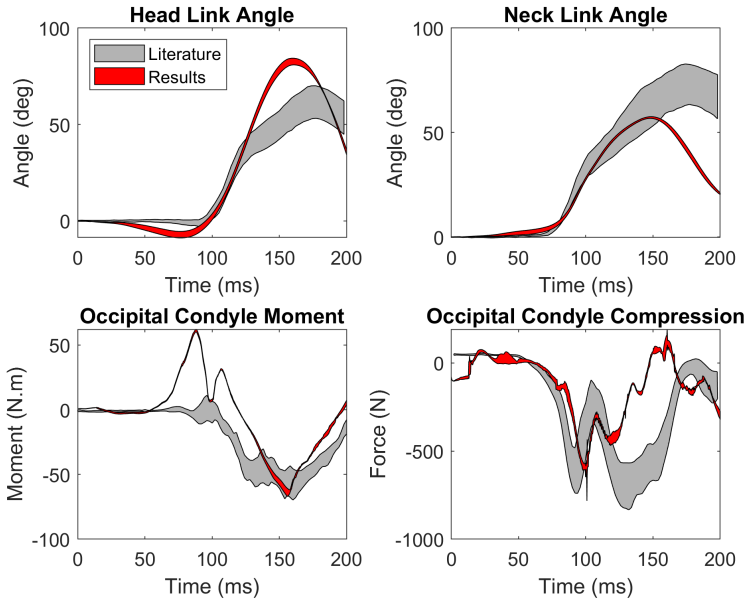

Figure D.2: Multiple optimisation results shown as a corridor of one standard deviation around the mean

The optimisation process suggests that while the model does not exactly follow the validation requirements, a better model will not be obtained by further altering the activation level parameters. A possible improvement could be seen if each muscle has its own activation level curve, but that will significantly increase the number of optimisation variables and therefore the complexity of the optimisation process. Based on the results that are currently available, it is decided to use the activation level curve that was optimised for all four the objectives, even though any of the others would be sufficient.

List of References

[1] Standard FIA 8853-2016. *Safety Harnesses*. 2015. [Online]. Available at: https://www.fia.com/sites/default/files/8853-2016_safety_harnesses.pdf, [2021, June 23].

[2] Standard FIA 8858-2010. *Frontal Head Restraint (FHR) System*. 2012. [Online]. Available at: https://www.fia.com/sites/default/files/regulation/file/8858-2010_Frontal_Head_Restraint_0.pdf, [2020, April 11].

[3] Standard FIA 8859-2015. *Premium Helmet*. 2015. [Online]. Available at: https://www.fia.com/sites/default/files/8859-2015_premium_helmet_0.pdf, [2021, June 1].

[4] Standard FIA 8860-2018. *Advanced Helmet*. 2012. [Online]. Available at: https://www.fia.com/sites/default/files/8860-2018_advanced_helmet_2.pdf, [2021, June 1].

[5] Chapman, M.A. and Oni, J. Motor racing accidents at Brands Hatch, 1988/9. *British Journal of Sports Medicine*. 1991. 25.3: 121–123. https://doi.org/10.1136/bjsm.25.3.121

[6] Steele, A.G. Emergency Medical Care for Open Wheel Racing Events at Indianapolis Raceway Park. *Annals of Emergency Medicine*. 1994. 24.2: 264–268. https://doi.org/10.1016/S0196-0644(94)70140-7

[7] Chesser, T., Norton, S., Nolan, J. and Baskett, P. What are the requirements for medical cover at motor racing circuits? *Injury*. 1999. 30.4: 293–297. https://doi.org/10.1016/S0020-1383(99)00086-8

[8] Minoyama, O. and Tsuchida, H. Injuries in professional motor car racing drivers at a racing circuit between 1996 and 2000. *British Journal of Sports Medicine*. 2004. 38.5: 613–616. https://doi.org/10.1136/bjsm.2003.007674

[9] SFI Specification 38.1. *Quality Assurance Specifications: Head and Neck Restraint Systems*. 2019. [Online]. Available at: https://www.sfifoundation.com/wp-content/pdfs/specs/Spec_38.1_041919.pdf, [2020, May 28].

[10] Fédération Internationale de l'Automobile. *Technical List N29: List of FIA-approved frontal head restraint (FHR) systems according to FIA Standard 8858-2010*. 2019. [Online]. Available at: https://www.fia.com/technical-list-ndeg29-fhr-systems-approved-according\-fia-standard-8858-2010, [2020, April 11].

[11] Fédération Internationale de l'Automobile. *Technical List N69: Helmets homologated according to the FIA Standard 8860-2018*. 2019. [Online]. Available at: https://www.fia.com/regulation/category/761, [2020, April 11].

[12] Kreinest, M., Scholz, M. and Trafford, P. On-scene treatment of spinal injuries in motor sports. *European Journal of Trauma and Emergency Surgery*. 2017. 43.2: 191–200. https://doi.org/10.1007/s00068-016-0749-3

[13] Kohan, E.J. and Wirth, G.A. Anatomy of the Neck. *Clinics in Plastic Surgery*. 2014. 41.1: 1–6. https://doi.org/10.1016/j.cps.2013.09.016

[14] Li, J. *Anatomy of the spine*. n.d. [Online]. Available at: https://med.virginia.edu/joshua-li/patient-conditions/anatomy-of-the-spine/, [2020, May 29].

[15] Dodwad, S.-n.M., Khan, S.N. and An, H.S. Cervical Spine Anatomy. In: Shen, F., Samartzis, D. and Fessler, R. (eds.), *Textbook of the Cervical Spine*, 1st edition. Philadelphia: Saunders. 2014. Chapter 1, 3–21. ISBN 978-1-4557-1143-7.

[16] Magee, D.J. Cervical Spine. In: *Orthopedic Physical Assessment*, 6th edition. Philadelphia: Saunders. 2014. Chapter 3, 148–223. ISBN 978-1-4557-0977-9.

[17] Netter, F.H. *Atlas of Human Anatomy*. 7th edition. Elsevier. 2019. ISBN 978-0-3233-9322-5.

[18] Grandjean, E. *Fitting the Task to the Man: A Textbook of Occupational Ergonomics*. 4th edition. Taylor & Francis. 1988. ISBN 978-0-8506-6379-2.

[19] Basmajian, J.V. *Primary anatomy*. 8th edition. Baltimore: Williams & Wilkins. 1982. ISBN 0-683-00550-2.

[20] Encyclopædia Britannica. *Striated muscle; human biceps muscle*. 2015. [Online]. Available at: https://www.britannica.com/science/muscle#/media/1/398553/46939, [2020, May 29].

[21] Deslauriers, J. Anatomy of the Neck and Cervicothoracic Junction. *Thoracic Surgery Clinics*. 2007. 17.4: 529–547. https://doi.org/10.1016/j.thorsurg.2006.12.009

[22] Physiopedia. *Category: Cervical Spine - Anatomy*. n.d. [Online]. Available at: https://www.physio-pedia.com/Category:Cervical_Spine_-_Anatomy, [2020, April 21].

[23] GetBodySmart. *Back Muscles Anatomy - Muscles that act on the Back*. n.d. [Online]. Available at: https://www.getbodysmart.com/back-muscles, [2020, April 21].

[24] Physiopedia. *Erector Spinae*. n.d. [Online]. Available at: https://www.physio-pedia.com/Erector_Spinae, [2021, February 22].

[25] Backman, J., Häkkinen, K., Ylinen, J., Häkkinen, A. and Kyröläinen, H. Neuromuscular Performance Characteristics of Open-Wheel and Rally Drivers. *The Journal of Strength and Conditioning Research*. 2005. 19.4: 777. https://doi.org/10.1519/R-16544.1

[26] Li, F., Liu, N.-s., Li, H.-g., Zhang, B., Tian, S.-w., Tan, M.-g. and Sandoz, B. A review of neck injury and protection in vehicle accidents. *Transportation Safety and Environment*. 2019. 1.2: 89–105. https://doi.org/10.1093/tse/tdz012

[27] Techy, F. and Benzel, E.C. Biomechanics of the Cervical Spine. In: Shen, F.H., Samartzis, D. and Fessler, R.G. (eds.), *Textbook of the Cervical Spine*, 1st edition. Saunders. 2015. Chapter 7, 64–69. ISBN 978-1-4557-1143-7.

[28] Boström, O., Svensson, M.Y., Aldman, B., Hansson, H.-A., Håland, Y., Lövsund, P., Seeman, T., Säljö, A. and Örtengren, T. A new neck injury criterion candidate-based on injury findings in the cervical spinal ganglia after experimental neck extension trauma. In: *Proceedings of The 1996 International Ircobi Conference On The Biomechanics Of Impact*. Dublin, Ireland. 1996. 123–136.

[29] National Highway Traffic Safety Administration. *Federal Motor Vehicle Standards, Code of Federal Regulations under Title 49, Part 571.208*. 2011. [Online]. Available at: https://www.govinfo.gov/content/pkg/CFR-2011-title49-vol6/pdf/CFR-2011-title49-vol6-sec571-208.pdf, [2021, August 26].

[30] Schmitt, K.-U., Muser, M.H., Walz, F.H. and Niederer, P.F. N km –A Proposal for a Neck Protection Criterion for Low-Speed Rear-End Impacts. *Traffic Injury Prevention*. 2002. 3.2: 117–126. https://doi.org/10.1080/15389580212002

[31] Van Lopik, D.W. and Acar, M. A computational model of the human head and neck system for the analysis of whiplash motion. *International Journal of Crashworthiness*. 2004. 9.5: 465–473. https://doi.org/10.1533/ijcr.2004.0302

[32] De Jager, M.K.J. *Mathematical head-neck models for acceleration impacts*. Doctoral dissertation. Eindhoven University of Technology, Eindhoven. 1996. [Online]. Available at: https://doi.org/10.6100/IR460661, [2020, February 24].

[33] Van der Horst, M.J. *Human head neck response in frontal, lateral and rear end impact loading : modelling and validation*. Doctoral dissertation. Technische Universiteit Eindhoven. 2002. [Online]. Available at: https://doi.org/10.6100/IR554047, [2020, February 24].

[34] Van Lopik, D.W. *A computational model of the human head and cervical spine for dynamic impact simulation*. Doctoral dissertation. Loughborough University. 2004. [Online]. Available at: https://hdl.handle.net/2134/7643, [2020, February 24].

[35] Nissan, M. and Gilad, I. The cervical and lumbar vertebrae - an anthropometric model. *Engineering in Medicine*. 1984. 13.3: 111–114. https://doi.org/10.1243/EMED_JOUR_1984_013_030_02

[36] Moroney, S.P., Schultz, A.B., Miller, J.A. and Andersson, G.B. Load-displacement properties of lower cervical spine motion segments. *Journal of Biomechanics*. 1988. 21.9: 769–779. https://doi.org/10.1016/0021-9290(88)90285-0

[37] Yoganandan, N., Pintar, F., Maiman, D., Cusick, J., Sances, A. and Walsh, P. Human head-neck biomechanics under axial tension. *Medical Engineering & Physics*. 1996. 18.4: 289–294. https://doi.org/10.1016/1350-4533(95)00054-2

[38] Camacho, D.L., Nightingale, R.W., Robinette, J.J., Vanguri, S.K., Coates, D.J. and Myers, B.S. Experimental Flexibility Measurements for the Development of a Computational Head-Neck Model Validated for Near-Vertex Head Impact. In: *SAE Technical Papers*. 1997. https://doi.org/10.4271/973345

[39] van Lopik, D.W. and Acar, M. Development of a multi-body computational model of human head and neck. *Proceedings of the Institution of Mechanical Engineers, Part K: Journal of Multi-body Dynamics*. 2007. 221.2: 175–197. https://doi.org/10.1243/14644193JMBD84

[40] Cheng, E.J., Brown, I.E. and Loeb, G.E. Virtual muscle: a computational approach to understanding the effects of muscle properties on motor control. *Journal of Neuroscience Methods*. 2000. 101.2: 117–130. https://doi.org/10.1016/S0165-0270(00)00258-2

[41] Haeufle, D., Günther, M., Bayer, A. and Schmitt, S. Hill-type muscle model with serial damping and eccentric force–velocity relation. *Journal of Biomechanics*. 2014. 47.6: 1531–1536. https://doi.org/10.1016/j.jbiomech.2014.02.009

[42] White, A. and Panjabi, M.M. *Clinical Biomechanics of the Spine*. 2nd edition. Philadelphia: Lippincott. 1990. ISBN 0-397-50720-8.

[43] Wheeldon, J.A., Pintar, F.A., Knowles, S. and Yoganandan, N. Experimental flexion/extension data corridors for validation of finite element models of the young, normal cervical spine. *Journal of Biomechanics*. 2006. 39.2: 375–380. https://doi.org/10.1016/j.jbiomech.2004.11.014

[44] Oda, T., Panjabi, M.M. and Crisco, J.J. Three-Dimensional Translational Movements of the Upper Cervical Spine. *Journal of Spinal Disorders*. 1991. 4.4: 411–419. https://doi.org/10.1097/00002517-199112000-00002

[45] Van Lopik, D.W. and Acar, M. Dynamic verification of a multi-body computational model of human head and neck for frontal, lateral, and rear impacts. *Proceedings of the Institution of Mechanical Engineers, Part K: Journal of Multi-body Dynamics*. 2007. 221.2: 199–217. https://doi.org/10.1243/14644193JMBD89

[46] Thunnissen, J., Wismans, J., Ewing, C.L. and Thomas, D.J. Human Volunteer Head-Neck Response in Frontal Flexion: A New Analysis. In: *SAE Technical Papers*. 1995. https://doi.org/10.4271/952721

[47] Humanetics. *About Frontal Impact Dummies*. n.d. [Online]. Available at: https://www.humaneticsatd.com/crash-test-dummies/frontal-impact, [2020, May 22].

[48] Xu, T., Sheng, X., Zhang, T., Liu, H., Liang, X. and Ding, A. Development and Validation of Dummies and Human Models Used in Crash Test. *Applied Bionics and Biomechanics*. 2018. 2018: 1–12. https://doi.org/10.1155/2018/3832850

[49] Foster, J.K., Kortge, J.O. and Wolanin, M.J. Hybrid III — A Biomechanically-Based Crash Test Dummy. *SAE Transactions*. 1977. 3268–3283.

[50] Spittle, E.K., Miller, D.J., Shipley Jr, B.W. and Ints, K. Hybrid II and hybrid III dummy neck properties for computer modeling. *Air Force Systems Command, Wright-Patterson Air Force Base, Ohio*. 1992. 1–138.

[51] Deng, Y.-c. Anthropomorphic dummy neck modeling and injury considerations. *Accident Analysis & Prevention*. 1989. 21.1: 85–100. https://doi.org/10.1016/0001-4575(89)90051-1

[52] National Highway Traffic Safety Administration. *Anthropomorphic test devices-Hybrid III test dummy, Code of Federal Regulations under Title 49, Part 572, Subpart E*. 1986. [Online]. Available at: https://www.ecfr.gov/cgi-bin/retrieveECFR?gp=1&SID=557bfaef16d1a0e2775a5242ab26e41e&ty=HTML&h=L&mc=true&r=PART&n=pt49.7.572#se49.7.572_133, [2020, September 28].

[53] Mertz, H.J. and Patrick, L.M. Strength and Response of the Human Neck. In: *SAE Technical Papers*. 1971. https://doi.org/10.4271/710855

[54] Culver, C.C., Neathery, R.F. and Mertz, H.J. Mechanical Necks with Humanlike Responses. In: *SAE Technical Papers*. 1972. 61–75. https://doi.org/10.4271/720959

[55] Zhang, L., Ramesh, D., Yang, K.H. and King, A.I. Effectiveness of the Football Helmet Assessed by Finite Element Modeling and Impact Testing. In: *IRCOBI conference*, September. 2003. 27–38.

[56] Hubbard, R.P. Neck Protection Device with Occupant of a High Performance Vehicle. 1987. United States Patent 4638510.

[57] Gramling, H., Hodgman, P. and Hubbard, R. Development of the HANS Head and Neck Support for Formula One. In: *Motorsports Engineering*. 1998. https://doi.org/10.4271/983060

[58] Tiger Performance. *HANS Device Pro Ultra Lite - 30 Degree*. n.d. [Online]. Available at: https://tigerperformance.com/hans-devices/hans-device-pro-ultra-lite-30-degree.html, [2020, May 29].

[59] Gramling, H. and Hubbard, R. Development of an Airbag System for FIA Formula One and Comparison to the HANS Head and Neck Support. In: *SAE Motorsports Engineering Conference & Exposition*. 2000. https://doi.org/10.4271/2000-01-3543

[60] Kaul, A., Abbas, A., Smith, G., Manjila, S., Pace, J. and Steinmetz, M. A revolution in preventing fatal craniovertebral junction injuries: lessons learned from the Head and Neck Support device in professional auto racing. *Journal of Neurosurgery: Spine*. 2016. 25.6: 756–761. https://doi.org/10.3171/2015.10.SPINE15337

[61] Patalak, J.P., Harper, M.G. and Stitzel, J.D. Implications of head and neck restraint test repeatability for specification improvement. *Traffic Injury Prevention*. 2019. 20.6: 588–594. https://doi.org/10.1080/15389588.2019.1633467

[62] Snyman, J.A. *Practical Mathematical Optimization*, vol. 97 , *Applied Optimization*. New York: Springer-Verlag. 2005. ISBN 0-387-24348-8.

[63] Jones, D.R., Schonlau, M. and Welch, W.J. Efficient Global Optimization of Expensive Black-Box Functions. *Journal of Global Optimization*. 1998. 13.4: 455–492. https://doi.org/10.1023/A:1008306431147

[64] Keane, A., Forrester, A. and Sobester, A. *Engineering Design via Surrogate Modelling: A Practical Guide*. Washington, DC: American Institute of Aeronautics and Astronautics, Inc. 2008. ISBN 978-1-56347-955-7.

[65] Rasmussen, C.E. and Williams, C.K.I. *Gaussian Processes for Machine Learning*. Cambridge, Mass.: MIT Press. 2005. ISBN 978-0-2621-8253-9.

[66] Snoek, J., Larochelle, H. and Adams, R.P. Practical Bayesian optimization of machine learning algorithms. *Advances in Neural Information Processing Systems*. 2012. 4: 2951–2959.

[67] Neal, R.M. *Bayesian Learning for Neural Networks*. Doctoral dissertation. University of Toronto. 1995. [Online]. Available at: https://citeseerx.ist.psu.edu/viewdoc/download?doi=10.1.1.446.9306&rep=rep1&type=pdf, [2021, July 20].

[68] Agnihotri, A. and Batra, N. Exploring Bayesian Optimization. *Distill*. 2020. 5.5. https://doi.org/10.23915/distill.00026

[69] Shahriari, B., Swersky, K., Wang, Z., Adams, R.P. and De Freitas, N. Taking the human out of the loop: A review of Bayesian optimization. *Proceedings of the IEEE*. 2016. 104.1: 148–175. https://doi.org/10.1109/JPROC.2015.2494218

[70] Yoganandan, N., Pintar, F.A., Zhang, J. and Baisden, J.L. Physical properties of the human head: Mass, center of gravity and moment of inertia. *Journal of Biomechanics*. 2009. 42.9: 1177–1192. https://doi.org/10.1016/j.jbiomech.2009.03.029

[71] Forsythe, W. Smithsonian Physical Tables (9th Revised Edition): Table 229. Compression of Synthetic and Natural Rubbers. 1954; 2003. Available at: https://app.knovel.com/hotlink/khtml/id:kt002VRDS1/smithsonian-physical/table-229-compression, [2020, August 10].

[72] BodyParts3D. © The Database Center for Life Science licensed under CC Attribution-Share Alike 2.1 Japan. n.d. [Online]. Available at: http://lifesciencedb.jp/bp3d/, [2020, June 20].

[73] Mitsuhashi, N., Fujieda, K., Tamura, T., Kawamoto, S., Takagi, T. and Okubo, K. BodyParts3D: 3D structure database for anatomical concepts. *Nucleic Acids Research*. 2009. 37.Database: D782–D785. https://doi.org/10.1093/nar/gkn613

[74] Nagaoka, T., Watanabe, S., Sakurai, K., Kunieda, E., Watanabe, S., Taki, M. and Yamanaka, Y. Development of realistic high-resolution whole-body voxel models of Japanese adult males and females of average height and weight, and application of models to radio-frequency electromagnetic-field dosimetry. *Physics in Medicine and Biology*. 2004. 49.1: 1–15. https://doi.org/10.1088/0031-9155/49/1/001

[75] Zhang, C., Mannen, E.M., Sis, H.L., Cadel, E.S., Wong, B.M., Wang, W., Cheng, B., Friis, E.A. and Anderson, D.E. Moment-rotation behavior of intervertebral joints in flexion-extension, lateral bending, and axial rotation at all levels of the human spine: A structured review and meta-regression analysis. *Journal of Biomechanics*. 2020. 100: 109579. https://doi.org/10.1016/j.jbiomech.2019.109579

[76] Yoganandan, N., Kumaresan, S. and Pintar, F.A. Biomechanics of the cervical spine Part 2. Cervical spine soft tissue responses and biomechanical modeling. *Clinical Biomechanics*. 2001. 16.1: 1–27. https://doi.org/10.1016/S0268-0033(00)00074-7

[77] Mattucci, S.F. and Cronin, D.S. A method to characterize average cervical spine ligament response based on raw data sets for implementation into injury biomechanics models. *Journal of the Mechanical Behavior of Biomedical Materials*. 2015. 41: 251–260. https://doi.org/10.1016/j.jmbbm.2014.09.023

[78] Mattucci, S.F., Moulton, J.A., Chandrashekar, N. and Cronin, D.S. Strain rate dependent properties of human craniovertebral ligaments. *Journal of the Mechanical Behavior of Biomedical Materials*. 2013. 23: 71–79. https://doi.org/10.1016/j.jmbbm.2013.04.005

[79] Panjabi, M., Dvorak, J., Crisco, J., Oda, T., Hilibrand, A. and Grob, D. Flexion, extension, and lateral bending of the upper cervical spine in response to alar ligament transections. *Journal of spinal disorders*. 1991. 4.2: 157–67. https://doi.org/10.1097/00002517-199106000-00005

[80] Vasavada, A.N., Li, S. and Delp, S.L. Influence of Muscle Morphometry and Moment Arms on the Moment-Generating Capacity of Human Neck Muscles. *Spine*. 1998. 23.4: 412–422. https://doi.org/10.1097/00007632-199802150-00002

[81] Njus, G.O., Liu, Y.K. and Nye, T.A. The inertial and geometrical properties of helmets. *Medicine & Science in Sports & Exercise*. 1984. 16.5: 498–505. https://doi.org/10.1249/00005768-198410000-00014

[82] Toomey, D.E., Yang, K.H. and Van Ee, C.A. The Hybrid III Upper and Lower Neck Response in Compressive Loading Scenarios With Known Human Injury Outcomes. *Traffic Injury Prevention*. 2014. 15.March 2015: S223–S230. https://doi.org/10.1080/15389588.2014.931950

[83] Leatt Corporation. Dynamic Testing of Head and Neck Restraints. 2012.

[84] Jones, T.C. and Doggett, W.R. Time-Dependent Behavior of High Strength Kevlar and Vectran Webbing. In: *55th AIAA/ASME/ASCE/AHS/ASC Structures, Structural Dynamics, and Materials Conference*. American Institute of Aeronautics and Astronautics. 2014. 1–22. https://doi.org/10.2514/6.2014-1328

[85] Pereira Neto, A.H., Geiger, F.P., Lisbôa, T.V. and Marczak, R.J. Mechanical Analysis of Polymeric Webbing Tests With and Without Preloads. In: *Proceedings of the 4th Brazilian Conference on Composite Materials*, 1. Pontifícia Universidade Católica do Rio de Janeiro. 2018. 390–397. https://doi.org/10.21452/bccm4.2018.05.04

[86] Snell Memorial Foundation, Inc. *SA2015 Standard for Protective Headgear*. 2014. [Online]. Available at: https://www.smf.org/standards/sa/2015/SA2015Final3252014.pdf, [2021, May 13].

[87] *Get Started Racing.com*. 2017. [Online]. Available at: http://www.getstartedracing.com/protect-your-neck/, [2020, June 11].

[88] Lundberg, S.M. and Lee, S.-I. A Unified Approach to Interpreting Model Predictions. In: *31st Conference on Neural Information Processing Systems*. 2017. ISSN 10495258.